Title
Generation of Quasi-Perpendicular Collisionless Shocks by a Laser-Driven Magnetic Piston

Author
Schaeffer, Derek

Publication Date
2014

Peer reviewed|Thesis/dissertation

University of California
Los Angeles

Generation of Quasi-Perpendicular Collisionless Shocks by a Laser-Driven Magnetic Piston

A dissertation submitted in partial satisfaction
of the requirements for the degree
Doctor of Philosophy in Physics

by

Derek Schaeffer

2014

Abstract of the Dissertation

Generation of Quasi-Perpendicular Collisionless Shocks by a Laser-Driven Magnetic Piston

by

Derek Schaeffer

Doctor of Philosophy in Physics

University of California, Los Angeles, 2014

Professor Christoph Niemann, Chair

Collisionless shocks are ubiquitous in many space and astrophysical plasmas. However, since space shocks are largely steady-state, spacecraft are not well suited to studying shock formation *in situ*. This work is concerned with the generation and study in a laboratory setting of magnetized, quasi-perpendicular collisionless shocks relevant to space shocks. Experiments performed at the Large Plasma Device (LAPD) at UCLA and the Trident Laser Facility at Los Alamos National Laboratory (LANL) combined a magnetic piston driven by a high-energy laser (Raptor at UCLA or Trident at LANL) incident on a carbon target with a preformed, magnetized background plasma. Magnetic flux measurements and 2D hybrid simulations indicate that a magnetosonic pulse consistent with a low-Mach number collisionless shock was formed in the ambient plasma. The characteristics of the shock are analyzed and compared to other experiments in which no shock or a shock precursor formed. The results and simulations reveal that the various experimental conditions can be organized into weak and moderate coupling regimes, in which no shock forms, and a strong coupling regime, in which a full shock forms. A framework for studying these regimes and designing future shock experiments is devised.

Early-time laser-plasma parameters necessary to characterize the different shock coupling regimes are studied through experiments performed at the LAPD and Phoenix laboratory at UCLA. In addition to spectroscopic and fast-gate filtered photography, the experiments

utilize a custom Thomson scattering diagnostic, optimized for a novel electron density and temperature regime where the transition from collective to non-collective scattering could be spatially resolved. Data from the experiments and 3D analytic modeling indicate that the laser-plasma is best fit at early times with an isentropic, adiabatic fluid model and is consistent with a recombination-dominated plasma for which the electron temperature $T_e \propto t^{-1}$. In addition, spectroscopic measurements and 1D radiation-MHD simulations reveal that the laser-plasma velocity distribution is segregated by charge state, with the fastest ion species having the highest charge state, but the slowest species having the most mass. The results also suggest that the fastest non-trivial ion population (the dominant charge state) at typical laser intensities ($I_0 \sim 10^{11}$ W cm^{-2}) is CV (C^{+4}).

The dissertation of Derek Schaeffer is approved.

Christopher Russel

Walter Gekelman

Christoph Niemann, Committee Chair

University of California, Los Angeles

2014

To Hayden

Table of Contents

List of Figures

List of Tables

Acknowledgments

I would like to thank:

My advisor, Prof. Chris Niemann, for convincing me to join his lab within six hours of visiting UCLA, for giving me the opportunity to help him build the lab, and for his continuous support, advice, and guidance.

Dr. Carmen Constantin, for building from scratch not one but three laser systems, for sitting alone in the control room for hours to run the lasers, and for refusing to succumb to the capricious will of the laser gods.

Dr. Dan Winske, Dr. David Montgomery, and Dr. Siegfried Glenzer for their mentorship and help in running experiments.

Prof. Walter Gekelman, Prof. Troy Carter, and Prof. Christopher Russel for their guidance and for being on my committee.

Prof. George Morales, for teaching the best series of classes I've ever taken.

Dr. Patrick Pribyl, Lucky Zoltan, and Marvin Drandell, for their help in making my experiments on the LAPD run smoothly.

Michael Okuda, for inventing the LCARS graphical interface from which I liberally borrowed.

My fellow graduate students, for countless fruitful discussions. In particular: Erik Everson, for building lots of tiny probes, for explaining more than I could ever want to know about cars, weight-lifting, and cycling, and for being a fellow perfectionist; Anton Bondarenko, for showing time and again that if you go far enough down the rabbit-hole, you'll find something at the bottom, and for sharing his many post-modern philosophies; and Eric Clark, for building and running simulations, for knowing everything about linux, and for his beer brewing mastery.

Many others, who together have contributed to the amazing time I've had in graduate

school.

My family, for their support and love, for always encouraging me, and for only occasionally asking me when I'd graduate.

Vita

2007	B.A. (Physics), Cornell University
2008	M.S. (Physics), University of California, Los Angeles
2007-2008	Teaching Fellow, University of California, Los Angeles.
2008-2014	Research Fellow, University of California, Los Angeles.

Publications

D.B. Schaeffer, E.T. Everson, A.S. Bondarenko, S.E. Clark, C.G. Constantin, S. Vincena, B. Van Compernolle, S.K.P. Tripathi, D. Winske, W. Gekelman, C. Niemann. "Laser-driven, magnetized quasi-perpendicular collisionless shocks on the Large Plasma Device." *Physics of Plasmas*, **21**(5):056312, May 2014.

D.B. Schaeffer, E.T. Everson, D. Winske, C.G. Constantin, A.S. Bondarenko, L.A. Morton, K.A. Flippo, D.S. Montgomery, S.A. Gaillard, and C. Niemann. "Generation of magnetized collisionless shocks by a novel, laser-driven magnetic piston." *Physics of Plasmas*, **19**(7):070702, July 2012.

D.B. Schaeffer, D.S. Montgomery, A.S. Bondarenko, L.A. Morton, R.P. Johnson, T. Shimada, C.G. Constantin, E.T. Everson, S.A. Letzring, S.A. Gaillard, K.A. Flippo, S.H. Glenzer, and C. Niemann. "Thomson Scattering Measurements of Temperature and Density in a Low-Density, Laser-Driven Magnetized Plasma." *Journal of Instrumentation*, **7**(2):P02002, Feb. 2012.

D. B. Schaeffer, N. L. Kugland, C. G. Constantin, E. T. Everson, B. Van Compernolle, C. A. Ebbers, S. H. Glenzer, and C. Niemann. "A scalable multipass laser cavity based on injection by frequency conversion for noncollective Thomson scattering." *Review of Scientific Instruments*, **81**(10):10D518, 2010.

CHAPTER 1

Introduction

Collisionless shocks are prevalent in many astrophysical and terrestrial space environments, including supernovae remnants, coronal mass ejections, the solar wind, and ionospheric explosions. In many of these systems, the basic structure can be modeled as that of a magnetic piston driving a shock through a magnetized ambient plasma. The shock is formed when accelerated plasma flows through the ambient plasma faster than the ambient magnetosonic speed, and functions to decelerate the ambient plasma in the shock frame while simultaneously increasing entropy through heating. Unlike hydrodynamic shocks that dissipate energy through classical collisions over scale lengths on the order of the classical mean free path, collisionless shock energy is dissipated through electromagnetic effects over far shorter length scales.

Besides their ubiquity in space environments, collisionless shocks are of general interest for several reasons. While these shocks have been studied remotely and *in situ* by spacecraft for decades, those systems are difficult to diagnose or largely steady-state, and so have focused on properties of pre-formed shocks (see [68] and [77] for reviews on terrestrial space and astrophysical shocks, respectively). As a result, the microphysics of shock formation has been largely left to theoretical efforts. With the recent discovery [44] that Earth's bow shock can reform, there has been renewed interest in understanding shock formation. Additionally, several physical effects are still not well understood, including the mechanism by which entropy is generated in the shock front [43] and the process by which ions are accelerated to extremely high energies [34].

By providing greater control over relevant parameters and reproducibility, appropriately-

Condition	
Super-Alfvénic	$M_A > 1$
Sufficient Coupling	$R_M/\rho_d > 1$
Sufficient Space	$D_0/\rho_{a,s} = D_0 \cdot M_A^{-1}(c/\omega_{pi,s})^{-1} > 1$
Sufficient Time	$T \cdot \Omega_{ci,s}^{-1} > 1$
Collisionless	$\lambda_{ii,s}/D_0 > 1$

Table 1.1: Necessary conditions to form a collisionless shock. R_M/ρ_d is a condition on piston-ambient ion coupling, where R_M is the equal mass radius and ρ_d is the debris directed gyroradius. $T = D_0/v_A$ is the shock transit time and D_0 is the system size. For shocked ambient ions, $\rho_{a,s}$ is the directed gyroradius, $(c/\omega_{pi,s})$ is the inertial length, $\Omega_{ci,s}^{-1}$ is the cyclotron period, and $\lambda_{ii,s}$ is the ion-ion mean free path.

scaled laboratory experiments can thus contribute to an understanding of collisionless shocks, despite orders of magnitude differences in scale [20, 89]. Moreover, experiments can help validate complex computational codes and complement spacecraft measurements. In the past five decades, much work has been done on collisionless shocks in the laboratory. Early work used θ-pinches to drive imploding pistons to successfully create perpendicular shocks, but the shocks did not separate from the piston [61, 30, 18, 78]. Later experiments that combined a laser-produced plasma with a θ-pinch achieved some success it creating a shock-like structure that separated from the piston [63, 2]. Other experiments studied the diamagnetic cavity generated by a sub-Alfvénic laser-driven plasma in an external magnetic field [35, 19, 65, 85, 12], while more recent work has focused on studying collisionless shocks by combining a laser-plasma with a Z-pinch [64] or through field-reversed configuration (FRC) plasma guns [49].

Previous efforts have been largely unsuccessful because there are several criteria that must be simultaneously fulfilled by scaled laboratory shock experiments to be of relevance to space and astrophysical environments [15] (see Table 1.1). The magnetic piston must drive a super-Alvénic magnetic pulse through a magnetized ambient plasma long enough for

instabilities to grow in the pulse front. This also implies that the system size must be large enough for a shocked ambient ion moving at the shock speed to complete one gyro-orbit. The mean-free-path of a shocked ambient ion must also be much larger than the system size to avoid classical collisions. To ensure sufficient coupling between the piston and ambient ions, hybrid simulations have predicted that the piston width must be larger than an ion inertial length [59] and the piston radius must be larger than a piston ion directed gyroradius [11]. Together, these criteria simultaneously require a high-energy piston (so that the pulse is super-Alfvénic) and a highly magnetized ambient plasma (so that the piston couples to the ambient plasma) while keeping the ratio $\beta = E_{piston} \cdot (8\pi/B^2) > 1$.

Recent experiments [15, 71, 58, 70] carried out at UCLA and elsewhere have achieved the above criteria, as discussed in Chapter 3. These experiments combine a high-energy laser capable of driving a super-Alfvénic piston with a pre-formed, magnetized ambient plasma sufficiently large to allow a shock to form and separate. An outline of this process is presented in sections 1.1-1.3.

1.1 Laser-Produced Plasmas

When a laser impinges a target, a laser-produced plasma (LPP) is formed. The LPP will expand and, if an ambient magnetic field is present, interact with the field to form a diamagnetic cavity ("bubble"), as outlined below. This forms the basis of the magnetic piston.

1.1.1 Laser-Target Interaction

When the surface of a target is irradiated by a laser, the intense electric fields of the laser cause target electrons to vibrate, leading to either heating and evaporation or, if sufficiently intense, the direct ejection of target material [76, 75]. This ablated plasma is highly collisional and isothermal, with a initial temperature that depends on the laser-target interaction. At higher densities up to the critical density, the plasma can be further heated by absorbing laser energy directly through an inverse bremmstrahlung process, in which a photon is captured by

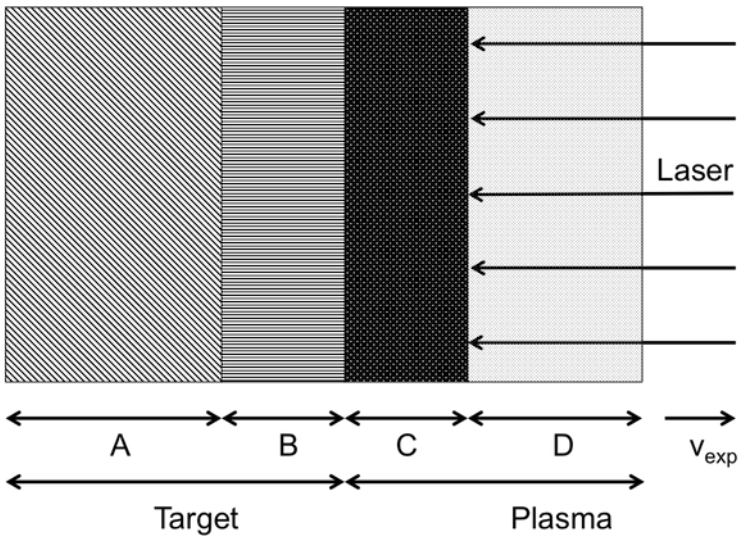

Figure 1.1: Schematic diagram showing different phases present during laser irradiation of a target: (A) unaffected target, (B) ablated target material, (C) dense plasma absorbing laser radiation, and (D) expanding plasma transparent to laser. Adapted from R.K. Singh [76].

an electron [50]. Since the plasma density decreases rapidly as it expands, the ablated plasma will be transparent to the laser everywhere but a small region near the target surface (see Fig. 1.1). A dynamic equilibrium can thus be established, in which high-density evaporated plasma absorbs laser energy, which causes less material to be evaporated, which lowers the plasma density and restarts the process. The thermal energy attained in this region is then quickly converted to kinetic energy as the plasma expands.

1.1.2 Expansion into Vacuum

Since the duration of the laser pulse ($\sim$ 10 ns) is generally much shorter than the dynamics of interest (100s of ns or more), the production of the LPP can be considered instantaneous and can be modeled as a hot, highly confined gas. The size of the initial gas cloud will be large parallel to the target surface (due to the extended spot size of the laser) relative to the size perpendicular to the target. As such, large pressure gradients will drive a rapid expansion of the LPP, primarily in the perpendicular direction, resulting in an ellipsoidal plasma volume (see Fig. 1.2a). The expansion can be considered adiabatic since the plasma

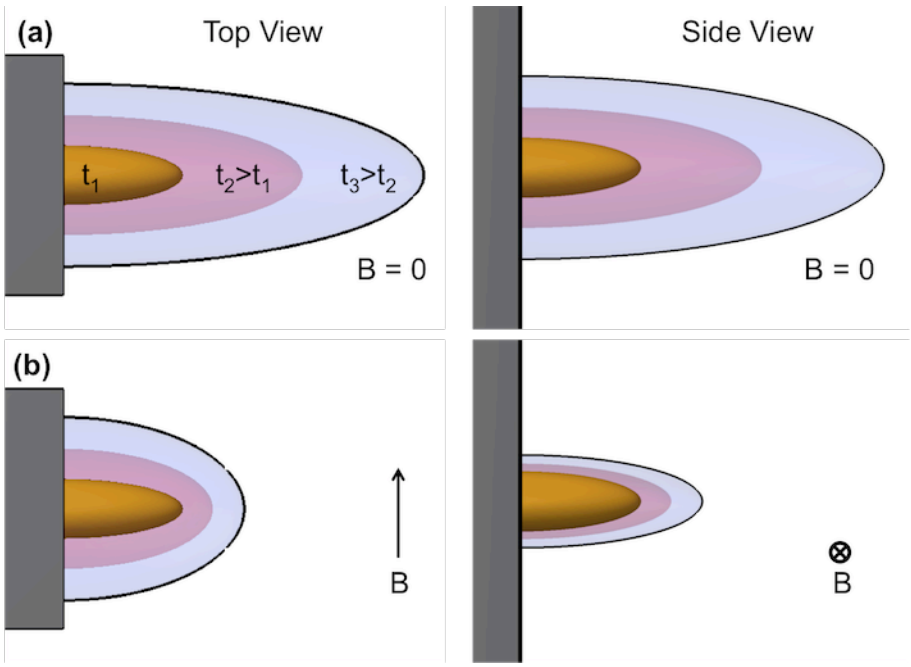

Figure 1.2: Representative shape of a laser-produced plasma without (a) and with (b) a background magnetic field. The plasma generally takes an ellipsoidal shape due to pressure anisotropies.

cannot exchange energy with its surroundings.

1.1.3 Expansion into a Magnetized Plasma

With the addition of an external magnetic field, the condition of adiabaticity is no longer valid. Instead, a LPP expanding across a magnetic field will form a diamagnetic cavity [19, 84, 14]. In the MHD picture, this is a result of the magnetic field being advected with the magnetized electrons (which are tied to the field lines) as they are pulled along by the unmagnetized ions. In the kinetic picture, the space-charge separation of magnetized electrons and unmagnetized ions sets up a radial ambipolar electric field, which in turn induces an $\vec{E} \times \vec{B}$ azimuthal drift (primarily) on the electrons. This drift forms the diamagnetic current and acts to expel the magnetic field within the current layer while compressing it at the layer's edge [65, 85]. The diamagnetic current is further reinforced by electron pressure

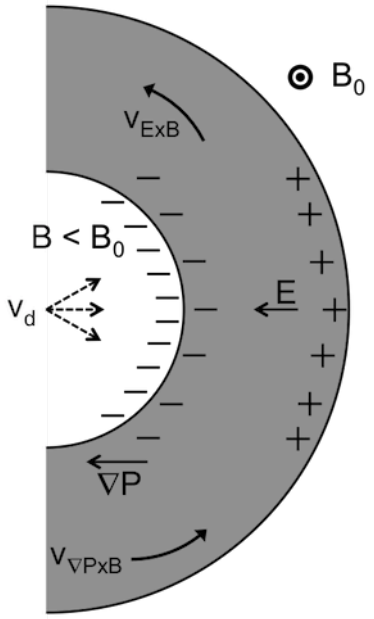

Figure 1.3: Diagram of a diamagnetic cavity. The laser expansion is assumed to be symmetric. The diamagnetic current is driven by $\vec{E} \times \vec{B}$ and $\nabla P \times \vec{B}$ drifts and acts to expel the magnetic field within the current layer.

gradients (either in temperature or density) at the cavity edge in the form of $\nabla P \times \vec{B}$ currents (see Fig. 1.3).

The shape of the resulting LPP will change from the radially-dominated ellipsoid in vacuum to more of an oblate spheroid (*e.g.* bulging disk, see Fig. 1.2b), with the dimensions along the field and perpendicular to the target being similar (since the magnetic field will tend to retard the faster radial motion of the LPP while having little effect on the slower parallel motion), but the dimension perpendicular to both being small (since it is both slower moving and retarded by the field).

The size of the bubble can be estimated from simple energy considerations, ignoring energy sinks like shear Alfvén waves and spatial asymmetries in the bubble. The initial kinetic energy $E_d = \frac{1}{2} m_d N_d v_d^2$ of a LPP composed of N_d ions of mass m_d moving uniformly at speed v_d in a sphere of radius R can be written, assuming all the energy is used to expel a magnetic field B_0, as

$$E_d = \left(\frac{B_0^2}{8\pi}\right) \cdot \left(\frac{4\pi}{3} R^3\right) \tag{1.1}$$

The resulting cavity radius $R = R_B = (3N_d m_d v_d^2 / B_0^2)^{1/3}$ is known as the magnetic stopping radius.

1.2 Piston-Ambient Plasma Coupling

The addition of an ambient plasma allows the LPP-driven magnetic cavity to develop into a magnetic piston, in which energy is transferred from the LPP to ambient ions. This energy transfer can be estimated by extending [6] the simple model of section 1.1.3. The initial kinetic energy E_d is now written as two terms

$$E_d = \left(\frac{B_0^2}{8\pi} + \frac{1}{2} m_a n_a v_d^2\right) \cdot \left(\frac{4\pi}{3} R^3\right) \tag{1.2}$$

where the first term is the same as Eq. 1.1 and the second is energy used to accelerate a mass density $m_a n_a$ of ambient ions to speed v_d. If all the energy is now used to accelerate ambient ions to v_d, the cavity will expand to the equal mass radius $R = R_M = (3N_d m_d / 4\pi m_a n_a)^{1/3}$. Note that since the ratio $R_B/R_M = M_A^{(2/3)}$, the requirement that $R_M < R_B$ or $M_A > 1$ must be met in order to transfer energy to the ambient ions, *i.e.* that the LPP ions be super-Alfvénic. Recall that $R_M/\rho_d > 1$ must also be satisfied, so that a fine balance between fast and magnetized LPP ions is necessary to effectively form a magnetic piston.

There has been much work done on the mechanism by which energy is transferred from LPP ions to ambient ions [77, 6, 33], though the topic is still an active area of research. Since the LPP-ambient ion-ion collisional mean free path is generally greater than the characteristic coupling interaction region (R_M) in the experiments detailed here, only collisionless coupling mechanisms will be considered. These mechanisms can be divided into turbulent or laminar processes.

1.2.1 Turbulent Coupling

In turbulent coupling, free energy drives instabilities that can transfer energy between LPP and ambient ions. The primary candidates are the modified two-stream instability and the ion-ion two-stream instability. It has been shown [60, 48] that the condition $M_A \lesssim (1+\beta_e)^{1/2}$ is required for the onset of these instabilities, where $\beta_e = 8\pi n_e k T_e / B_0^2$ and n_e and T_e are the electron density and temperature, respectively. For the experiments detailed here, $\beta_e \ll 1$, and so instabilities are not expected to play an important role in the coupling process for super-Alfvénic expansions.

1.2.2 Laminar Coupling

In laminar coupling, the generation of an electric field drives processes that couple LPP and ambient ions. The electric field is derived from the electron momentum equation [6, 33]

$$m_e n_e \frac{d\vec{v_e}}{dt} = -\nabla P_e - e n_e \left(\vec{E} + \vec{v_e} \times \vec{B}/c\right) + e n_e \eta \left(\vec{J_i} + \vec{J_e}\right) \tag{1.3}$$

where m_e, n_e, v_e, P_e, and $\vec{J_e}$ are the electron mass, density, drift velocity, pressure, and current density, respectively, and $\vec{J_i}$ and η are the ion current density and resistivity. Assuming the electron mass and resistivity are negligible and solving for $\vec{E}$ gives

$$\vec{E} = -\frac{1}{e n_e} \nabla P_e - \vec{v_e} \times \vec{B}/c \tag{1.4}$$

Neglecting the displacement current and solving for $\vec{v_e}$ from Ampere's Law yields

$$\vec{v_e} = \frac{1}{e n_e} \left(\sum_i \vec{J_i} - \frac{c}{4\pi} \nabla \times \vec{B}\right) \tag{1.5}$$

$$\vec{E} = -\frac{1}{e n_e} \nabla P_e - \frac{1}{4\pi e n_e} \vec{B} \times \left(\nabla \times \vec{B}\right) - \frac{1}{e n_e c} \sum_i \vec{J_i} \times \vec{B} \tag{1.6}$$

where the first term on the right in Eq. 1.6 is the electron pressure gradient, the second is the magnetic pressure and curvature, and the third is the Larmor term. Under the assumption

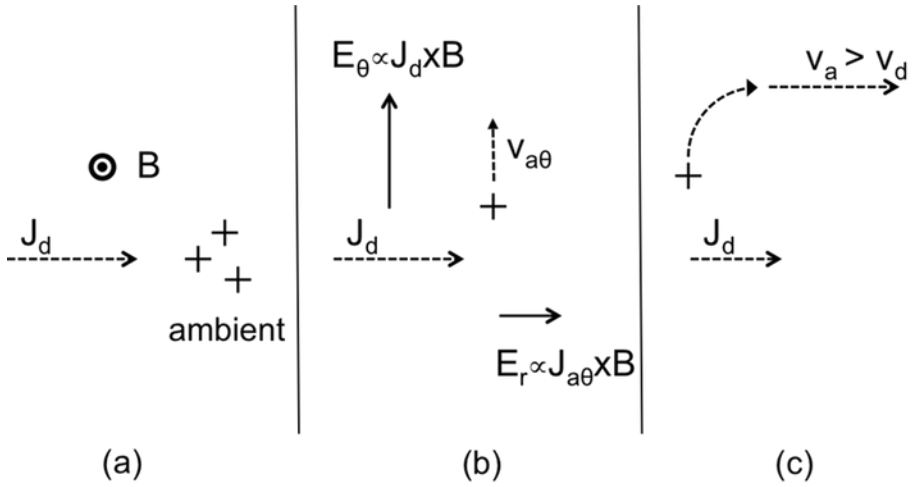

Figure 1.4: Diagram of Larmor coupling. (a) The ambient ions are assumed to be essentially stationary relative to a beam of LPP ions with current J_d. (b) The current J_d induces an azimuthal electric field E_θ. E_θ accelerates ambient ions, which induces a secondary radial electric field E_r. (c) The ambient ions begin to gyrate and are considered coupled if they are accelerated to a speed greater than the LPP ion speed by the time they are directed radially.

$\beta_e \ll 1$ from section 1.2.1, the magnetic pressure term is much larger than the electron pressure term. Furthermore, it can be shown [6] through simple scaling arguments that the ratio of the second and third terms goes like M_A^{-1}. Therefore, for super-Alfvénic expansions, Larmor coupling is expected to be the dominant mechanism for transferring energy between LPP and ambient ions in the magnetic piston.

The Larmor field can be understood as the electric field induced by a changing magnetic field responding to the LPP ion current [33]. Since the LPP ions are primarily moving radially and since the ambient ions are generally much lighter (typically H or He *vs.* C) and relatively stationary, this gives rise to an azimuthal electric field whose magnitude is mostly determined by the LPP ion radial speed and a radial electric field determined by the ambient ion azimuthal speed (since the ambient ions will respond more quickly to the induced azimuthal field). As the ambient ions are accelerated azimuthally, they will feel a Lorentz force that turns them into the radial direction after 1/4 gyroperiod. If the now radially-directed ambient ion velocity is greater than the LPP ion velocity, then the ambient

ions will remain ahead of the LPP ions, *i.e.* they will be coupled (see Fig. 1.4). Hewett *et al.* have derived an expression (assuming quasi-neutrality) for this condition in terms of the "coupling" parameter α

$$\alpha \equiv \left(\frac{\pi}{2} - 1\right) \frac{Z_{lpp} n_{lpp}}{Z_a n_a} \tag{1.7}$$

where the subscript corresponds to LPP or ambient ions, Z is the charge state, and n is the density. For $\alpha > 1$, ambient ions are coupled. In other words, for a fixed ambient density, as the LPP density or charge state is increased, a stronger azimuthal electric field is generated that can accelerate ambient ions to higher speeds and make it more likely that they will move as fast or faster than the LPP ions.

1.3 Collisionless Shock Formation

If ambient ions are sufficiently accelerated by the piston, their interaction[1] with unperturbed ambient ions (upstream ions) can lead to the formation of a collisionless shock through a theoretically well-characterized process (for an excellent review, see [79], [39], [10], or [81]).

1.3.1 Types of Magnetized Shocks

Collisionless shocks arise when a super-magnetosonic plasma flow (*e.g.* piston-driven ambient ions) encounters an obstacle (*e.g.* upstream ambient plasma) and collective electromagnetic effects lead to dissipation on length scales ($\sim c/\omega_{pi}$) much smaller than the classical mean free path. A typical shock geometry in shown in Fig. 1.5. The magnetosonic speed c_{ms} can be written as a function of the shock wave propagation angle θ_B relative to the magnetic field

[1]Note, while collisionless interactions between piston ions or piston and ambient ions have been emphasized, that condition is not necessary to form collisionless shocks. Only the interaction between the piston-accelerated ambient ions and the upstream ambient ions need be collisionless.

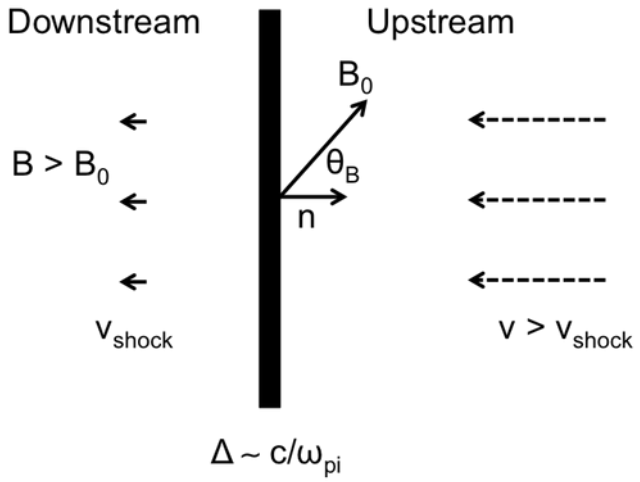

Figure 1.5: Geometry of a collisionless shock. The shock acts to slow incoming material and is compressive, so that magnetic field (and density) are higher downstream relative to upstream. Adapted from R.A. Truemann [81].

$$c_{ms}^2(\theta_B) = \frac{1}{2}\left[c_{ms}^2 \pm \left[\left(v_A^2 - c_s^2\right)^2 + 4v_A^2 c_s^2 sin^2(\theta_B)\right]^{1/2}\right] \tag{1.8}$$

where $c_{ms}^2 = v_A^2 + c_s^2$, v_A is the Alfvén speed, and c_s is the sound speed. From Eq. 1.8 it can be seen that three types of waves (shocks) can exist: fast, slow, and Alfvénic (or intermediate). Note that only fast mode shocks can propagate perpendicular to the magnetic field. Since for the experiments detailed in this work $v_A >> c_s$, super-Alfvénic and super-magnetosonic will be used interchangeably.

Shocks can be further classified by the angle θ_B as quasi-perpendicular ($\pi/4 < \theta_B \leq \pi/2$) or quasi-parallel ($0 \leq \theta_B < \pi/4$).

1.3.2 Criticality

Criticality is a measure of how well a shock can maintain itself through anomalous (since there are no classical collisions) resistive dissipation and is written in terms of a critical Mach number M_c, where $M < M_c$ is subcritical and $M > M_c$ is supercritical. A supercritical shock is unable to maintain itself solely through resistive dissipation. M_c depends on the plasma

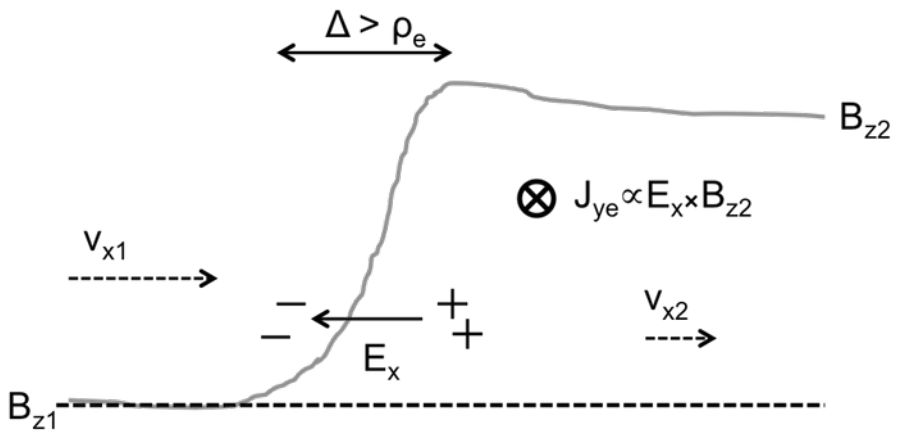

Figure 1.6: Diagram of a subcritical shock ramp. The ramp leading to a compressed magnetic field B_{z2} acts as a barrier to electrons, setting up a cross-ramp potential E_x. Since the electrons' gyroradii ρ_e are smaller than the ramp width Δ, they can $E_x \times B_{z2}$ drift within the ramp. This creates a cross-field current J_{ye} along the shock ramp, which acts as a source of free energy that can drive instabilities that provide dissipation. Adapted from R.A. Truemann [81].

β and θ_B, but the largest possible value is $M_c \approx 2.76$ (M_c increases as θ_B increases or β decreases).

1.3.3 Shock Formation

As a super-magnetosonic plasma flow impacts an obstacle, the obstacle reflects ions upstream, creating an ion-ion beam instability that generates magnetosonic waves traveling upstream. If the plasma flow is moving faster than the wave group velocity, the wave will begin to steepen and form wave trains. Dispersion leads to the formation of a solitary wave with a ramp steepness on the order of the ion inertial length. Upstream ions and electrons respond to this ramp with different gyroradii, producing a cross-ramp potential and cross-field drift (see Fig. 1.6).

For a subcritical shock, this drift can excite instabilities (most likely ion acoustic or lower hybrid [87, 88]) that provide anomalous resistivity. The resulting dissipation allows

the soliton to form into a shock. For a supercritical shock, instabilities are unable to provide sufficient dissipation. Instead, the reflection of in-flowing ions back upstream provides most of the dissipation.

1.4 Scope of Dissertation

This work is concerned with the generation of laboratory collisionless shocks by a laser-driven magnetic piston, the criteria necessary to form these shocks in the laboratory, and the laser plasma characterization necessary to calculate those criteria.

Chapter 3 presents experimental evidence and analysis of the first laser-driven, subcritical quasi-perpendicular magnetized collisionless shock. The analysis focuses specifically on the characterization of the shock and its relationship to shock features expected theoretically. Additionally, the shock is compared to features seen in experiments in which no shock or a pre-shock was created. The extent to which the different experimental outcomes can be organized by formation criteria, and hence the extent to which those criteria encapsulate the relevant shock formation physics, is also studied.

Chapter 4 addresses the issue of LPP characterization and its role in estimating initial plasma conditions necessary to calculate shock formation criteria. It will be shown that the assumption of a uniform, spherical laser plasma is no longer valid at the high laser intensities of interest in this work. Instead, experimental data, analytic modeling, and computational simulations are utilized to characterize and model the behavior of the LPP under a range of laser conditions. This work significantly expands upon previous efforts and extends the current understanding of piston development and its relation to shock generation. Additionally, the acquisition of experimental data on a LPP required the development of a Thomson scattering diagnostic effective in a novel parameter regime, in multiple environments, and in multiple configurations. The diagnostic also required building new operational capabilities and beam lines for the Phoenix laser system. This work is detailed in Chapter 5.

Producing a laboratory collisionless shock was a collaborative effort and significant achieve-

ment since, as outlined in previous sections, the creation of a laboratory collisionless shock requires the right balance of a fast piston, dense ambient plasma, and strong magnetic field, where any one works in opposition to one of the others. Extensive resources were required to build the hardware infrastructure and operating software necessary to run multiple automated high-energy laser and pulse power systems simultaneously and safely. This is detailed in the Appendices.

CHAPTER 2

Experimental Setups

As outlined in Chapter 1, generation of laboratory collisionless shocks requires a fine balance between the characteristics of the laser plasma, ambient plasma, and background magnetic field. This is most easily accomplished when each element (laser, plasma, field, *etc.*) can be controlled independently. To that end, shock experiments were initially performed on the Large Plasma Device [27] (LAPD) in combination with the Phoenix laser, both at UCLA. When it was determined that there was insufficient laser power and ambient density to generate a shock, a series of experiments were carried out at the Trident Laser Facility [51] at Los Alamos National Laboratory (LANL, see section 2.1), where multiple high-power lasers created both the ambient plasma and laser-produced plasma (LPP). While a shock precursor was generated [71], the ambient plasma was insufficiently tunable or characterized to generate a full-fledged shock. Recent upgrades have added a high-power laser (Raptor) to the Phoenix laboratory [56] and a large lanthanum hexaboride (LaB_6) cathode capable of generating higher-density ambient plasmas to the LAPD (see section 2.2). As a result, recent experiments have successfully generated a shock [70] at UCLA (see Chapter 3). Meanwhile, experiments have been carried out on smaller vacuum vessels in the Phoenix laboratory to characterize the LPP (see section 2.3).

A variety of diagnostics were utilized in these experiments. The primary diagnostic for studying the LPP was Thomson scattering (see Chapter 5). Where applicable, emissive spectroscopy and fast camera imaging were also used to study the LPP, while proton radiography was employed to characterize the diamagnetic cavity. The primary diagnostic for studying the structure of the shocks were magnetic flux ("bdot") probes.

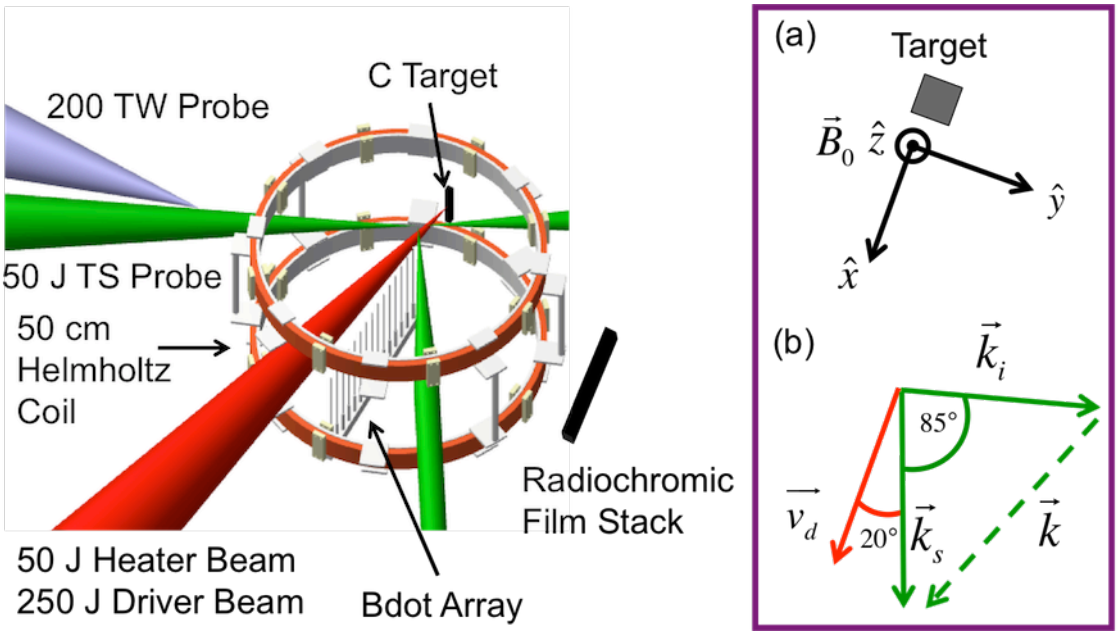

Figure 2.1: Schematic layout of the experiment on Trident. (a) Coordinate system of the experiment. (b) Scattering geometry for the Thomson diagnostic.

2.1 Trident Laser Facility

The Trident Laser Facility [51] consists of two independent laser systems coupled to a large vacuum chamber. A typical setup is shown in Fig. 2.1 and typical parameters are listed in Table 2.1. A graphite target was placed at the inner edge of a large (Ø50 cm) pulsed Helmholtz coil and was translated and/or rotated each shot for a fresh surface. The target surface normal was directed through the center of the coil and defined the $\hat{x}$ direction, while the central axis of the coil defined the $\hat{z}$ direction (see Fig. 2.1a). The coil could generate quasi-static ($\sim$ 1 ms) magnetic fields up to 1 kG along $\hat{z}$.

The experiment was performed in two stages. In the first ("heater") stage, a laser beam (1053 nm, 50 J, 1.5×10^{11} W/cm^2) ablated a plasma into a background magnetic field. After ≈ 7 μs, the background field had diffused back into the plasma, forming a magnetized ambient plasma. In the second ("driver") stage, a second pulse of the same laser beam (250 J, 6.5×10^{12} W/cm^2) created a super-Alfvénic plasma that expanded into the previously-formed ambient plasma. The delay between the heater and driver beams was variable up to

Laser Energy	(J)	50 (heater), 250 (driver)
Laser Intensity	(10^{11} W/cm^2)	1.5 (heater), 6.5 (driver)
Background Magnetic Field	(G)	< 1000
Ambient Plasma Species		C
Ambient Plasma Ion Density	(cm^{-3})	5×10^{13}

Table 2.1: Typical parameters for a Trident experiment.

10 μs. Note that the driver beam hit the same spot on the target as the heater beam.

2.1.1 Magnetic Flux Probes

A modular array – consisting of 40 probe slots spaced 1 cm apart – of single-axis, non-differential 1 mm bdot probes was aligned along $\hat{x}$. The probes measured the $\hat{z}$ component of the magnetic field up to 40 cm from the target. Signals were passed though a custom Delrin flange with BNC feedthroughs and digitized by 500 MHz, 9-bit or 125 MHz, 12-bit scopes.

2.1.2 Thomson Scattering

A second laser beam line was configured as a Thomson-scattering probe (527 nm, 50 J, 10^{11} W) to characterize the ambient plasma and could be delayed arbitrarily relative to the heater beam. The beam was polarized along $\hat{z}$ and focused through an f/12 phase plate. Scattered light was collected from a 0.04 mm^3 volume positioned $3 - 18$ cm along $\hat{x}$ at an angle of 85° relative to the Thomson beam and 20° relative to $\hat{x}$ (see Fig. 2.1b). The scattering volume was defined by the beam waist (100 μm), the projection of the spectrometer slit width (100 μm) oriented along the beam, and the detector CCD size (4 mm) in the spatial dimension. The scattered light was collimated by an f/8 plano-convex lens and imaged by an f/4 achromatic lens with magnification 2 onto an f/4 0.25 m Chromex 250 imaging spectrometer (1200 grooves/mm grating blazed at 500 nm). The light was detected by a

Princeton Instruments (PI) MAX intensified charge-coupled device (ICCD) gated camera with a 10 ns exposure. The images had a spectral resolution of 0.6 nm, a spectral field of view of 30 nm, and a spatial resolution of 7 μm along the Thomson beam. Emissive spectra from the ambient plasma were also collected with the Thomson signal.

A black anodized plate angled away from the collection axis served as the viewing dump, while a baffle placed in the exit port of the probe beam acted as a beam dump. A KG3 bandpass filter placed in front of the spectrometer slit blocked light above 800 nm, including stray light from the heater and driver beams. Stray light from the probe beam was blocked by a 3 mm wide ($\Delta\lambda \approx 8$ nm) hard aperture mask placed directly in front of the detector CCD. The Thomson collection system was aligned using a Ø1 mm stainless steel pin placed inside a Ø1.9 mm pyrex capillary tube to facilitate scattering. The probe beam was focused onto the tip of the pin and adjusted along $\hat{z}$ to center the pin image on the detector.

In order to get absolute density calibrations, Rayleigh scattering measurements were taken in air with chamber fill pressures of 0.1-550 Torr and a 50 mJ probe beam in the same setup as the Thomson diagnostic (see Chapter 5 for details on Rayleigh scattering).

2.1.3 Proton Radiography

The Thomson beam line could also be configured as a high-intensity, short-pulse drive beam (200 TW, 10^{19} W/cm^2, 500 fs) for a proton deflectometry probe to map magnetic fields [25]. The short-pulse beam was focused onto a 10 μm Cu foil, creating an intense MeV proton backlighter that was imaged through a fiducial grid at the edge of the Helmholtz coil onto a large (8.5 $\times$ 11") radiochromic film stack, comprised of 4 layers plus a 7 μm Al low-energy filter. The film captured the deflection of the protons in the $\hat{x}$-$\hat{y}$ plane in an image of the $\hat{x}$-$\hat{z}$ plane.

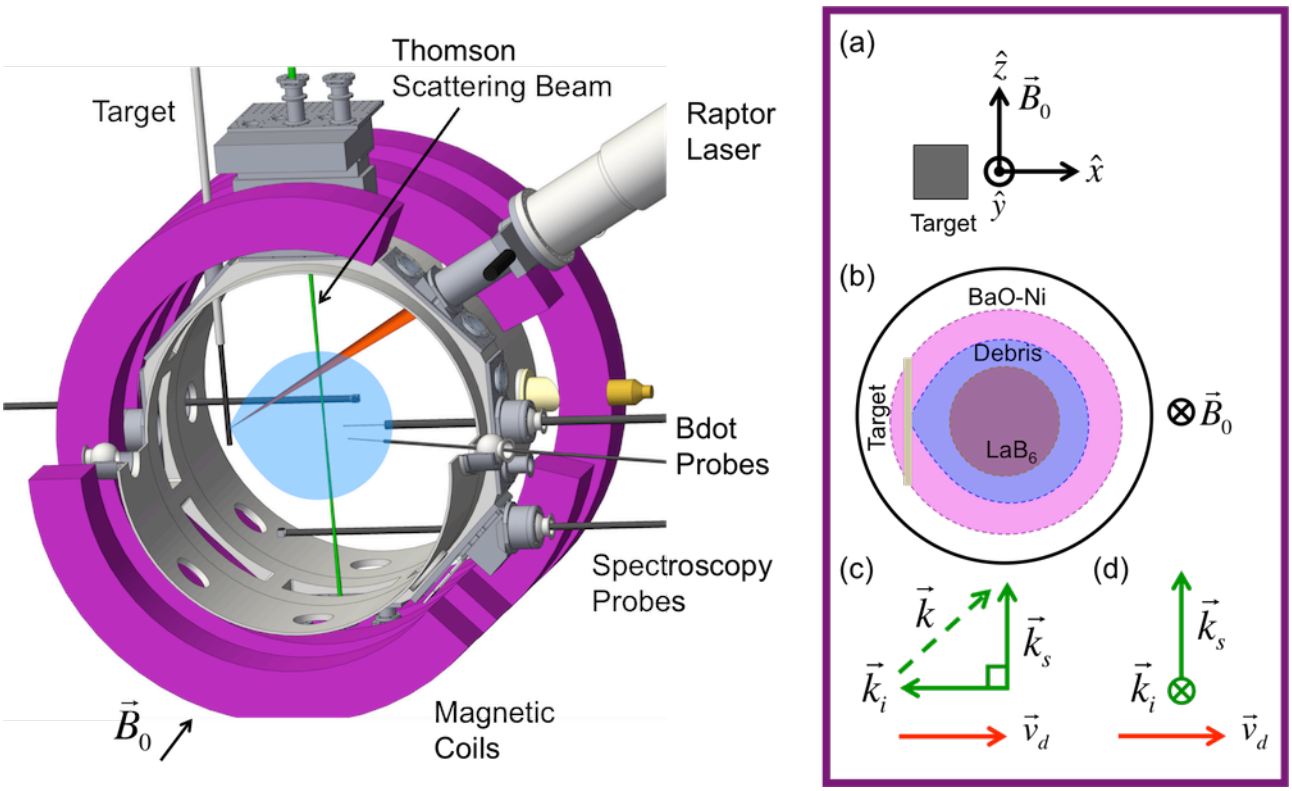

Figure 2.2: Schematic layout of an experiment on the LAPD. (a) Coordinate system of the experiment. (b) Cartoon cross-section of the LAPD plasma in a two-cathode configuration. (c) Scattering geometry for the Thomson diagnostic in a horizontal ($\hat{x}$) configuration. (d) Scattering geometry for the Thomson diagnostic in a vertical ($\hat{y}$) configuration.

2.2 Large Plasma Device

The Large Plasma Device (LAPD) [27] is a large scale (18 m long by Ø1 m) facility that provides a well-characterized and highly-reproducible magnetized ambient plasma. The plasma is steady-state (10 ms), quiescent and current-free, and customizable in both background magnetic field (0.2 - 1.8 kG) and ambient gas fill (H_2, He, Ne, Ar). A BaO-coated Ni cathode generates the main Ø60 cm plasma ($n_a \sim 2\times10^{12}$ cm^{-3}) while a second LaB_6 (lanthanum hexaboride) cathode generates a smaller Ø40 cm core plasma ($n_a \sim 2\times10^{13}$ cm^{-3}) roughly centered on the main plasma (see Fig. 2.2b). The ambient plasma has a typical electron temperature $T_e = 6$ eV and ion temperature $T_i = 1$ eV. The background field is oriented

Laser Energy	(J)	20 - 200
Laser Intensity	(10^{11} W/cm^2)	0.8 - 40
Background Magnetic Field	(G)	200 - 400
Ambient Plasma Species		H, He
Ambient Plasma Ion Density	(cm^{-3})	5×10^{12} - 2×10^{13}

Table 2.2: Typical parameters for a LAPD experiment.

axially along the machine and defines $\hat{z}$, with $\hat{x}$ oriented horizontally perpendicular to the field and $\hat{y}$ oriented vertically (see Fig. 2.2a).

A typical experimental setup and parameters are shown in Fig. 2.2 and Table 2.2, respectively. A graphite or HDPE (high-density polyethylene C_2H_4) target was embedded in the LAPD ambient plasma 30 cm from the machine center axis. The target was translated and/or rotated every shot for a fresh surface. Since the laser-ablated plasma is always directed normal to the target surface, the target can be rotated relative to the background field to study different shock geometries. For quasi-perpendicular shocks, the target normal was oriented along $\hat{x}$. The Raptor laser (20-200 J) was focused through a 1.8 m focal-length lens to a 0.5-2 mm^2 spot on the target at a 30° angle relative to the target normal.

2.2.1 Magnetic Flux Probes

The evolution of the magnetic field was measured with a variety of differentially-wound bdot probes. Single-axis bdots measured the $\hat{z}$ component of the field up to 60 cm from the target along $\hat{x}$. Individual probes were positioned in 1 cm increments with 1-3 shots taken per position, while a "5-tip" probe containing 5 bdot cores spaced 1 cm apart was incremented in 5 cm steps with generally 1 shot per position. Additional tri-axis bdots measured all three components of the field up to 10 m from the target along $\hat{z}$. The probe signals were sent though custom-built 150 MHz differential amplifiers and coupled to fast (1.25 GHz) 10-bit digitizers. Additional details on the design and construction of these probes can be found in

[22].

2.2.2 Thomson Scattering

A Thomson scattering diagnostic was employed to study the ablated plasma. A frequency-doubled beam (532 nm, 10 J) from the Phoenix laser was polarized along $\hat{z}$ and focused through a 1.5 m focal length lens along $\hat{x}$ up to 30 cm from the target (see Fig. 2.2c). The Thomson beam was angled such that it terminated on the target surface or was slightly offset so that it terminated in a long tube behind the target, though in both cases this created considerable stray light. The beam could be delayed arbitrarily relative to the ablator beam. The light was scattered from a 0.43 mm^3 volume defined by the beam waist (50 μm), the projection of the spectrometer slit width (500 μm) oriented along the beam, and the detector CCD size (17.2 mm) in the spatial dimension. The scattered light was collected by a custom-built fiber-optic probe (see Chapter 5) 30 cm downfield ($z = z_0 + 30$) at a 90° angle relative to the target normal. The light was collected through a 75 mm focal length lens with a demagnetization of 6 and coupled through 40 100-μm UV-grade glass fibers to a 1/4 m Acton spectrometer (1200 grooves/mm grating blazed at 500 nm) with a custom-built fiber-optic face plate. A PI MAX 4 ICCD camera imaged the scattered light with a 3 ns gate width. The resulting image had a spatial resolution of 0.15 mm along the beam, a spectral resolution of 0.29 nm, and a spectral field of view of 31 nm.

The Thomson beam was aligned with a custom-built probe inserted into the LAPD from behind the target (this necessitated raising the target for alignment). The probe consisted of a hollow tube with a window on the air-side and one of two caps on the vacuum side. Each cap could hold an alignment pin consisting of a Ø0.8 mm steel wire encased in a Ø1 mm hollow pyrex capillary tube (for isotropic scattering) and glued into a alumina ceramic tube (for stability). One cap was a disk with a small hole in the center that oriented the pin along $\hat{x}$ (for aligning the beam along $\hat{y}$) while the other cap was a disk with a lip that oriented the pin along $\hat{y}$ (for aligning along $\hat{x}$).

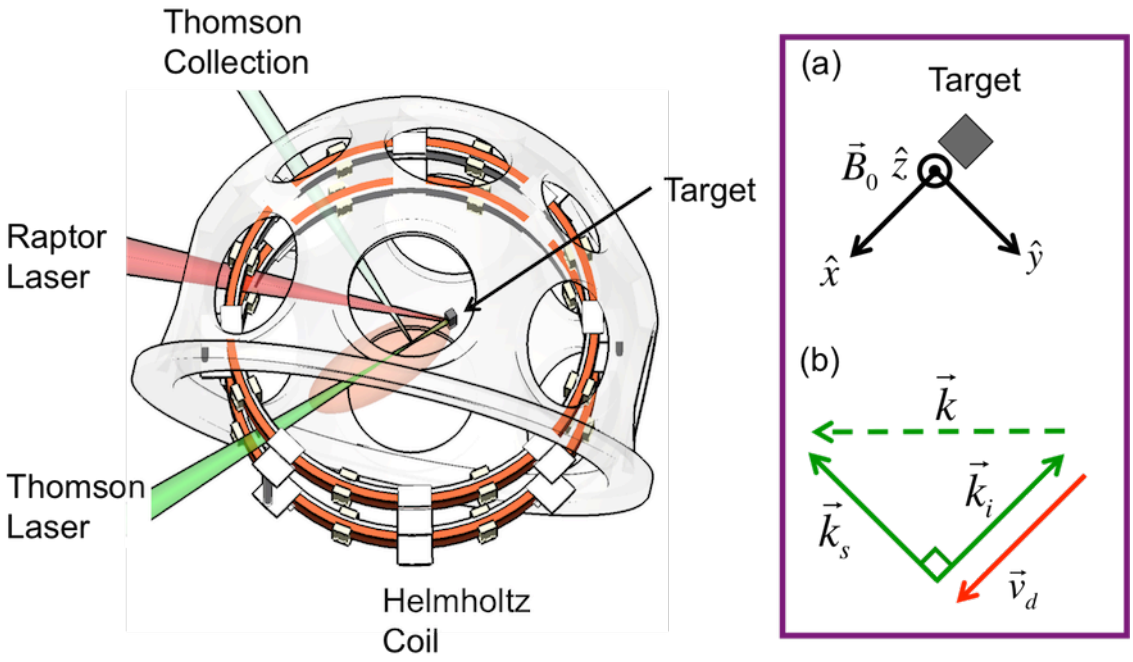

Figure 2.3: Schematic layout of the experiment on a Phoenix chamber. (a) Coordinate system of the experiment. (b) Scattering geometry for the Thomson diagnostic.

An attempt was made to measure electron heating in the shock ramp. For this purpose, the Thomson probe was offset 2.5 cm along $\hat{z}$ (to avoid other probes) and focused along $\hat{y}$ 30 cm from the target (see Fig. 2.2d). Additional baffles were added to the input and output windows to reduce stray-light and a Thorlabs BT610 beam trap placed at the output window was used to terminate the beam. This successfully reduced stray light by a factor of 10 compared to the horizontal Thomson-scattering beam setup.

2.3 Phoenix Vacuum Chamber

Experiments to characterize the LPP were carried out on a small (Ø50 cm) spherical vacuum chamber in the Phoenix laboratory. A typical setup is shown in Fig. 2.3 and typical parameters are listed in Table 2.3. A graphite target was placed at the inner edge of a large (Ø50 cm) pulsed Helmholtz coil and was translated and/or rotated each shot for a fresh surface. The target surface normal defined the $\hat{x}$ direction, while the central axis of the coil defined

Laser Energy	(J)	40 - 100
Laser Intensity	(10^{11} W/cm^2)	0.2 - 5
Background Magnetic Field	(G)	0 - 1000
Ambient Plasma Species		–
Ambient Plasma Ion Density	(cm^{-3})	–

Table 2.3: Typical parameters for a Phoenix experiment.

the $\hat{z}$ direction (see Fig. 2.3a). The coil could generate quasi-static ($\sim$ 1 ms) magnetic fields up to 1 kG along $\hat{z}$. The Raptor laser (40-100 J) was focused through a 1.8 m focal-length lens to a 0.5-4 mm^2 spot on the target at a $\sim 40^\circ$ angle relative to the target normal.

2.3.1 Thomson Scattering

The frequency-doubled Phoenix beam (523 nm, 20 J) served as a Thomson scattering probe and was polarized along $\hat{z}$ and focused along $\hat{x}$ up to 10 cm from the target (see Fig. 2.3b). The beam terminated at the target surface and was delayed up to 10 μs after Raptor. The light was scattered from a 0.06 mm^3 volume defined by the beam waist (10 μm), the projection of the spectrometer slit width (500 μm) oriented along the beam, and the detector CCD size (12 mm) in the spatial dimension. Scattered light was collected along $\hat{y}$ through baffled tubes (with additional baffled tubes acting as a viewing dump) and imaged (magnification 1) through a multiple-lens system onto a 3/4 m SPEX 1702 spectrometer (1200 grooves/mm grating blazed at 300 nm). The light was captured by a PI MAX 2 ICCD camera with a 10 ns exposure. The resulting image had a spatial resolution of 96 μm along the beam, a spectral resolution of 0.05 nm, and a spectral field of view of 13.3 nm.

The Thomson beam was aligned with a Ø1 mm stainless steel pin encased in a Ø1.9 mm pyrex capillary tube (to facilitate scattering) and mounted on a 3D picomotor drive. A low-power beam could be scattered off the pin tip to align the beam along $\hat{z}$ or the pin could be backlit (*e.g.* calibration lamp) to image the pin in two dimensions (using a large

slit width) to orient the beam in the $\hat{x}$-$\hat{y}$ plane. The pin was lowered between alignments.

Rayleigh scattering measurements were taken as necessary to get absolute density calibrations. The Thomson beam was reused in the same configuration but with a laser energy of 100 mJ. The chamber was filled with air at pressures of 1-760 Torr, with the signal at 1 Torr acting as a stray-light and background fiducial. The air was allowed to settle overnight at 1 Torr, and the chamber was slowly vented to take measurements at higher pressures.

2.3.2 Emissive Spectroscopy

The chamber was also used for emissive doppler spectroscopy measurements using the same collection optics as for the Thomson scattering probe. In this case the target was relocated so that the Raptor beam was oriented normal to the target surface, and the collection optics imaged a plane 5 cm from the target along $\hat{x}$. This allowed spatially-integrated, time-resolved ($\sim$ 50 ns) doppler measurements of carbon charge states CI - CV (C^{+0} - C^{+4}) up to 2200 ns after target ablation. The spectra were resolved by a 3600 grooves/mm grating blazed at 300 nm and spatially binned into a 1D image for a spectral resolution of $\sim$ 0.02 nm.

CHAPTER 3

Generation of Quasi-Perpendicular, Magnetized Collisionless Shocks

Magnetized collisionless shocks are a challenging experimental problem. As outlined in Chapter 1, they are ubiquitous in space and astrophysical plasmas. However, generating them in a laboratory setting requires a sufficiently high-energy piston to drive ions to super-Alfvénic speeds, a sufficiently large magnetic field for those ions to be considered magnetized, and enough space and time for the ions to form a shock. Too much piston energy and too little magnetic field, too little energy and too large a field, or too few ions and the process fails. Unsurprisingly, then, creating magnetized collisionless shocks in the laboratory has met with limited success since the 1960s [63, 2, 65]. Even then, the shock was strictly perpendicular and could not separate from the piston [61, 30, 18, 78], limiting the experiments' relevance to space shocks.

By using a high-energy laser to drive a magnetic piston through a large-scale magnetized ambient plasma, experiments at UCLA have demonstrated a quasi-perpendicular, magnetized collisionless shock [70, 57]. This process was originally proposed in [20], first carried out at UCLA in [15], and expanded upon in [55, 71, 73, 56, 11, 58]. Because the flexibility of the laser allows non-perpendicular geometries, and because the piston is only temporarily tied to the shock, these experiments allow more control over shock formation and evolution than the original ones on θ-pinches.

The process of generating a collisionless shock with a magnetic piston itself has several challenging experimental components. To understand the composition of the piston, the laser-produced plasma (LPP) that forms the piston must be well-characterized. The

method(s) by which the piston couples energy to the ambient ions must be understood in order to maximize the coupling efficiency. The structure and evolution of the piston-accelerated ions must be studied to confirm shock formation. Finally, once a shock has formed, new diagnostics and techniques will be needed to probe and control its behavior.

This chapter is concerned with the formation and characteristics of a laboratory magnetized collisionless shock, its relationship to previously observed non-shocks and pre-shocks, and the conditions under which such shocks can be expected to form. A comprehensive analysis of the LPP is presented in Chapter 4 and is used to calculate shock formation criteria and how well those criteria encapsulate shock formation physics in Section 3.3. An overview of the coupling process is given in Chapter 1, though in general the mechanics of coupling is beyond the scope of this dissertation. Experiments studying the behaviors of fully formed shocks are left as future work.

Section 3.1 reviews some theory of magnetized collisionless shocks, including what features are expected in experiments. Section 3.2 details the hybrid simulations that are compared to the experimental results of Section 3.3. Section 3.4 summarizes important findings.

3.1 Theory

A comprehensive theoretical treatment of collisionless shocks can be found in [79], [39], and [81]. Only those components relevant to laboratory shocks will be discussed here (a brief outline of the theory is also given in Chapter 1 and reproduced in part here for convenience).

A shock is created when a flow moving faster than the local sound speed encounters an obstacle. The obstacle serves to slow down the flow. Because the oncoming flow is faster than the sound speed, information about the obstacle cannot propagate quickly enough upstream to directly affect particles. To compensate, a region is established that acts to slow the incoming flow at the expense of increased entropy. In other words, the shock converts the high ram, low thermal pressure flow upstream (the region that shock has not reached) to a low ram, high thermal pressure flow downstream (the region the shock has passed). In

a collisionless shock, the transition region (shock layer) is much smaller than the classical mean free path.

Here, the relevant sound speed is the magnetosonic speed $c_{ms}^2 = v_A^2 + c_s^2$ – where v_A is the Alfvén speed and c_s is the sound speed – and, for the plasmas of interest, can usually be approximated $c_{ms} \approx v_A$. The magnetosonic speed $c_{ms}(\theta_B)$ can be further written as a function of the shock wave propagation angle θ_B relative to the magnetic field

$$c_{ms}^2(\theta_B) = \frac{1}{2}\left[c_{ms}^2 \pm \left[\left(v_A^2 - c_s^2\right)^2 + 4v_A^2 c_s^2 sin^2(\theta_B)\right]^{1/2}\right] \tag{3.1}$$

As a result, shocks can be classified by the angle θ_B as quasi-perpendicular ($\pi/4 < \theta_B \leq \pi/2$) or quasi-parallel ($0 \leq \theta_B < \pi/4$). The experiments detailed here then involve quasi-perpendicular, fast mode shocks.

Using the magnetohydrodynamic (MHD) equations for a single-fluid plasma, and assuming a planar shock, relationships between the upstream and downstream values of density n, velocity v, magnetic field B, and pressure P can be derived. These are known as the Rankine-Hugoniot (RH) jump conditions, and describe the global (far from the shock layer) conservation of energy across the shock. Note that they cannot address how energy is partitioned microscopically in the shock layer. For a strictly perpendicular shock ($\theta_B = \pi/2$) and assuming an ideal gas equation of state [10, 81], the jump conditions become

$$\frac{v_2}{v_1} = \frac{n_1}{n_2} = \frac{B_1}{B_2} = \frac{1}{8}\left[1 + (1 + 2.5\beta_1)M_A^{-2} + \left[\left[1 + (1 + 2.5\beta_1)M_A^{-2}\right]^2 + 2M_A^{-2}\right]^{1/2}\right] \tag{3.2}$$

where $M_A^{-1} = B_1/\sqrt{4\pi m n_1 v_1^2} = v_A/v_1$, $\beta_1 = 8\pi n_1 T_1/B_1^2$, T_1 is the total temperature, and the subscripts 1 and 2 denote the upstream and downstream regions, respectively. As can be seen in Eq. 3.2, the magnetic field and density downstream of the shock increase by the same amount as the velocity decreases. For the marginal $\beta \sim 1$, quasi-perpendicular, low-Mach number plasmas in the experiments, Eq. 3.2 can be approximated as $B_2/B_1 \approx M_A$, *etc.* (see Fig. 3.1). Also note that the temperature downstream is always larger than the

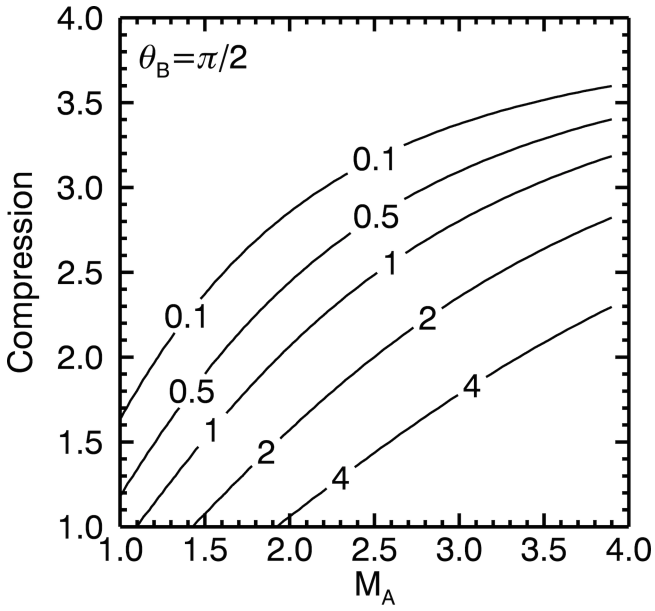

Figure 3.1: Compression ratio (ratio of downstream to upstream value) versus Alfvénic Mach number M_A for a strictly perpendicular ($\theta_B = \pi/2$) planar shock with lines (solid) of constant $\beta = 8\pi nT/B^2$. For $\beta \sim 1$, the compression ratio increases as the Mach number for $M_A \lesssim 3$.

upstream temperature ($T_2/T_1 > 1$), *i.e.* the shock heats the plasma (the entropy is also strictly increasing).

Shocks can be further classified by their criticality, a measure of how well a shock can maintain itself through anomalous (since there are no classical collisions) resistive dissipation. Criticality is expressed in terms of a critical Mach number M_c, where $M < M_c$ is subcritical and $M > M_c$ is supercritical. A supercritical shock is unable to maintain itself solely through resistive dissipation. M_c depends on the plasma β and θ_B, but the largest possible value is $M_c \approx 2.76$ (M_c increases as θ_B increases or β decreases) [46, 39]. For the experiments detailed here, the shocks are generally subcritical.

For subcritical shocks, the process by which the shock forms is theoretically well understood [79]. As a super-magnetosonic plasma flow impacts an obstacle, the obstacle reflects ions upstream, creating an ion-ion beam instability that generates magnetosonic waves traveling upstream. If the plasma flow is moving faster than the wave group velocity, the wave will begin to steepen and form wave trains. Dispersion leads to the formation of a solitary

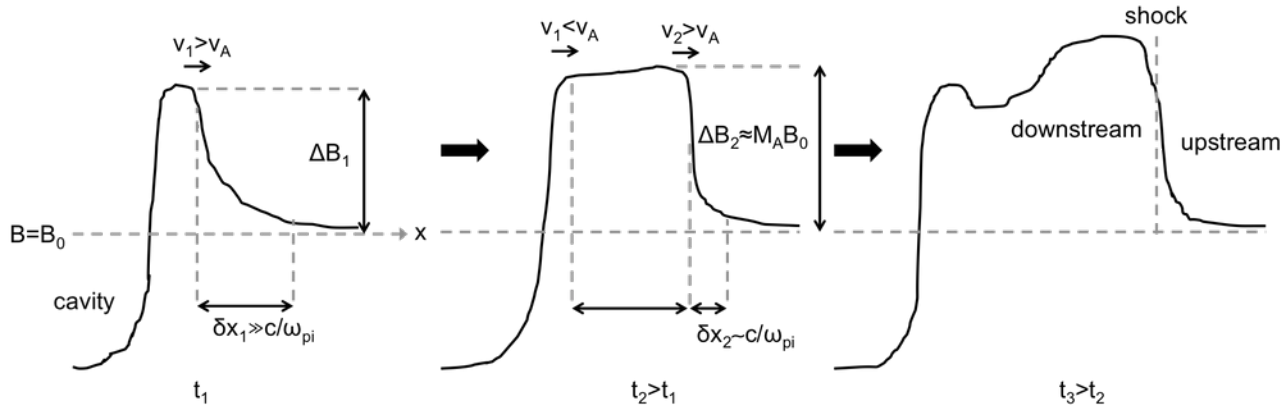

Figure 3.2: Diagram of the shock formation process with a magnetic piston. At t_1, a super-Alfvénic piston forms a diamagnetic cavity and magnetic field compression at the cavity edge. The width of the compression's leading ramp is much larger than an ion inertial length c/ω_{pi}. At later times ($t_2 > t_1$), a shock begins to form as piston-accelerated ambient ions overrun unperturbed ions. The forming shock (still moving super-Alfvénically) separates from the piston as the piston loses energy. The shock compression goes like the Mach number, and the shock ramp is on the order of an ion inertial length. Late in time (t_3), the shock has fully formed and separated from the piston.

wave with a ramp steepness on the order of the ion inertial length. Upstream ions and electrons respond to this ramp with different gyroradii, producing a cross-ramp potential and cross-field drift. This drift can excite instabilities that provide anomalous resistivity, which results in dissipation that allows the soliton to form into a shock. The exact instabilities responsible remain undetermined (though they are most likely the ion acoustic or lower hybrid instabilities).

From the above considerations and experimental conditions, a quasi-perpendicular, fast mode, low-Mach number, subcritical shock is expected with a shock layer thickness on the order of an ion inertial length and magnetic field compression similar to the Mach number. Fig. 3.2 shows a diagram of the process by which the shock is expected to form (in terms of the magnetic field, though the process should be similar for the ambient density). Initially, a diamagnetic cavity and compression at the cavity edge are formed by the piston. The

compression moves super-Alfvénically, and the leading ramp of the compression is much larger than an ion inertial length due to faster ions slipping through. Later in time, a shock begins to form as piston-accelerated ambient ions overrun unperturbed ions. As the piston loses energy, a large compression width develops as the shock separates from the slowing cavity edge. The leading compression ramp also steepens. Late in time, the shock has separated from the piston, with a well-defined shock ramp and downstream region.

In addition to the shock features expected, the formation process places limits on the conditions under which a collisionless shock will form. In the shock frame, the upstream ions with flow v_0 must, of course, be super-Alfvénic ($M_A = v_0/v_A > 1$). The collisional mean free path between shocked ions must be larger than their gyroradii ($\lambda_{ii,s} > \rho_{a,s}$, where $\rho_{a,s} = v_s/\Omega_{ci,s}$, $\Omega_{ci,s} = Z_a e B_s/m_a c$, $v_s \approx v_0/M_A$, and $B_s \approx M_A B_0$ is the compressed magnetic field for low-Mach number shocks). In order to setup a cross-ramp potential, the shocked ions must be sufficiently magnetized [20], *i.e.* their gyroradii must be less than the system size ($\mu = D_0/\rho_{a,s} > 1$). This is equivalent to the condition that the upstream ions have sufficient time to establish the cross-ramp potential ($T = D_0/v_s > \Omega_{ci,s}^{-1}$). The system size D_0 is defined as the distance from the target to the edge of the (suitable) ambient plasma.

Shocks can be further (though incompletely) characterized by a coupling parameter ϵ that helps distinguish when a shock will form. The parameter was originally derived by Bashurin *et al.* [4] using the equal charge radius $R_* = (3N_d Z_d/4\pi Z_a n_a)^{1/3}$. A modified version using the equal mass radius is given by

$$\epsilon = \frac{R_M^2}{\rho_d\ \rho_a} = \left(\frac{R_M}{\rho_d}\right)^2 \left(\frac{m_d\ Z_a}{m_a\ Z_d}\right) \tag{3.3}$$

where $R_M = (3N_d m_d/4\pi m_a n_a)^{1/3}$, $\rho_d = v_0\ m_d c/(eZ_d B_0)$, $\rho_a = v_0\ m_a c/(eZ_a B_0)$, v_0 is the piston speed, and the subscripts refer to debris and ambient ions, respectively. Note that this parameter was derived strictly for large-Mach number shocks, so its application is approximate. Simulations [11] suggest $\epsilon \gtrsim 0.5$ is necessary for shock formation.

3.2 Simulations

Two-dimensional (2D) hybrid simulations were used to study the process of shock formation. Detailed information on the simulation models can be found in [86] and [11]. The simulations utilize a 2D3V collisionless magnetostatic hybrid code in two Cartesian spatial dimensions with three-dimensional fields and velocities. The magnetostatic approximation neglects the displacement current in Ampere's law so that effects on the order of the electron plasma frequency (ω_{pe}) are ignored. The ions are simulated kinetically using the particle-in-cell technique, while the electrons are treated as an inertial-less, charge-neutralizing fluid. The electrons are treated adiabatically, such that at a given time, the electron temperature is given by $T_e(x) = T_{e0}(n_e(x)/n_0)^{\gamma-1}$, where γ is the adiabatic index (usually $\gamma = 5/3$). The simulations do not include the laser-target interaction, but focus on a plasma expanding out from a planar target perpendicular to a uniform magnetic field into an ambient plasma at experimental conditions.

The above simulation model is valid for collective plasma behavior that occurs over multiple ion inertial lengths (c/ω_{pi}) and over multiple ion gyroperiods ($2\pi\Omega_{ci}^{-1}$). The simulations are resolvable below the ion inertial length, but may not be accurate at cell sizes approaching the electron inertial length. Because the displacement current is neglected and the electrons are treated as a fluid, the simulation cannot directly model subcritical shock formation, since that requires higher-frequency electron effects. Nonetheless, there is generally sufficient dissipation due to ion reflection from the shock ramp, even at low Mach numbers, for collisionless shocks to form.

In Fig. 3.3, a simulation under representative laboratory conditions illustrates the main features expected in experiments. The simulation domain consisted of 240×240 cells, each of size $0.133c/\omega_{pi}$, along $\hat{x}$ and $\hat{y}$. The simulation was initialized with a uniform ambient H plasma with density $n_a \sim 10^{13}$ cm^{-3} (about 100 macro [representative] particles per cell) and temperature $T_a \sim 1$ eV. The laser plasma (debris) ions were initialized in the center of the simulation domain with a Gaussian distribution spanning a few cells. The

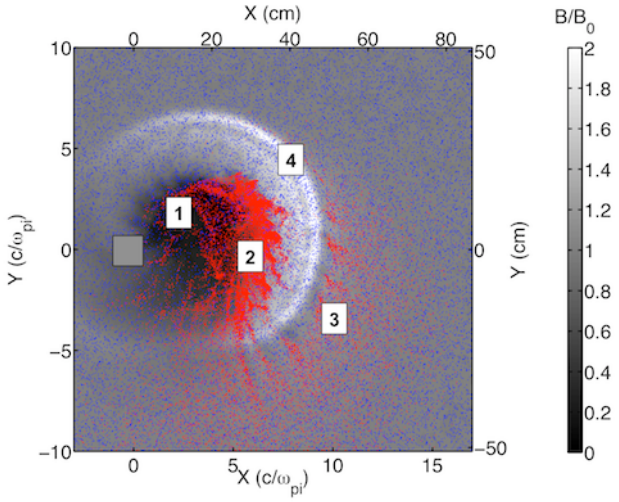

Figure 3.3: A 2D spatial contour plot at late time from a hybrid simulation initialized to representative experimental parameters, showing the basic features seen in experiments. Red and blue dots are debris and ambient ions, respectively, while the contour is the scaled magnetic field amplitude in $\hat{z}$. The target is represented by the solid gray box at (0,0) and is irradiated by a laser (not part of simulation) from $+\hat{x}$. Labeled in the figure are: (1) the formation of a magnetic cavity by the piston; (2) the piston edge coming to a stop as debris energy is transferred to the ambient plasma; (3) fast debris ions decoupling and slipping through the background; (4) a low-Mach number quasi-perpendicular collisionless shock separating from the piston.

debris ions (C^{+4}) were set up with a thermal distribution corresponding to $T_d \sim 1$ eV and to expand cylindrically outward with a speed of $M_A \sim 2$. The electrons were initialized with a temperature $T_{e0} \sim 5$ eV. An initial magnetic field $B_0 \sim 200$ G was oriented out of the simulation plane ($\hat{z}$). The simulation shows: the formation of a diamagnetic cavity and sweeping out of ambient ions by the piston; the coupling of energy between the piston and ambient ions and subsequent stagnation of the piston; the decoupling of faster debris ions; and the formation of a low-Mach number collisionless shock. Simulations for specific experimental parameters are presented in Section 3.3.

Run	E_0 (J)	I_0 (10^{11} W/cm^2)	Target	B_0 (G)	n_a (10^{12} cm^{-3})	Ambient Plasma
Run 1	19 ± 1	5 ± 2	C	275	5 ± 1	He^{+1}
Run 2	90 ± 5	1.4 ± 0.3	C	200	5 ± 1	H^{+1}
Run 3	180 ± 10	50 ± 20	C	400	50 ± 25	C^{+4}
Run 4	190 ± 10	12 ± 5	C_2H_4	300	12 ± 1	H^{+1}

Table 3.1: Summary of collisionless shock experiments. E_0 and I_0 are the average laser energy and intensity, respectively, for each run. n_a is the peak ambient ion density. Note that while Run 4 used a plastic (C_2H_4) target, measurements and simulations show no significant effect from the H debris. However, the plastic target allowed much higher laser intensities than a graphite (C) target.

3.3 Results

To illustrate the characteristics of shock formation in a laboratory setting, several representative experimental runs with a range of laser energies, intensities, background magnetic fields, and ambient plasma conditions were selected, each carried out on either the Large Plasma Device (LAPD) or the Trident Laser Facility (see Sections 2.2 and 2.1, respectively). A summary of the runs is given in Table 3.1. In general, each run took magnetic flux measurements over multiple laser shots along $\hat{x}$, the axis parallel to the debris blowoff and perpendicular to both the target surface and background magnetic field. All measurements are of the $\hat{z}$ component (along the field) of the magnetic field. Runs on the LAPD utilized a two-cathode configuration that generated a uniform low-density background plasma and a higher-density core plasma (see Fig. 2.2). Runs on Trident utilized a two-beam configuration, in which the first beam created a background plasma and the second beam drove the piston (see Fig. 2.1).

The runs were chosen to emphasize different features of shock formation: weakly coupled systems were no shock forms; moderately coupled systems where a pre-shock forms; and strongly coupled systems where a full shock forms (see Fig. 3.5). Note that moderately

coupled runs are generally capable of evolving into a full shock, but lack suitable ambient conditions for enough space or time. For each run, space-time plots of magnetic field amplitude and corresponding spatial and temporal lineouts are provided. Where possible, data is compared to vacuum (no ambient plasma) conditions. Since shock formation strongly depends on ambient density, ambient density profiles are also provided, if available. In the following, the ion inertial length c/ω_{pi} and ion gyro-frequency Ω_{ci}^{-1} are given in terms of ambient ion conditions as listed in Table 3.1, and unless otherwise stated, distances are relative to the target and times are relative to laser ablation.

3.3.1 Weak Coupling

Fig. 3.6 shows results from Run 1 (see Table 3.1), carried out on the LAPD. This run lies in the weak coupling regime, in which the piston fails to transfer significant energy to the ambient plasma. The resulting magnetic field structures are very similar to the sub-Alfvénic features seen in [65, 85, 13]. As is typical in sub-Alfvénic cases, at early times ($t = 200$ ns or $\sim 0.1\ \Omega_{ci}^{-1}$) the ramp of the compression is shallow and ends at the cavity edge (*i.e* no pulse width, see Fig. 3.6d). This is due to the decoupling of faster debris ions that carry some magnetic compression with them. At peak compression ($t = 549$ ns or $\sim 0.4\ \Omega_{ci}^{-1}$), the magnetic pulse has begun to broaden, indicating some ambient effect, but its leading edge remains shallow. Furthermore, while the Mach number of the compression ranges from $M_A = 2.7 - 3.7$ between the cavity and leading edges (also indicative of pulse broadening, see Fig. 3.6a-b), the amplitude of the compression only reaches a maximum of $B_z/B_0 = 1.3 \pm 0.1$, which is inconsistent with the RH conditions. By $t = 800$ ns ($\sim 0.5\ \Omega_{ci}^{-1}$), the compression remains broad but weakly compressed with a shallow ramp. Unlike the following runs, the ambient density remains largely uniform throughout the experiment. This suggests that weak coupling prevents a shock from forming, despite favorable ambient conditions.

3.3.2 Moderate Coupling

Runs 2 (Fig. 3.7) and 3 (Fig. 3.8) represent moderate coupling, in which a pre-shock forms. A pre-shock has sufficient initial conditions to begin shock formation (unlike the weak coupling case), but fails to fully steepen due to a lack of space, time, and/or uniform ambient density.

Like Run 1, Run 2 (also carried out on the LAPD) has at early times (t = 500 ns or $\sim 1.3\ \Omega_{ci}^{-1}$) a compression with a shallow ramp ending at the cavity edge (see Fig. 3.7d). Unlike Run 1, however, the compression continues to grow until reaching a maximum value $B_z/B_0 = 1.7 \pm 0.1$ at $t = 1.1\ \mu$s ($\sim 1.9\ \Omega_{ci}^{-1}$) and $x = 29$ cm ($0.9 \pm 0.1\ \rho_d$). Since the compression is also moving at $M_A = 1.8 \pm 0.1$ (see Fig. 3.7a-b), it is consistent with the RH conditions for low-Mach number shocks. Additionally, comparing the magnetic field profile with and without an ambient plasma indicates a strong ambient effect (see Fig. 3.7c). The compression with ambient plasma is stronger and has a steeper temporal ramp (but comparable breadth). The compression's leading edge also arrives faster, while its cavity edge is slower, indicating coupling with the ambient plasma. The initial conditions thus suggest the beginning of shock formation. However, as the magnetic pulse reaches its maximum compression, the ambient density falls significantly (see Fig. 3.7d). This causes the local Alfvén speed to increase and the pulse to become sub-Alfvénic. As a result, the compression fails to steepen or separate and instead dissipates.

Run 3 (carried out on Trident) exhibits similar behavior to Run 2 despite significantly different ambient conditions. Here, the compression moves at $M_A = 1.5 \pm 0.4$ and reaches a maximum value of $B_z/B_0 = 1.6 \pm 0.1$ at $t = 530$ ns ($\sim 0.6\ \Omega_{ci}^{-1}$) and $x = 8$ cm ($1.4 \pm 0.2\ \rho_d$). Again, this is consistent with the RH conditions. Like Run 2, the compression with ambient plasma is different than without. Also like Run 2, the compression fails to steepen or separate and dissipates at later times.

A hybrid simulation of Run 3 initialized to the experimental conditions shows similar features to the experiment (see Fig. 3.9). The ambient plasma had a Gaussian density

distribution centered on the initial debris distribution. The debris plasma consisted of a cloud of C^{+4} ions that expanded out conically at $M_A \sim 2$. In Fig. 3.9c, the simulation shows the formation of a magnetic compression consistent with the RH jump conditions. However, it also shows that the ambient density, while compressed from piston coupling, fails to remain tied to the magnetic compression due to insufficient magnetization. This is also seen in Fig. 3.9d, where there are no reflected ambient ions in phase space at the leading edge of the magnetic pulse.

3.3.3 Strong Coupling

Results from Run 4 (Fig. 3.10) indicate a strong coupling regime in which a shock has formed (though it does not fully separate from the piston). The run was a carried out on the LAPD. Like the previous runs, Run 4 shows signs of moderate coupling at $t = 280$ ns ($\sim 0.6\ \Omega_{ci}^{-1}$, see Fig. 3.10d). The leading edge of the compression moves at $M_A = 1.5 \pm 0.1$ with a magnetic compression $B_z/B_0 = 1.6 \pm 0.1$ (consistent with RH conditions), but has a shallow ramp. However, the compression continues to grow until reaching a maximum value at $t = 708$ ns ($\sim 1.9\ \Omega_{ci}^{-1}$) and $x = 29$ cm ($0.9 \pm 0.1\ \rho_d$), at which point the pulse has a considerably different structure. The compression has increased to $B_z/B_0 = 2.0 \pm 0.1$ and moves at $M_A = 2.1 \pm 0.1$, also consistent with the RH conditions. The ramp of the compression, though, has steepened to a width $\delta = 0.5 \pm 0.2\ c/\omega_{pi}$. Furthermore, the width of the pulse has increased to $\Delta = 1.4 \pm 0.2\ c/\omega_{pi}$, showing a significant separation of the front of the compression from the cavity edge. This can also be seen in the difference between the speeds of the front ($M_A = 2.1 \pm 0.1$) and back ($M_A = 1.6 \pm 0.1$) of the compression (see Fig. 3.10a-b). Since each of these features is expected to increase with time as the shock forms, further evidence of shock formation comes from tracking them in time (see Fig. 3.4).

Like the moderate coupling runs, comparison to shots taken in vacuum under the same conditions indicate that the above features are tied to the ambient plasma. At $x = 37$ cm ($1.2 \pm 0.1\ \rho_d$), the magnetic pulse in vacuum has a much shallower ramp. Though the width of the pulse in vacuum is broader than seen in previous runs, it is nonetheless much

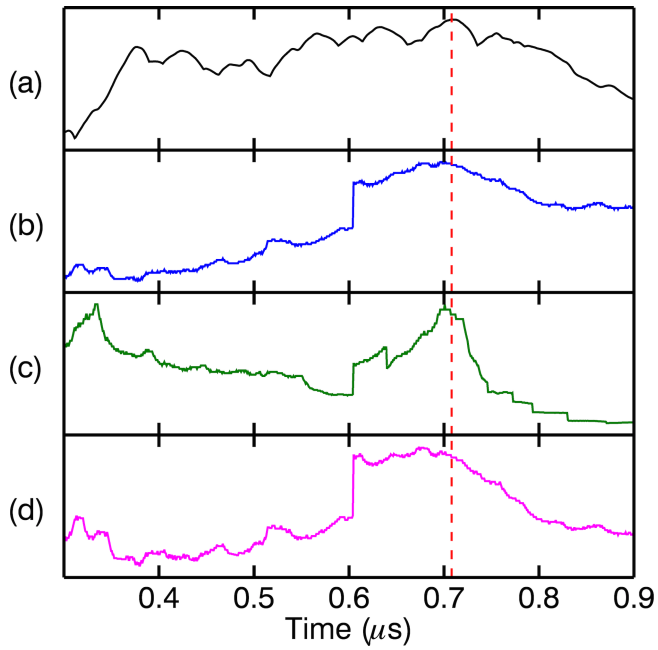

Figure 3.4: Evolution of shock formation for Run 4. (a) Peak magnetic field amplitude. (b) Magnetic pulse width, defined as the distance between the first and last point where the field reaches 60% of its maximum. (c) Pulse ramp steepness, defined as the change in field over the distance between the edge of the pulse and where the field is 5% above background. (d) Ratio of pulse ramp speed to cavity speed. In (b)-(d), there is a sudden change around $t = 600$ ns, with all values reaching a maximum at or near the time of maximum field amplitude (dashed), as expected for a shock. Afterwards, all values dissipate as the pulse enters a low-density regime. All values are in normalized units.

narrower than the corresponding pulse with ambient plasma. Furthermore, the cavity moves more slowly with an ambient plasma (350 vs. 390 $\pm$ 20 km/s), consistent with energy being coupled to the ambient ions, while the leading magnetic compression moves more quickly (530 vs. 420 $\pm$ 10 km/s), consistent with a pulse that is being carried by accelerated ambient ions.

Similar to Runs 2 and 3, by $t = 940$ ns ($\sim 2.5\ \Omega_{ci}^{-1}$) the compression has entered a region of significantly reduced ambient density. This causes both the Alfvén speed and ion inertial length to increase, decreasing and smearing out the leading edge of the magnetic

compression.

The above results were compared to 2D hybrid simulations initialized to the same experimental conditions (see Fig. 3.11). The simulations used a two-component ambient plasma, with one uniform low-density plasma covering the entire simulation domain, and another high-density Gaussian component centered $\sim 4\ c/\omega_{pi}$ from the initial debris distribution. The debris plasma consisted of a cloud of C^{+4} ions that expanded out conically at $\pm 75^{\circ}$ at $M_A = 2.65$. As can be seen in Fig. 3.11a-b, the formation of a low-Mach number collisionless shock is also reproduced in the simulations. In particular, a magnetic and ambient density compression consistent with the jump conditions is seen in Fig. 3.11c, while a small population of reflected ambient ions from the shock front is seen in Fig. 3.11d. The simulations also show the dissipation of the shock as it leaves the high-density ambient plasma (see Fig. 3.11a), consistent with experimental observations.

3.3.4 Shock Formation Criteria

As detailed in Sections 3.3.1-3.3.3, the shock experiments yielded a variety of results that fell into the categories of weak, moderate, and strong coupling. It is of interest then to determine whether the shock criteria outlined in Section 3.1 can accurately capture these differences, which would indicate that these criteria are encapsulating the physics of laboratory shock formation.

In order to calculate the criteria, in particular ϵ, it is necessary to have information on the initial state of the laser plasma (piston). This is estimated from the results of Chapter 4. Specifically, laser-target simulations benchmarked by experiments and empirical scaling laws provided a range of particle number and charge state values for various laser intensities. The total number of ablated particles was calculated from the experimental laser intensity, and using both the measured intensity and expansion speed, interpolated average ablated charge states for that speed were estimated. Together with the experimental ambient conditions, this allowed a calculation of the equal mass radius R_M, debris gyroradius ρ_d, and ambient

Condition	Run 1	Run 2	Run 3	Run 4
$M_A > 1$	2.8	1.3	1.5	1.9
$\epsilon > 0.5$	0.04	0.9	1.3	0.6
$\mu > 1$	0.8	0.7	0.4	1.8
$\lambda_{ii,s}/\rho_{a,s} > 1$	$\gg 1$	$\gg 1$	$\gg 1$	$\gg 1$
$\beta > 1$	0.7	1.3	0.1	1.9

Table 3.2: Criteria necessary for shock formation for runs from Table 3.1. $M_A = v_0/v_A$ is the Alfvénic Mach number, where v_0 is the shock speed (generally the piston expansion speed). $\epsilon = R_M^2/\rho_d\rho_a$ is the coupling parameter, where $R_M = (3N_d m_d/4\pi m_a n_a)^{1/3}$, $\rho_d = v_0 \cdot m_d c/Z_d e B_0$, and $\rho_a = v_0 \cdot m_a c/Z_a e B_0$. The magnetization parameter $\mu = D_0/\rho_{a,s}$ is defined with respect to the shocked ambient ions, where D_0 is the system size, $\rho_{a,s} = v_s/\Omega_{ci,s}$, $\Omega_{ci,s} = Z_a e B_s/m_a c$, $v_s \approx v_0/M_A$, and $B_s \approx M_A B_0$ is the compressed magnetic field for low-Mach number shocks. $\lambda_{ii,s}$ is the shocked ambient ion-ion collisional mean free path, $\beta = 1/2\ n_{a,s} m_a v_s^2/8\pi B_s^2$, and $n_{a,s} \approx M_A n_a$.

gyroradius ρ_a, and hence ϵ.

The shock formation criteria for the experimental results are summarized in Table 3.2. As can be seen, only Run 4 satisfies all formation conditions, consistent with the measurements from Section 3.3.3 that indicate a collisionless shock formed. While a super-Alfvénic expansion, sufficient coupling, and high β were achieved in most cases, the most difficult criteria to satisfy was sufficient magnetization μ. This in turn appears to be most sensitive, not to the ambient density or magnetic field (though increasing both helps), but rather to the amount of space available with suitable ambient conditions. In both Runs 2 and 3, a shock appeared to be forming, but the ambient density profile collapsed too close to the target and no shock formed. In contrast, in Run 4 the ambient density remained high long enough for the shock to form, though it collapsed before the shock could separate from the piston.

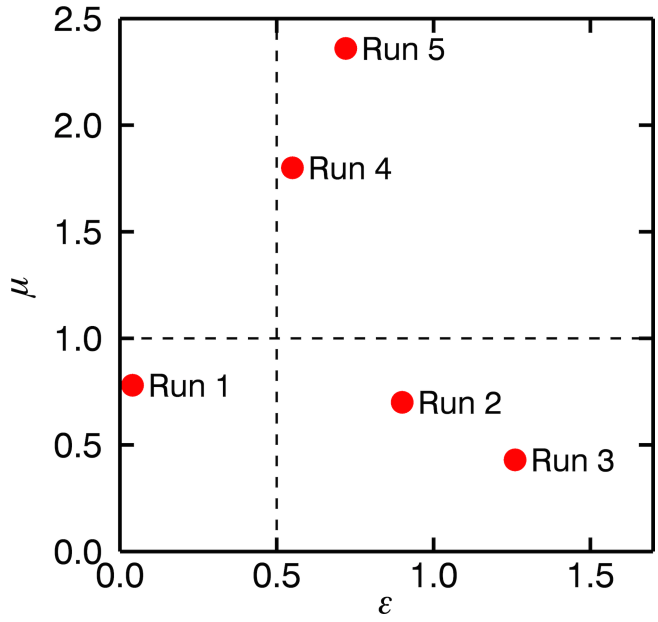

Figure 3.5: Location of experimental runs (solid circles) in an ϵ-μ parameter space. From the location of the runs, it can be seen that values of $\epsilon < 0.5$ and $\mu < 1$ correspond to weak coupling, values of $\epsilon > 0.5$ and $\mu < 1$ correspond to moderate coupling, and values of $\epsilon > 0.5$ and $\mu > 1$ correspond to strong coupling and are necessary for shock formation (see Section 3.3.4). Run 5 had the same experimental conditions as Run 4 but with a background magnetic field of 400 G. Note that continuing to increase μ will eventually cause $M_A < 1$.

These results can also be organized using just an $\epsilon - \mu$ parameterization, as show in Fig. 3.5. It can be seen that the experiments fall into distinct regions corresponding to weak ($\epsilon < 0.5$, $\mu < 1$), moderate ($\epsilon > 0.5$, $\mu < 1$), and strong ($\epsilon > 0.5$, $\mu > 1$) coupling. This indicates that both parameters are capturing much of the physics of piston coupling (ϵ) and shock formation (μ).

Since the results of Chapter 4 allow the shock criteria to be calculated for a range of laser intensities and ambient densities, it is possible to place Runs 1-4 in a larger experimental parameter space. Figures 3.12 and 3.13 show each run and its location relative to contours of relevant shock criteria. It can be seen, for example, that in order for Run 2 to achieve $\mu > 1$ at the same laser intensity, it would require only a small increase in the peak ambient density, though at the expense of coupling. Not coincidentally, this would place Run 2 in

a very similar regime as Run 4. It can also be seen that it would be possible for Run 4 to increase ϵ by increasing B_0 without becoming sub-Alfvénic or unmagnetized, potentially forming a stronger shock. A higher B_0 would also allow a higher ambient density to be used, increasing μ without sacrificing much coupling. Since ϵ is only weakly dependent on intensity, any of the runs could achieve increased magnetization and Mach number by increasing laser intensity.

3.4 Summary

Experiments carried out on the LAPD and Trident Laser Facility, in conjunction with a theoretical framework for subcritical shocks and the results of Chapter 4, yielded the following results:

- Combining a laser-driven magnetic piston with a large, pre-formed magnetized ambient plasma has allowed a unique investigation into collisionless shock formation not readily available to spacecraft.
- A magnetized, quasi-perpendicular, sub-critical collisionless shock was observed, though it did not fully separate from the piston. 2D hybrid simulations initialized to the same experimental conditions reproduced the features seen in experiments.
- Several criteria for shock formation were investigated, the two most important of which appear to be the coupling parameter ϵ and magnetization parameter μ. Previous work and simulations suggests values of $\mu > 1$ and $\epsilon > 0.5$ are necessary for shock formation.
- The results of several experiments in which no shock, a pre-shock, or a full shock formed allowed the experiments to be organized by weak, moderate, or strong coupling. Those categories, in turn, were found to correspond to distinct regions in an $\epsilon - \mu$ parameter space, where values of $\epsilon < 0.5$ and $\mu < 1$ indicate weak coupling, values of $\epsilon > 0.5$ and $\mu < 1$ indicate moderate coupling, and values of $\epsilon > 0.5$ and $\mu > 1$ indicate strong coupling. The results of Chapter 4 were critical in calculating reasonable values of ϵ.

- Using the results of Chapter 4, the experimental runs and shock criteria were extended into a larger experimental parameter space, which may help optimize formation conditions for future shock experiments.

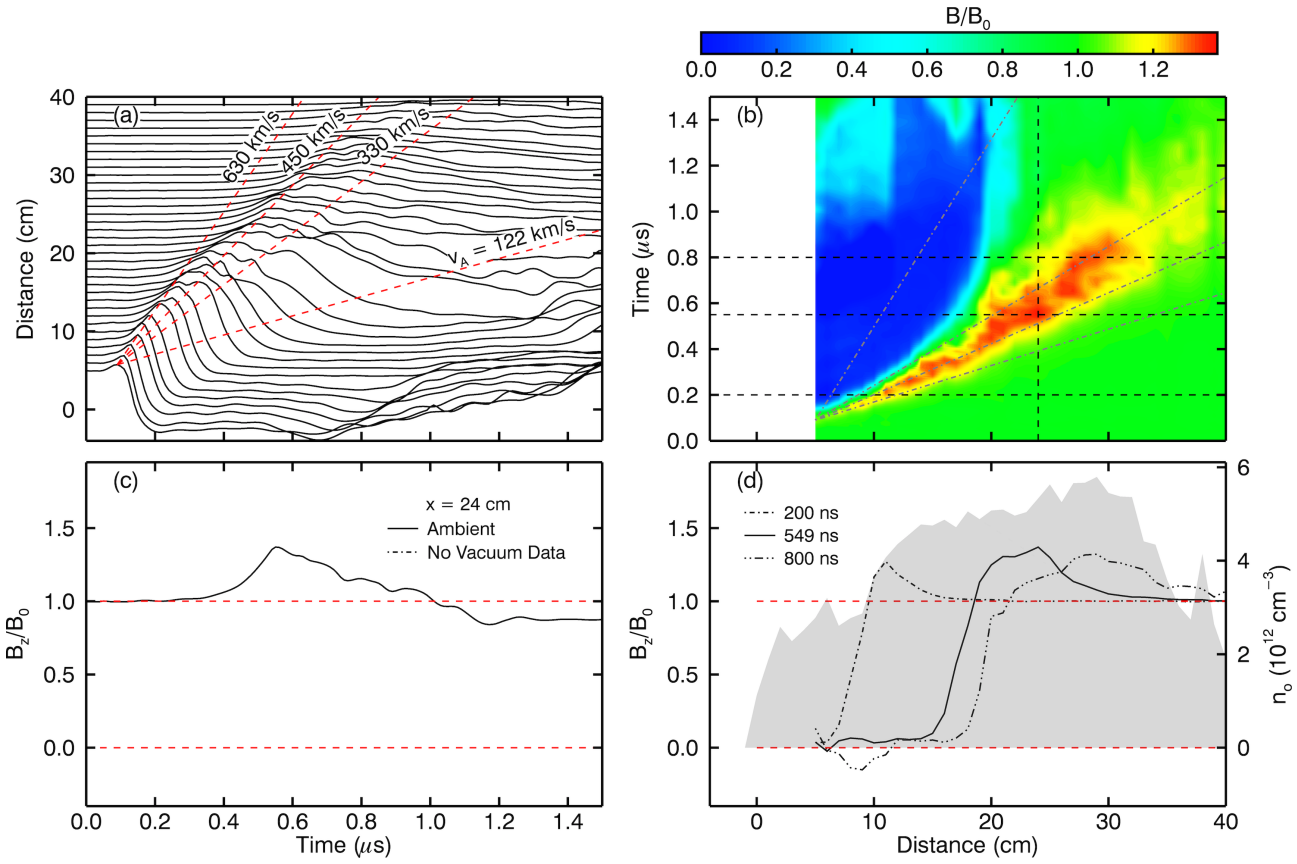

Figure 3.6: Results from shock experiment Run 1 (see Table 3.1). (a) Stacked temporal plots of magnetic field amplitude with velocity lines (dashed). (b) Contour streak plot of normalized magnetic field. Also shown are spatial and temporal lineouts (dashed) and velocity lines (dot-dash). (c) Spatial lineout from (b) containing maximum compression. (d) Temporal lineouts from (b), including at maximum compression (solid). The ambient density profile is also shown (gray overlay). The results indicate no shock or pre-shock is formed, consistent with a weak coupling regime.

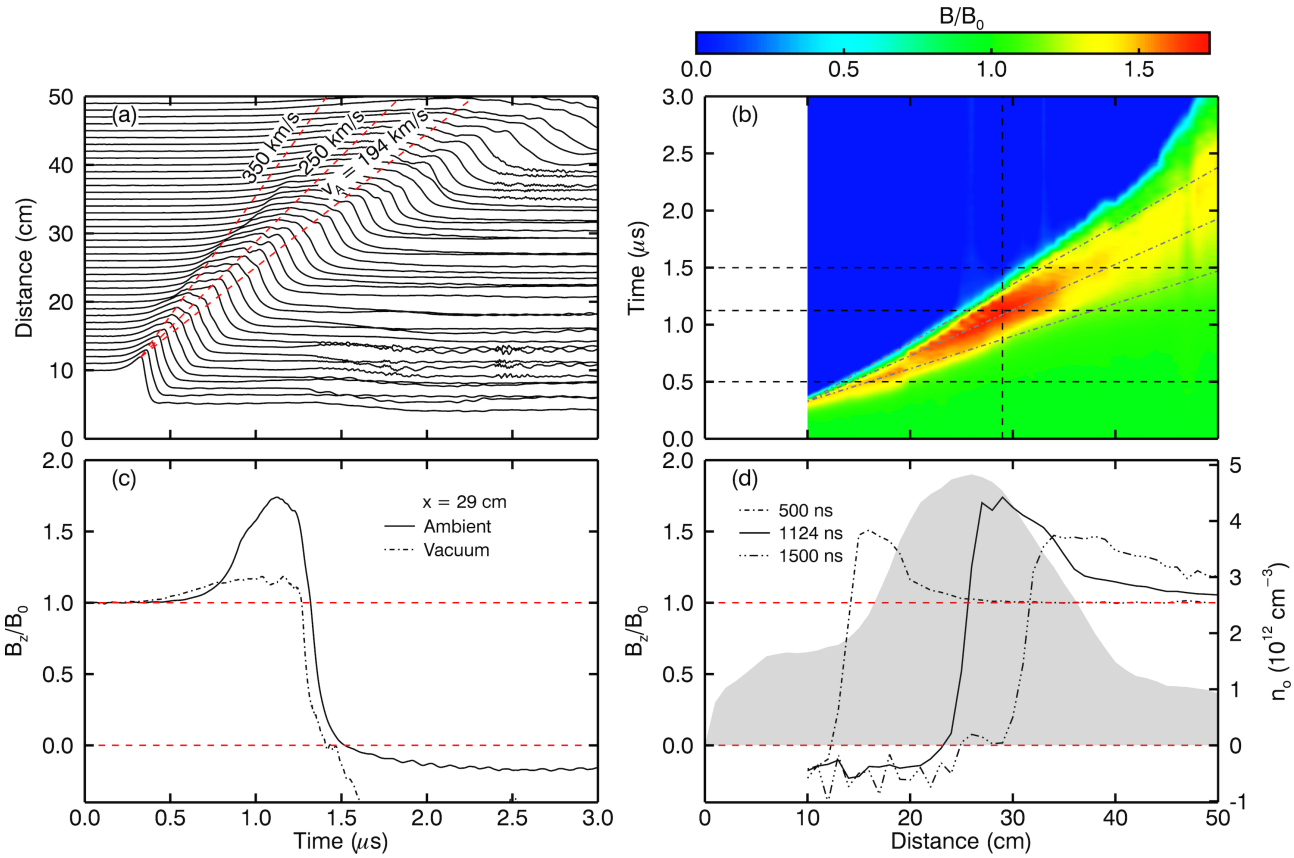

Figure 3.7: Results from shock experiment Run 2 (see Table 3.1). (a) Stacked temporal plots of magnetic field amplitude with velocity lines (dashed). (b) Contour streak plot of normalized magnetic field. Also shown are spatial and temporal lineouts (dashed) and velocity lines (dot-dash). (c) Spatial lineout from (b) containing maximum compression and corresponding vacuum profile. (d) Temporal lineouts from (b), including at maximum compression (solid). The ambient density profile is also shown (gray overlay). The results indicate that a pre-shock formed but did not have sufficiently uniform ambient density to steepen and separate from the piston.

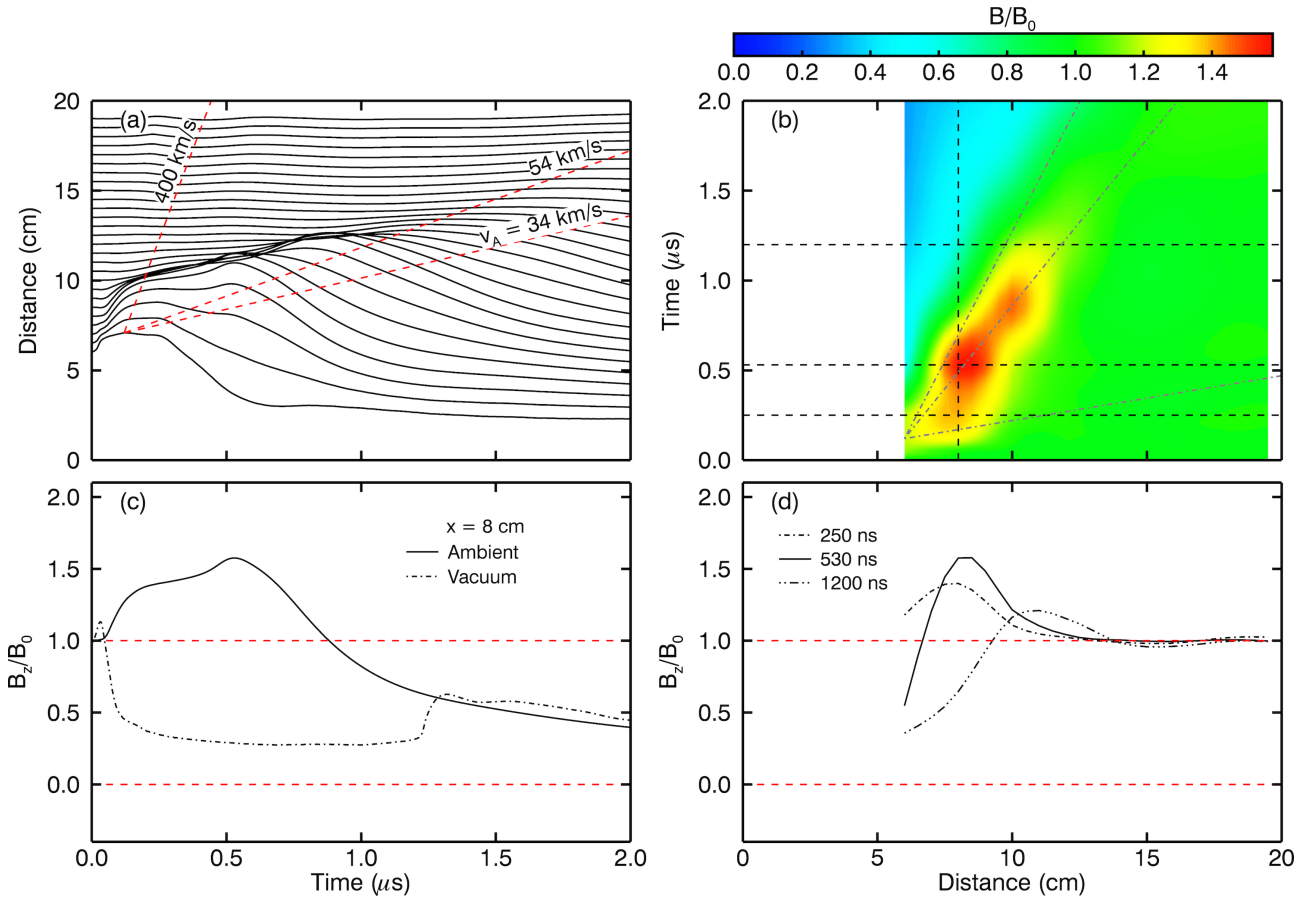

Figure 3.8: Results from shock experiment Run 3 (see Table 3.1). (a) Stacked temporal plots of magnetic field amplitude with velocity lines (dashed). (b) Contour streak plot of normalized magnetic field. Also shown are spatial and temporal lineouts (dashed) and velocity lines (dot-dash). (c) Spatial lineout from (b) containing maximum compression and corresponding vacuum profile. (d) Temporal lineouts from (b), including at maximum compression (solid). The results indicate that a pre-shock formed, though it was unable to fully steepen or separate from the piston.

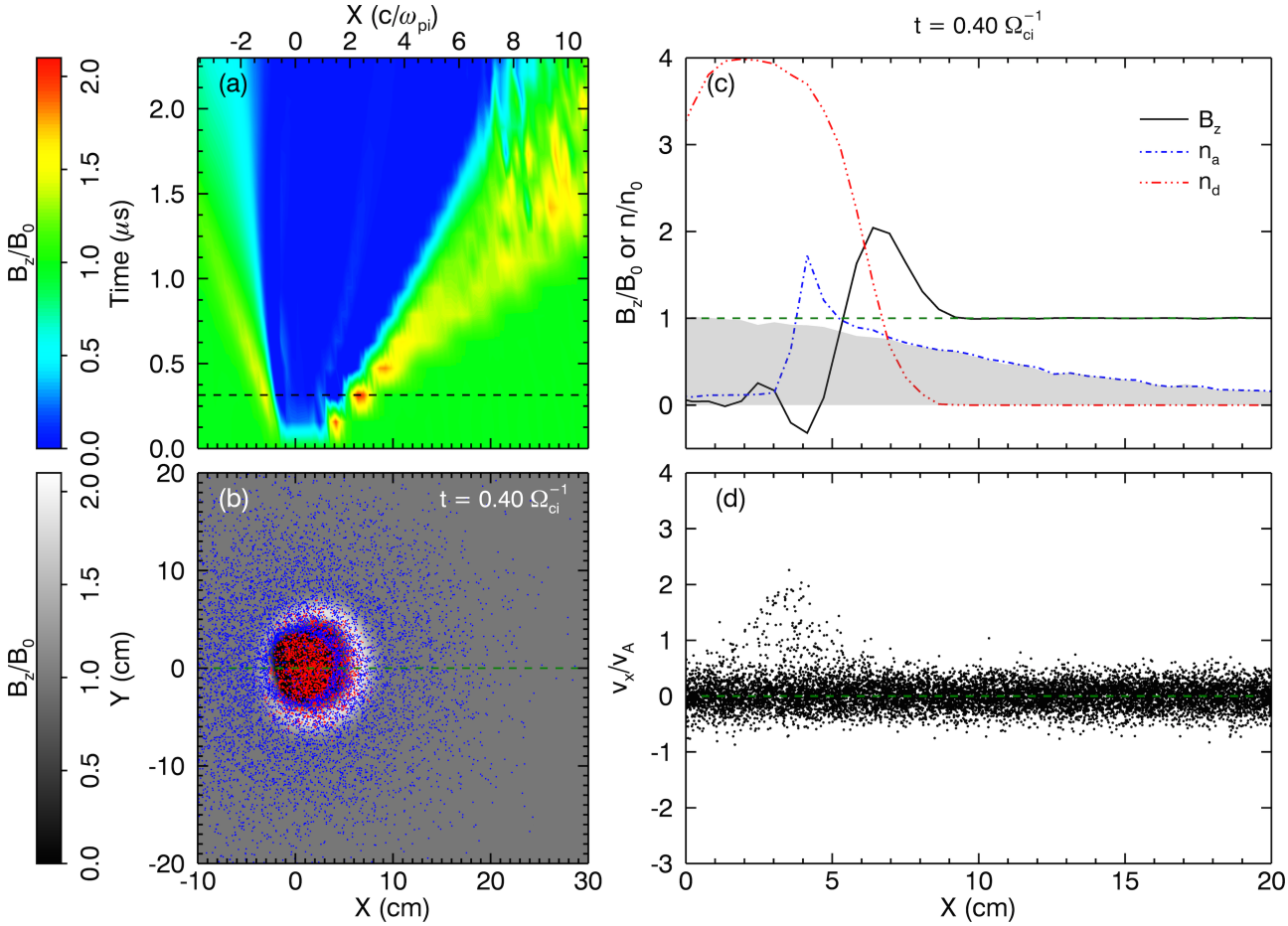

Figure 3.9: 2D hybrid simulation of Run 3 initialized to the same experimental conditions. At initial time, the ambient plasma has a Gaussian distribution centered on the initial debris distribution. The debris cloud (C^{+4}) is concentrated at $(x, y) = (0, 0)$ in a small disk ($\emptyset = 0.5\ c/\omega_{pi}$) with Gaussian intensity. (a) Contour streak plot of B_z. Also shown (dashed) is the time at which (b)-(d) are calculated. (b) Spatial contour plot of B_z at early time (0.4 Ω_{ci}^{-1}) from the same simulation. 1D profiles at $y = 0$ (green dashed) are shown in (c). (c) Magnetic (solid), ambient density (dot-dash), and debris density (dot-dot-dash) profiles at the same time showing the formation of a magnetic compression consistent with the RH jump conditions, but an insufficiently magnetized ambient compression. The original ($t = 0$) ambient density profile is also shown (gray overlay). (d) Phase-space plot of ambient ions (dots) at late time. A lack of reflected ions is consistent with the failure to form a shock.

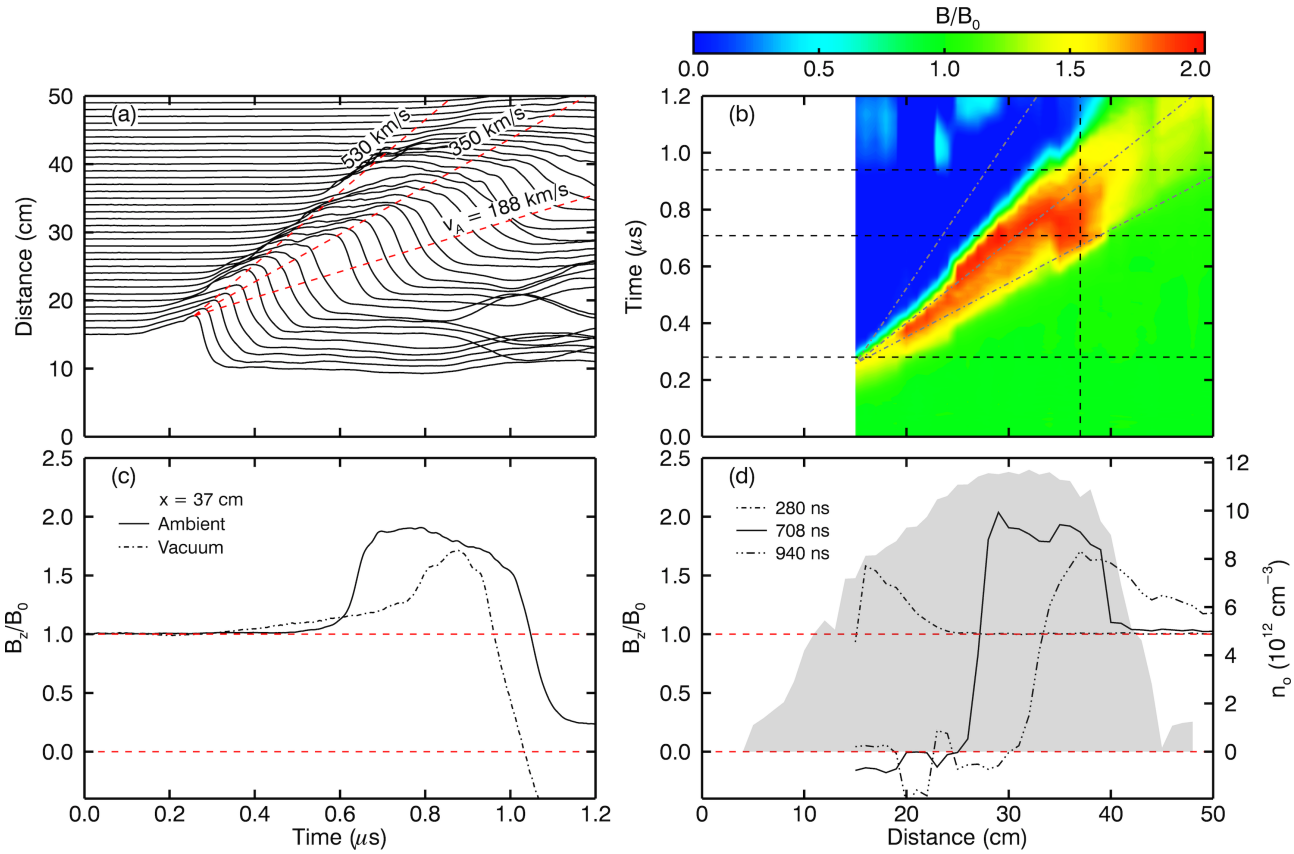

Figure 3.10: Results from shock experiment Run 4 (see Table 3.1). (a) Stacked temporal plots of magnetic field amplitude with velocity lines (dashed). (b) Contour streak plot of normalized magnetic field. Also shown are spatial and temporal lineouts (dashed) and velocity lines (dot-dash). (c) Spatial lineout from (b) containing maximum compression and corresponding vacuum profile. (d) Temporal lineouts from (b), including at maximum compression (solid). The ambient density profile is also shown (gray overlay). The results indicate that a shock formed but did not have sufficiently uniform ambient density to fully separate from the piston.

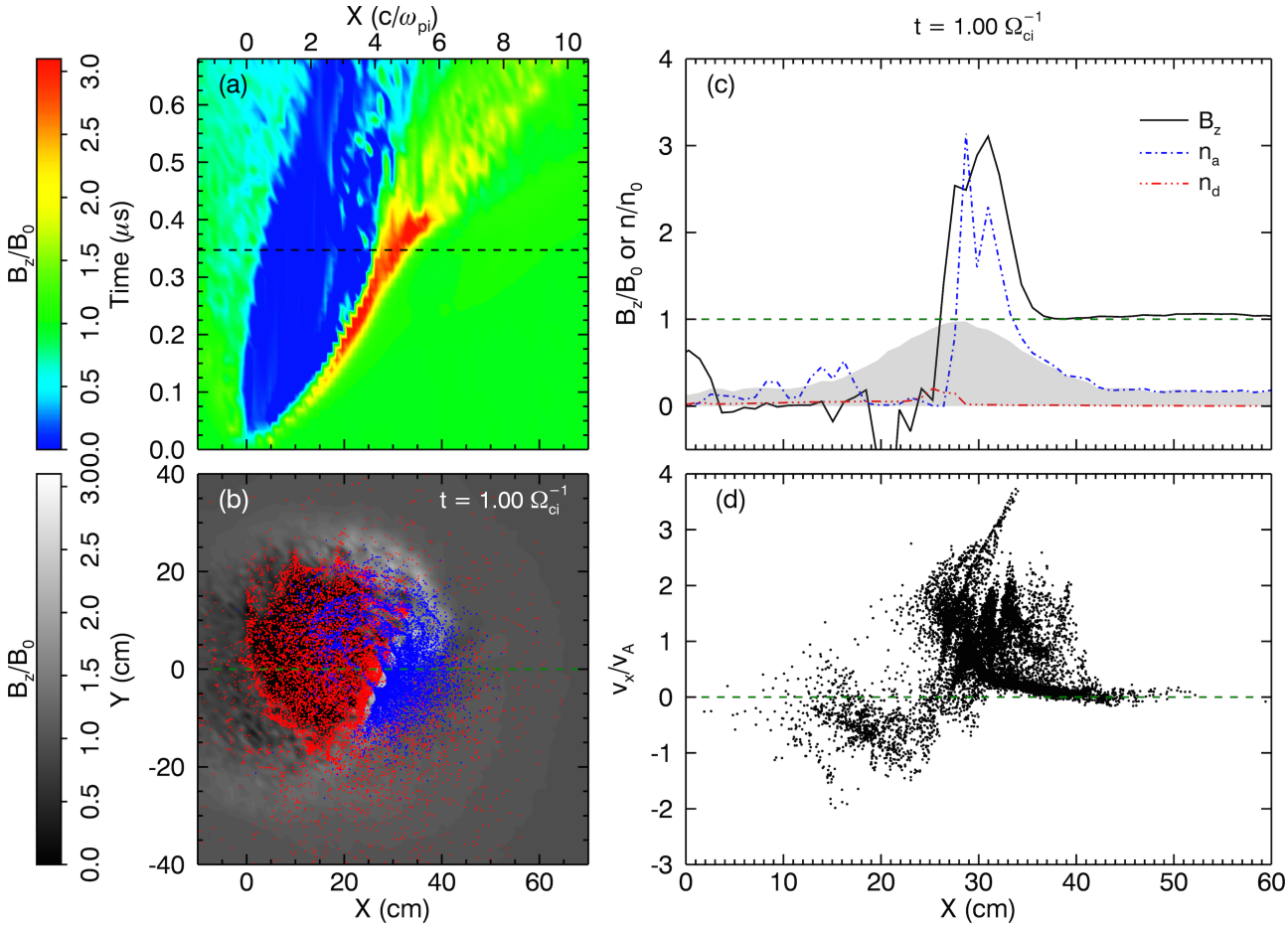

Figure 3.11: 2D hybrid simulation of Run 4 initialized to the same experimental conditions. At initial time, the ambient density is inhomogenous, with a uniform low-density component over the whole domain and a high-density Gaussian core centered at $x = 30$ cm ($4\ c/\omega_{pi}$). The debris cloud (C^{+4}) is concentrated at $(x, y) = (0, 0)$ in a small disk ($\varnothing = 0.25\ c/\omega_{pi}$) with Gaussian intensity. (a) Contour streak plot of B_z. Also shown (dashed) is the time at which (b)-(d) are calculated. (b) Spatial contour plot of B_z at late time ($1\ \Omega_{ci}^{-1}$) from the same simulation. 1D profiles at $y = 0$ (green dashed) are shown in (c). (c) Magnetic (solid), ambient density (dot-dash), and debris density (dot-dot-dash) profiles at late time showing the formation of a low-Mach number shock, with magnetic and density compressions consistent with the RH jump conditions. The original ($t = 0$) ambient density profile is also shown (gray overlay). (d) Phase-space plot of ambient ions (dots) at late time. A small population of reflected ions at $x = 30$ cm is consistent with the formation of a shock.

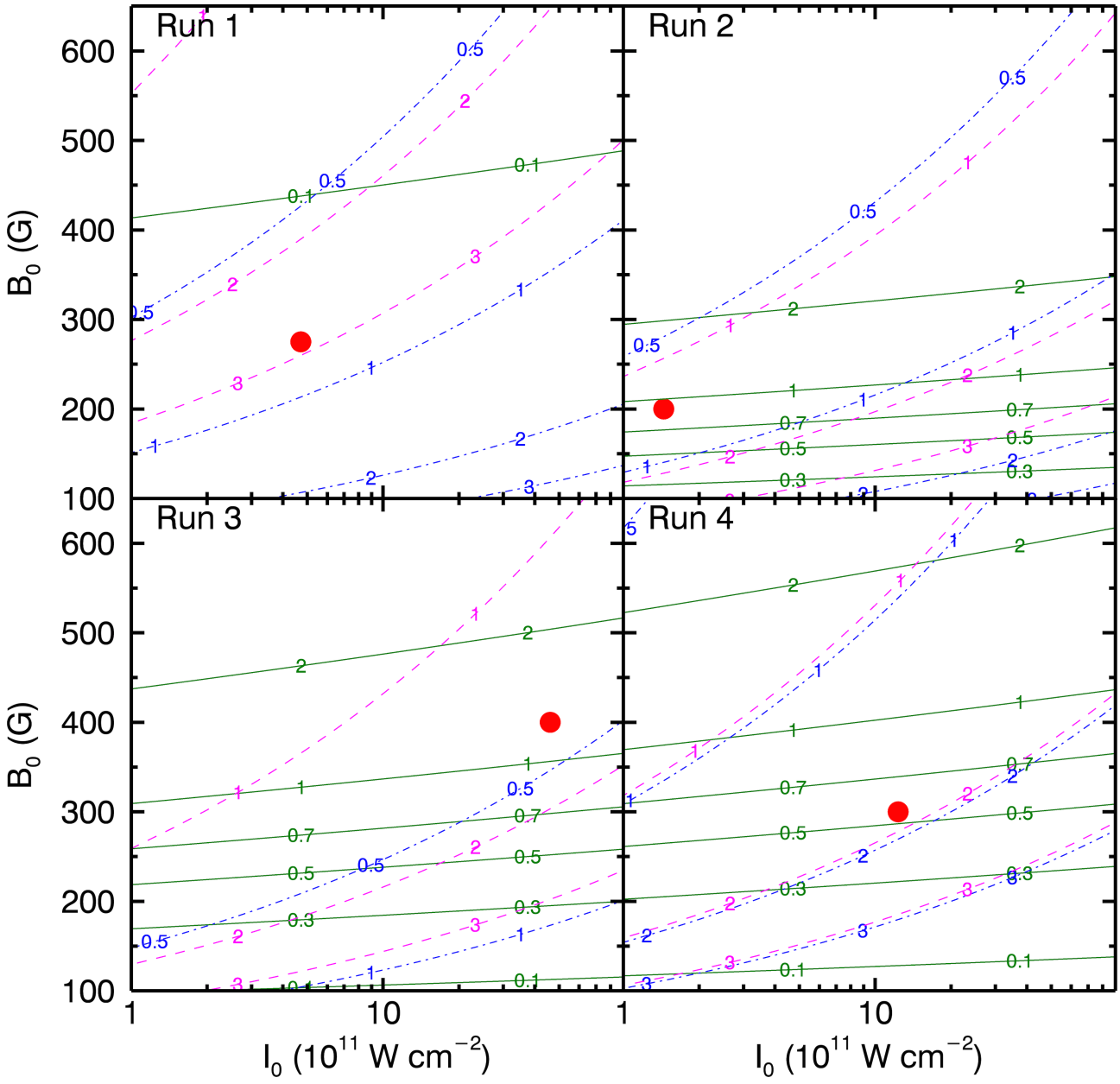

Figure 3.12: Parameter spaces for each experimental run, with ambient density fixed to the experimental value. The location of the experiment with respect to background magnetic field B_0 and incident laser intensity I_0 is represented by the solid circle. Also shown are contours of constant ϵ (solid), constant μ (dot-dash), and constant M_A (dashed).

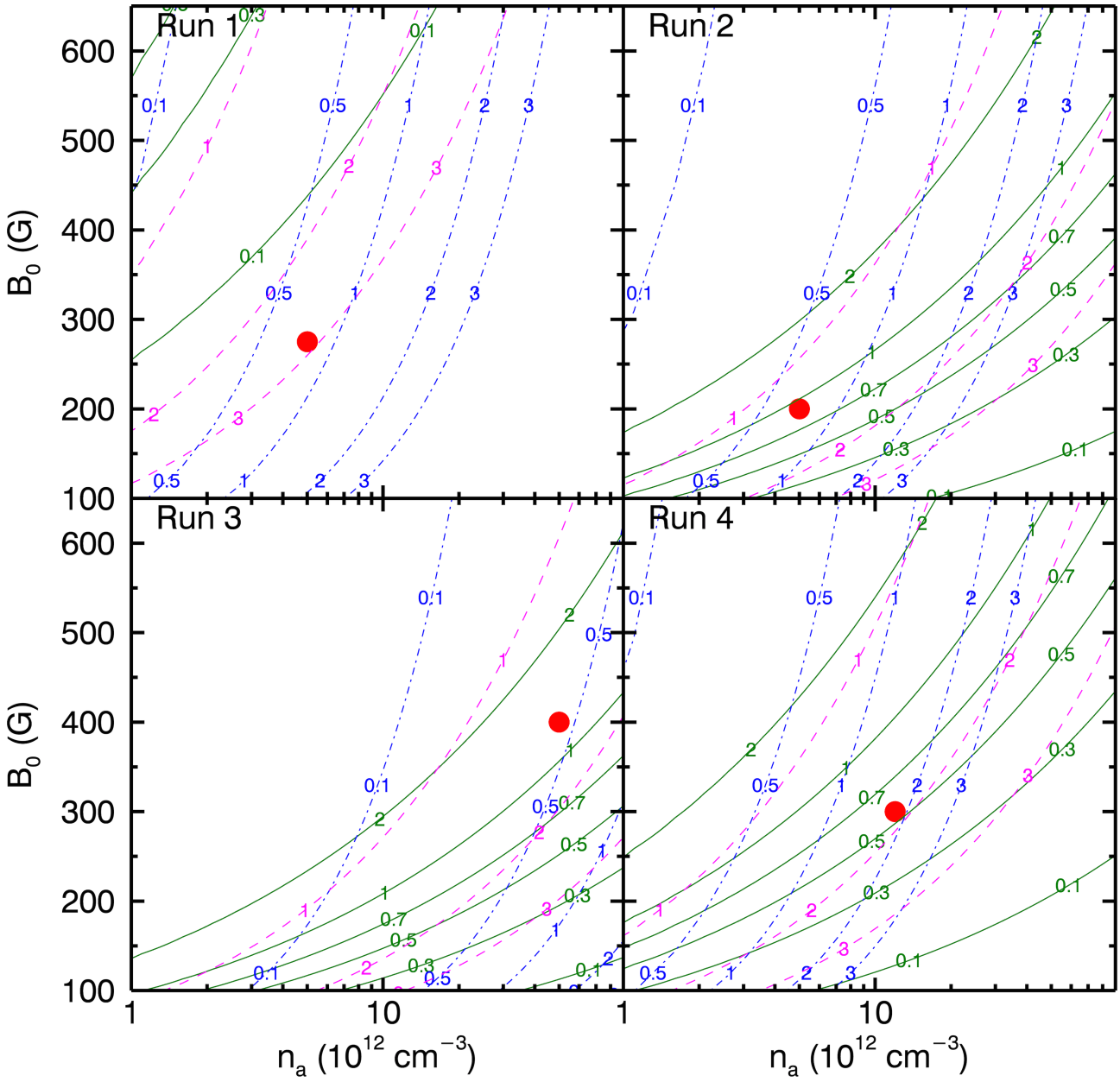

Figure 3.13: Parameter spaces for each experimental run, with laser intensity fixed to the experimental value. The location of the experiment with respect to background magnetic field B_0 and ambient ion density n_a is represented by the solid circle. Also shown are contours of constant ϵ (solid), constant μ (dot-dash), and constant M_A (dashed).

CHAPTER 4

Characterization of Laser-Produced Plasmas

When a high-intensity laser is incident on a solid target, a laser-produced plasma (LPP) is formed. LPPs have been studied in a wide range of contexts, from inertial-confinement fusion [31, 40] to material deposition on semiconductors [76, 1]. When detailed measurements of the ablated plasma have been done, they have generally been at small scales (< 1 cm, < 100 ns) or with higher-mass targets (Al, Au, *etc.*) [29, 80]. A few larger-scale studies were done on LPPs from a carbon target several decades ago [7, 67, 16], but they were limited in the characteristics measured. More recent studies are similarly limited by spectroscopic and photographic measurements [32, 54, 53].

A fluid picture of a LPP, in which parameters vary smoothly and a characteristic value can often be assigned to the expansion speed or charge-state, is often sufficient for generic ablated plasmas, especially at low laser energy. However, in the context of laboratory collisionless shocks and high-energy lasers, the nature of the ablated plasma plays a substantial role in the effectiveness of a magnetic piston, and hence the formation of shocks. It is therefore paramount to understand the complex behavior and composition of the LPP. Specifically, one wants to know the spatial and temporal evolution of the shape, velocity, charge state, temperature, and density of the expanding plasma. It is then possible to estimate the initial state of the LPP, which is used to calculate shock formation criteria in Chapter 3.

In this chapter, experimental data, analytic modeling, and computational simulations provide new measurements of plasma characteristics and new insight into the complex evolution of plasmas generated from a carbon or plastic target. Multiple diagnostics – including Thomson scattering, emission spectroscopy, magnetic flux probes, and fast-gate filtered pho-

Run	Energy (J)	Intensity (W/cm^2)	Distance (cm)	Target	B (G)	Ambient Plasma
Run 1	50	1.2×10^{11}	1.2-2.4	C	0	N/A
Run 2	40	1.5×10^{10}	1.2-2.4	C	0	N/A
Run 3	65	2×10^{10}	1.2-2.4	C	0-1000	N/A
Run 4	100	1.8×10^{11}	2.4-5.6	C	300	He^{+1}
Run 5	10	9.4×10^{10}	5.0	C	0	N/A
Run 6	1	1×10^{11}	0-25	C_2H_4	0-350	N/A

Table 4.1: Summary of LPP characterization runs.

tography – build upon previous work and extend it to larger scales ($\sim$ 10 cm, $\sim$ 1 μs), while 3D fluid modeling and 1D radiation-MHD simulations provide a comprehensive framework for understanding LPPs. Experimental results are presented in Section 4.1. LPP expansion models are detailed in Section 4.2 and simulations are presented in Section 4.3. Significant results are summarized in Section 4.4.

4.1 Experimental Results

To characterize a laser-ablated plasma, experiments were performed on the Phoenix vacuum chamber and Large Plasma Device (see Sections 2.3 and 2.2, respectively). Since the primary diagnostic was Thomson scattering, most of the results presented will be Thomson scattering data, with other datasets included as necessary. An extensive outline on the theory of Thomson scattering can be found in Section 5.1, while details on the extraction of plasma parameters from Thomson scattering data can be found in Section 5.3.4. A summary of the experimental runs is shown in Table 4.1.

Fig. 4.1 is representative of Thomson scattering data and shows streaked contour plots of electron temperature T_e and density n_e from Run 1 in the Phoenix chamber (see Table 4.1). The data was taken from images centered 1.8 cm from the target surface and 200-600 ns after target ablation. An initial hot, dense plasma ($\sim$ 20 eV, $\sim 1.5 \times 10^{17}$ cm^{-3}) can be seen early

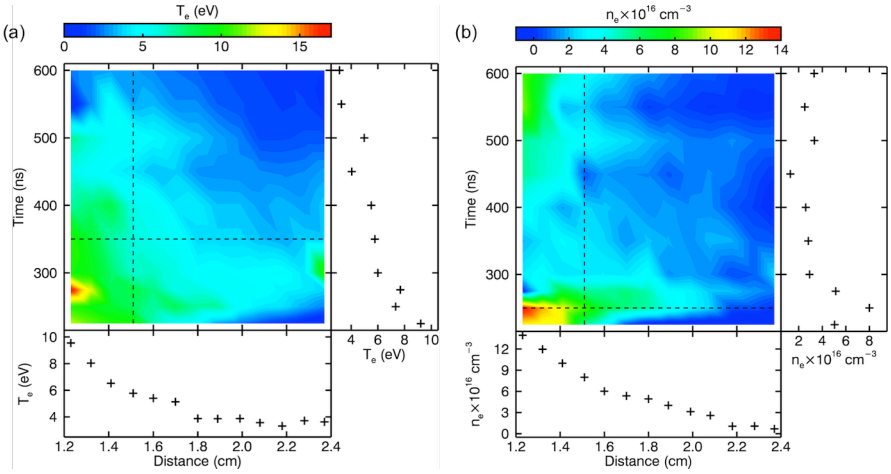

Figure 4.1: Streaked contour plots of (a) T_e and (b) n_e from Thomson scattering data from Run 1 (see Table 4.1). Also shown are representative profiles (dashed) of spatial data at a given time (bottom plot) or temporal data at a given distance (side plot).

in time approximately 1.2 cm from the target, indicating a time-of-flight (TOF) speed of ~ 60 km/s. (In principle, it is possible to extract a plasma velocity from the Doppler-shift of the Thomson scattered spectrum. However, the low spectrometer resolution and calibration uncertainties allowed only relative measurements.) The plasma can then be seen traversing to the back of the imaging volume (2.4 cm from the target) at the same speed, while cooling and diffusing. It is interesting to note a second density peak arriving around 500 ns (~ 30 km/s), with a corresponding increase in temperature. This suggests the arrival of a second plasma "blob", the possible origin of which will be addressed in Section 4.3.

A similar set of plots constructed from Thomson scattering data from the LAPD (Run 4) is shown in Fig. 4.2b-c. Also shown is a mosaic of images a different times (Fig. 4.2a), showing the arrival of the LPP and subsequent evolution. The images were taken with a fiber collection probe (see Section 5.3.2), accounting for the regularly spaced dark streaks. The data was taken from images of a plasma expanding into a 300 G external field and ambient He plasma, centered 4.0 cm from the target surface and 250-1000 ns after target ablation. It is worth noting that the directed ion gyroradius ($r_{gi} = v/\omega_{ci} > 6$ cm), even under favorable conditions, is larger than the collection region, implying that the external

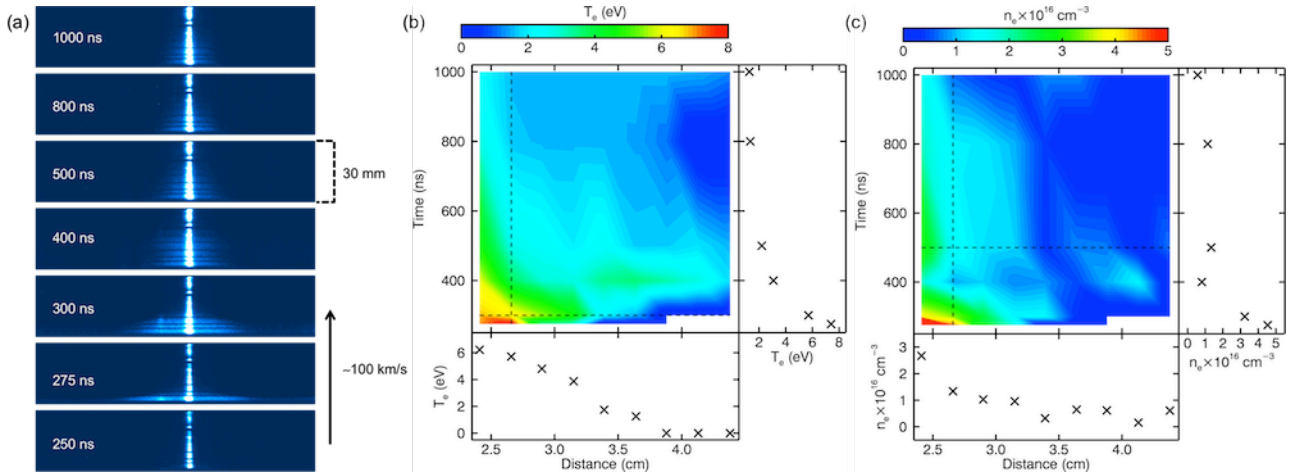

Figure 4.2: (a) Time series of spatially-resolved images from a fiber collection probe and corresponding streaked contour plots of (b) T_e and (c) n_e from Thomson scattering data from Run 4 (see Table 4.1). Also shown are representative profiles (dashed) of spatial data at a given time (bottom plot) or temporal data at a given distance (side plot) for (b) and (c).

magnetic field and ambient plasma should have little effect on the LPP at these times and distances. Like Run 1 a hot, dense plasma is initially seen, with a temperature ($\sim$ 8 eV) and density ($\sim 1.0 \times 10^{17}$ cm^{-3}) comparable to the plasma in Run 1. A bump in density at 500 ns ($\sim$ 50 km/s) also suggests a second plasma "blob". Assuming a constant speed, the TOF speed of the initial plasma edge at 250 ns is $\sim$ 100 km/s.

Fast-gate images provide further insight into the structure and evolution of the LPP (see Run 6 in Table 4.1). Images were taken with a gate width of 3 ns every 1 ns for 100 ns after laser ablation, and every 10 ns, up to 2.5 μs after ablation, thereafter. Each image represents a different laser shot. This sequence was repeated with various carbon line filters (CI-CV) inserted between the imaging volume and the camera. In Fig. 4.3, images of the LPP at various times are shown (no filter was used). Also shown are leading edge contours. In addition to an expanding plasma edge, a relatively stationary core region near the plasma can be seen, along with a slow moving ($\lesssim$ 10 km/s) ejection near the target's surface that probably corresponds to neutral and molecular carbon. In Fig. 4.4, the leading edge is further

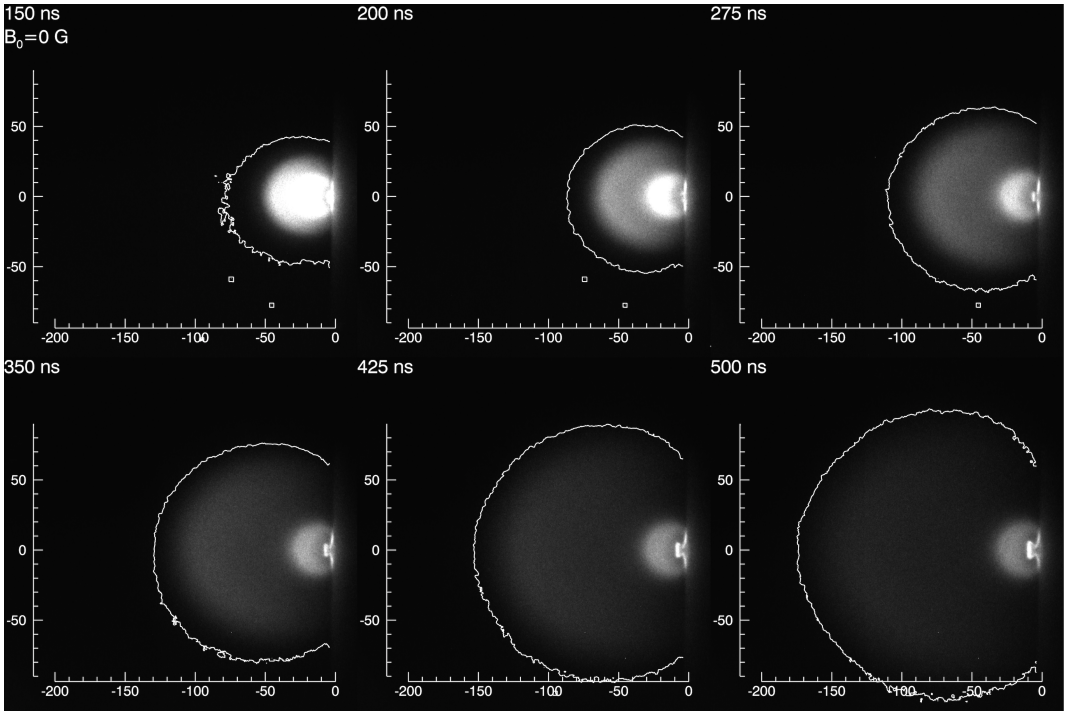

Figure 4.3: Fast-gate images of a LPP at various times. Each image represents a different laser shot. No emission line filters were used, and there was no external magnetic field. A leading edge contour is shown (solid), along with reference axes in mm (the laser was incident at (x,y)=(0,0)). All images are scaled to the same intensity range. Three distinct regions can be seen: the leading plasma plume, a stationary core, and a slowly expanding ejection near the target's surface.

analyzed. For each image, an edge position along the blowoff and at greatest extent parallel to the target surface were calculated. It can be seen that the edge component perpendicular to the target surface reaches a free streaming state with a constant velocity of 288 km/s by at least $\sim$ 100 ns. Likewise, the edge parallel to the target surface is streaming at 165 km/s. Earlier in time ($<$ 100 ns), a numerical differentiation of the edge's evolution indicates an acceleration on the order of 10-100 km/s/ns in both directions. However, this is inconclusive given the difficulty in finding a true edge at the earliest times (where acceleration is most likely to occur), since intense laser light causes signal saturation near the target. With regards to both size and speed, similar results are seen when the images are filtered for

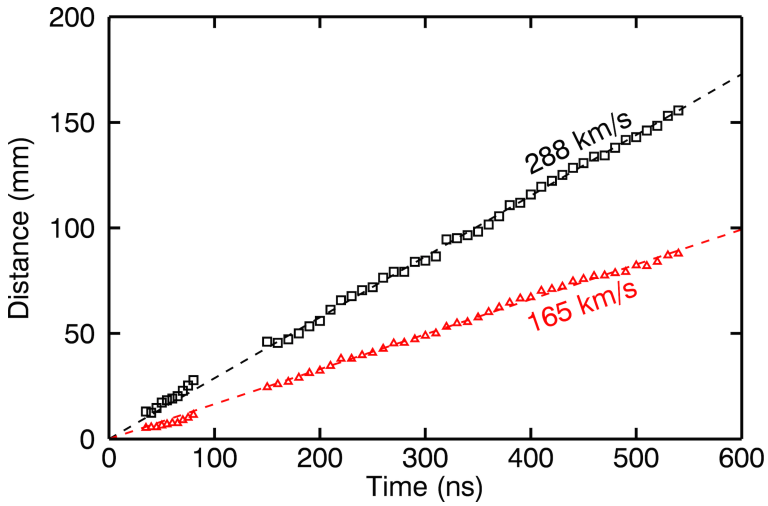

Figure 4.4: Plot of edge position perpendicular (squares) and parallel (triangles) to the target surface. For $t > 100$ ns, a corresponding speed was calculated (dashed). The consistency of the speeds indicate a free streaming state in both directions.

various carbon emission lines.

In addition to temperature and density characterization, information on the LPP charge states was taken with emission spectroscopy. Data was taken 5 cm from the target surface, 200-250 ns after ablation, for CII (C^{+0}) to CV (C^{+4}) ion lines. For each line, a Doppler shift and width were computed, as shown in Fig. 4.5. A distinct separation of velocity distribution by ion species is seen, with higher charge states corresponding to faster velocities. This suggests that the debris ions are ablated in charge state "shells" and is investigated in Section 4.3.

Lastly, magnetic flux ("bdot") probe measurements of the LPP indicate that a tenuous population of fast ions is primarily responsible for interacting with external elements (*e.g.* magnetic field). As can be seen in Fig. 4.6, when an LPP is ablated into an external magnetic field, a diamagnetic cavity is formed, with a leading edge moving at 400 km/s. Since this is faster than any of the plasma speeds observed by Thomson scattering or spectroscopy, it suggests that the fast population is lower-density by at least a factor of 100, based on the sensitivity of the Thomson diagnostic (no scattered signal was detected at times correspond-

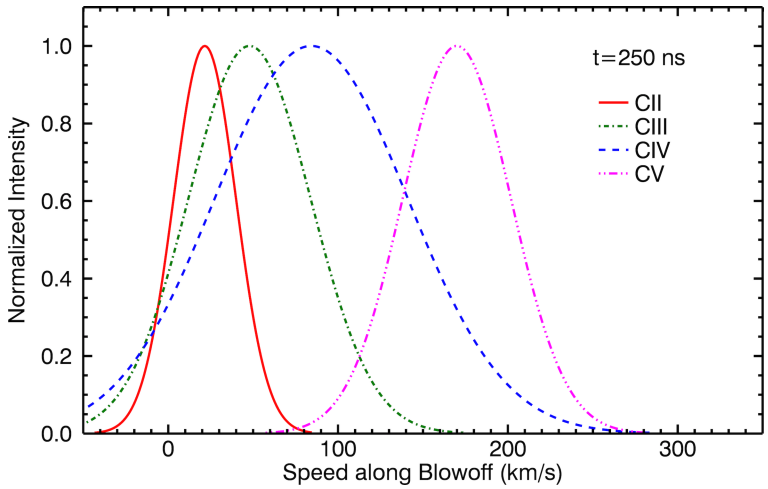

Figure 4.5: Velocity distributions derived from Doppler spectroscopic measurements of CII-CV, 250 ns after ablation.

ing to this speed). It also suggests that these ions have a high charge state based on Fig. 4.5. This is explored in Section 4.3.

4.2 LPP Expansion Models

In order to place the experimental data in context, several analytic models were developed to provide a comprehensive framework for understanding the behavior of expanding LPPs. All the models approximate the plasma as an unmagnetized, adiabatic fluid, the validity of which is addressed in Section 4.2.1. Note that the goal is not to model the expansion at all times, but only long enough to establish the basic characteristics of the LPP. After detailing the models (Section 4.2.3) they are compared in Section 4.2.4 to the experimental data from Section 4.1.

4.2.1 Assumptions

All the models developed here approximate the expanding plasma as an ideal gas subject to the fluid equations. For tractability, the gas is treated as a neutral fluid, so an external magnetic field is irrelevant. Two-component (ion and electron) plasmas are simulated in

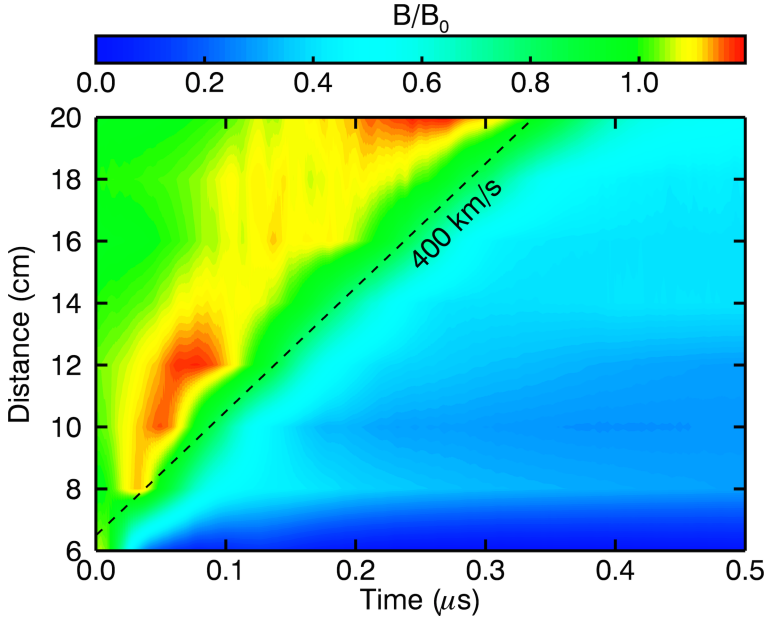

Figure 4.6: Streaked contour plot of magnetic field in vacuum with $B_0 = 390$ G. The formation of a diamagnetic cavity expanding at 400 km/s is clearly visible. Data was taken with a bdot probe at the Trident laser facility (see Section 2.1) with an incident laser intensity $I_0 = 10^{11}$ W cm^{-2}.

Section 4.3. Nonetheless, the assumption of zero magnetic field is often justified given that the region of interest for characterizing LPPs is usually smaller than the ion gyroradius, *i.e.* the ions are largely unmagnetized.

The models further assume the expanding plasma is adiabatic with an adiabatic index γ ($\gamma = 5/3$ for a monotonic gas) and subject to the ideal gas equation of state $P \propto nT$, where P is pressure, n is density, and T is temperature. If the plasma is reversibly adiabatic (isentropic), then it follows that $P^{\gamma-1}T^{-\gamma} =$ constant and $T \propto n^{\gamma-1}$. If the plasma is irreversibly adiabatic (free expansion), then the plasma temperature is isothermal. Assuming a constant expansion speed (see Section 4.2.3), the position of the plasma can be written $r \propto t$, and hence $n \propto t^{-3}$ (t is time). For an adiabatically expanding monotonic gas, then, $T \propto t^{-2}$.

In addition to pure adiabatic expansion, the density can decay due to radiative and

collisional recombination [67]. The corresponding rates are given by

$$R_R = \left(\frac{dn_e}{dt}\right)_R = -2.7 \times 10^{-19}\, Z^2\, T_e^{-3/4}\, n_e\, n_i \propto t^{-4.5} \tag{4.1}$$

$$R_C = \left(\frac{dn_e}{dt}\right)_C = -9.2 \times 10^{-39} Z^3\, \ln\sqrt{Z^2+1}\, T_e^{-9/2}\, n_e^2\, n_i \propto t^0 \tag{4.2}$$

$$R_E = \left(\frac{dn_e}{dt}\right)_E \propto t^{-4} \tag{4.3}$$

where R_R, R_C, and R_E are the radiative recombination, collisional recombination, and expansion rates, respectively, and the last proportionality assumes an adiabatic expansion. Note that $R_C > R_R$ when $n_e \gtrsim 3 \times 10^{13} T^{3.75} Z^{-1}$, which is usually the case for the plasmas studied here. It can thus be seen that for an adiabatic expansion, eventually collisional recombination will dominate. It can also be shown [47] that for a recombination-dominated plasma, the heat liberated by electron-electron collisions will heat the plasma and change the temperature scaling to $T \propto t^{-1}$.

The assumption of fluid behavior is valid as long as the ion and electron populations remain mostly Maxwellian and respond together (*i.e.* low-frequency). At early times this is easily satisfied due to the very high ablation densities and local-thermodynamic-equilibrium (LTE) conditions. At later times, the assumption's validity depends on which process, collisions or expansion, is dominant, and hence on how quickly T and n decay. The collision rate ν for electrons or ions generally has the form $\nu = T^{-3/2} n \ln\lambda$, where $\ln\lambda$ is the Coulomb logarithm and is mostly constant. If the collision rate remains close to its initial value during the LTE phase, each species will remain thermalized (*i.e.* Maxwellian).

Thus, for a purely adiabatic expansion where $T \propto t^{-2}$ and $n \propto t^{-3}$, ν will remain nearly constant and the populations will remain Maxwellian indefinitely. If instead $T \propto t^{-1}$ and $n \propto t^{-3}$, as in a recombination-dominated plasma, $\nu \to 0$ and eventually the species will become collisionless. It is worth noting, though, that in this case the electron-ion collision rate will tend to zero first, meaning each species individually may remain fluid-like for some time even though they no longer constitute a neutral fluid. In most cases, then, it

is reasonable to assume fluid-like behavior at the early expansion times of interest.

4.2.2 Laser-Target Interaction and Scalings Laws

The interaction of a high-intensity laser with a solid target is a complex system. The characteristics of the resulting ablated plasma will depend on the properties of the laser (energy, intensity, wavelength), the target (composition, thermal and emission properties, *etc.*), and the timescales of interaction. While the details of these interactions are beyond the scope of this dissertation, a general outline of the process is given in Section 1.1, and additional details can be found in [40, 50, 76].

More relevant are models that describe the rate at which mass is ablated from a planar target and the resulting expansion velocity of the LPP. Specifics on the derivation of these models can be found in [40, 50]. The results fall into two regimes based on the dominant mechanism of laser absorption. The first regime is valid when

$$\frac{\rho_s}{\rho_c} = 0.17 \left(\frac{\lambda}{1\mu\text{m}}\right)^{\frac{4}{3}} \left(\frac{I_a}{10^{13}\text{W cm}^{-2}}\right)^{\frac{1}{3}} \left(\frac{Z\,L}{100\mu\text{m}}\right)^{-\frac{1}{3}} < 1 \tag{4.4}$$

and describes low irradiance laser interactions, where inverse bremsstrahlung is dominantly responsible for absorbing laser power. Here, ρ_s and ρ_c are the sonic and critical mass densities, respectively, λ is the laser wavelength, I_a is the absorbed laser irradiance, Z is the charge state, and L is a characteristic length scale on the order of the laser spot radius. The resulting mass ablation rate $\dot{m}$ and expansion velocity v are given by

$$\begin{aligned} \dot{m} &= 0.53 \times 10^5 \left(\frac{\lambda}{1\mu\text{m}}\right)^{-\frac{4}{9}} \left(\frac{I_a}{10^{13}\text{W cm}^{-2}}\right)^{\frac{5}{9}} \left(\frac{Z\,L}{100\mu\text{m}}\right)^{-\frac{2}{9}} \left[\frac{\text{g}}{\text{cm}^2\text{s}}\right] \\ v &= 3.6 \times 10^2 \left(\frac{\lambda}{1\mu\text{m}}\right)^{\frac{2}{9}} \left(\frac{I_a}{10^{13}\text{W cm}^{-2}}\right)^{\frac{2}{9}} \left(\frac{Z\,L}{100\mu\text{m}}\right)^{\frac{1}{9}} \left[\frac{\text{km}}{\text{s}}\right] \end{aligned} \tag{4.5}$$

The second regime is valid when

$$\frac{\rho_s}{\rho_c} = 0.3 \left(\frac{\lambda}{1\mu\text{m}}\right)^2 \left(\frac{I_a}{10^{13}\text{W cm}^{-2}}\right)^{\frac{4}{7}} \left(\frac{Z\,L}{100\mu\text{m}}\right)^{-\frac{3}{7}} > 1 \tag{4.6}$$

and describes high irradiance laser interactions, where absorption at the critical density is dominant. The resulting mass ablation rate and expansion velocity are then given by

$$\begin{aligned} \dot{m} &= 0.34 \times 10^5 \left(\frac{I_a}{10^{13}\text{W cm}^{-2}}\right)^{\frac{5}{7}} \left(\frac{Z\,L}{100\mu\text{m}}\right)^{-\frac{2}{7}} \left[\frac{\text{g}}{\text{cm}^2\text{s}}\right] \\ v &= 6.5 \times 10^2 \left(\frac{I_a}{10^{13}\text{W cm}^{-2}}\right)^{\frac{1}{7}} \left(\frac{Z\,L}{100\mu\text{m}}\right)^{\frac{1}{7}} \left[\frac{\text{km}}{\text{s}}\right] \end{aligned} \tag{4.7}$$

For typical laser parameters used in this work, Eq. 4.4 is easily satisfied, the low irradiance regime is dominant, and Eq. 4.5 can provide an estimate for the total mass ablated and the expansion velocity. Indeed, experimental studies by Meyer and Thiell [50] and Grun *et al.* [31] at similar laser parameters show agreement with the scalings in Eq. 4.5. Meyer and Thiell, though, find that the wavelength dependence is slightly modified to be $\lambda^{-4/3}$ for $\dot{m}$ and $\lambda^{2/3}$ for v.

Using Eq. 4.5 with the above modifications, the total number of ablated particles N_B can be calculated by integrating over $\dot{m}$ for a spatially uniform, temporal Gaussian intensity distribution with peak incident intensity I_0. The incident I_0 and absorbed I_a intensities are taken to be the same, which is a modest approximation given that the absorbed intensity is generally a significant fraction ($> 50\%$) of the incident intensity [40]. The result is

$$\begin{aligned} N_B &= 3.53 \times 10^{15} \left(\frac{I_0}{10^{13}\text{W cm}^{-2}}\right)^{\frac{5}{9}} \left(\frac{\lambda}{1\mu\text{m}}\right)^{-\frac{4}{3}} \left(\frac{L}{100\mu\text{m}}\right)^{\frac{16}{9}} \left(\frac{\Delta t_L}{1\text{ns}}\right) \left(\frac{Z^{-\frac{2}{9}}}{A}\right) \\ &= 4.04 \times 10^{15} \left(\frac{E_0}{1\text{J}}\right)^{\frac{5}{9}} \left(\frac{\lambda}{1\mu\text{m}}\right)^{-\frac{4}{3}} \left(\frac{L}{100\mu\text{m}}\right)^{\frac{6}{9}} \left(\frac{\Delta t_L}{1\text{ns}}\right)^{\frac{4}{9}} \left(\frac{Z^{-\frac{2}{9}}}{A}\right) \end{aligned} \tag{4.8}$$

where E_0 is the incident laser energy, Δt_L is the pulse width, L is the laser spot diameter, and A is the atomic number. For $\lambda = 1.053\,\mu$m, $L = 1$ mm, $\Delta t_L = 25$ ns, $Z = 3$, $A = 12$, and $I_0 = 10^{11}$ W cm^{-2}, $N_B = 2.5 \times 10^{16}$.

4.2.3 Fluid Models

While the LPP is obviously not well approximated by fluid models at small scales, the large scale, smooth behavior can be reasonably expected to be fluid-like. The fluid equations are derived from the continuity (conservation of mass) equation

$$\frac{\partial \rho}{\partial t} + \nabla \cdot (\rho \vec{v}) = \frac{\partial \rho}{\partial t} + (\vec{v} \cdot \nabla \rho) + \rho (\nabla \cdot \vec{v}) = 0 \tag{4.9}$$

where ρ is the mass density and $\vec{v}$ is the fluid velocity, and from the equation of motion (conservation of momentum)

$$\frac{\partial}{\partial t}(\rho \vec{v}) + \nabla \cdot (\rho \vec{v} \vec{v}) = \vec{v}\frac{\partial \rho}{\partial t} + \rho \frac{\partial \vec{v}}{\partial t} + \vec{v}(\vec{v} \cdot \nabla \rho) + \rho (\vec{v} \cdot \nabla)\vec{v} + \vec{v}\rho (\nabla \cdot \vec{v}) = -\nabla P \tag{4.10}$$

where P is the pressure tensor and other source terms have been ignored. Using Eq. 4.9, Eq. 4.10 can be rewritten

$$\begin{aligned} \vec{v} \underbrace{\left(\frac{\partial \rho}{\partial t} + \vec{v} \cdot \nabla \rho + \rho (\nabla \cdot \vec{v}) \right)}_{0} + \rho \left(\frac{\partial \vec{v}}{\partial t} + (\vec{v} \cdot \nabla)\vec{v} \right) &= -\nabla P \\ \Rightarrow \rho \left(\frac{\partial \vec{v}}{\partial t} + (\vec{v} \cdot \nabla)\vec{v} \right) = \rho \frac{D\vec{v}}{Dt} &= -\nabla P \end{aligned} \tag{4.11}$$

To proceed, let

$$\vec{v} = \frac{x}{X(t)}\frac{dX}{dt} + \frac{y}{Y(t)}\frac{dY}{dt} + \frac{z}{Z(t)}\frac{dZ}{dt} \tag{4.12}$$

where $\{x, y, z\}$ are cartesian positions and $\{X, Y, Z\}$ are corresponding time-dependent characteristic length scales [1, 76]. From Eq. 4.12 it can be seen that each direction decouples from the others. Taking, for example, the $\hat{x}$ direction and using Newtonian dot notation, Eq. 4.10 becomes

$$\rho\left[\left(\frac{x\ddot{X}}{X}-\frac{x\dot{X}^2}{X^2}\right)+\left(\frac{x\dot{X}}{X}\partial_x\left(\frac{x\dot{X}}{X}\right)\right)\right]=-\partial_x P$$
$$\Rightarrow \frac{x\ddot{X}}{X}=-\partial_x P \tag{4.13}$$

Two models of the equation of state of the LPP that satisfy Eq. 4.13 (and related equations for $\hat{y}$ and $\hat{z}$) will be considered (other models can be found in [75, 37, 38]). The first was originally devised by Singh and Narayan [76]. In this model, two regimes are distinguished: during ($t < t_L$) and after ($t \geq t_L$) the laser pulse. During the laser pulse, the temperature is constant at T_0 while the density is Gaussian and the number of ablated particles N is linearly augmented with time. After the laser, the temperature is taken as isothermal but potentially time-dependent, while the density remains Gaussian but N is constant. The density is given as

$$n(x,y,z,t)=n_0(t)\exp\left(\frac{-x^2}{2X(t)^2}+\frac{-y^2}{2Y(t)^2}+\frac{-z^2}{2Z(t)^2}\right)$$
$$n_0(t)=\begin{cases}\sqrt{\frac{8}{\pi^3}}\frac{N_0}{X(t)Y(t)Z(t)}\frac{t}{t_L} & \text{for} \quad t<t_L\\ \sqrt{\frac{8}{\pi^3}}\frac{N_0}{X(t)Y(t)Z(t)} & \text{for} \quad t\geq t_L\end{cases} \tag{4.14}$$
$$N(t)=\iiint n(x,y,z,t)dxdydz=\begin{cases}N_0\frac{t}{t_l} & \text{for} \quad t<t_L\\ N_0 & \text{for} \quad t\geq t_L\end{cases}$$

The characteristic scale lengths $\{X, Y, Z\}$ are then the $1/e$ edge of the plasma. The temperature is given by

$$T(x,y,z,t)=\begin{cases}T_0 & \text{for} \quad t<t_L\\ T_0\left[\frac{X_0Y_0Z_0}{X(t)Y(t)Z(t)}\right]^{\gamma-1} & \text{for} \quad t\geq t_L\end{cases} \tag{4.15}$$

where $X_0 = X(0)$, $Y_0 = Y(0)$, $Z_0 = Z(0)$. Note that without loss of generality, the time is taken to be zero at the beginning of each regime. The pressure is then given by

$$P(x,y,z,t) = P_0(t)\exp\left(\frac{-x^2}{2X(t)^2}+\frac{-y^2}{2Y(t)^2}+\frac{-z^2}{2Z(t)^2}\right)$$

$$P_0(t) = \begin{cases} \sqrt{\frac{8}{\pi^3}}\frac{N_0 k_B T}{X(t)Y(t)Z(t)}\frac{t}{t_L} & \text{for} \quad t < t_L \\ \sqrt{\frac{8}{\pi^3}}\frac{N_0 k_B T}{X(t)Y(t)Z(t)} & \text{for} \quad t \geq t_L \end{cases} \tag{4.16}$$

Substituting Eq. 4.16 into Eq. 4.13, the equations of motion for $t \geq t_L$ are

$$X(t)\left[\frac{d^2X}{dt^2}\right] = Y(t)\left[\frac{d^2Y}{dt^2}\right] = Z(t)\left[\frac{d^2Z}{dt^2}\right] = \frac{E_1}{M}\left[\frac{X_0Y_0Z_0}{X(t)Y(t)Z(t)}\right]^{\gamma-1} \tag{4.17}$$

where $E_1 = k_B T_0 N_0$, $M = N_0 m$, and m is the mass of one particle. For $t < t_L$, the continuity equation must be modified to allow for the injection of particles. It can be shown that the resulting equation of motion is

$$X(t)\left[\frac{1}{t}\frac{dX}{dt}+\frac{d^2X}{dt^2}\right] = Y(t)\left[\frac{1}{t}\frac{dY}{dt}+\frac{d^2Y}{dt^2}\right] = Z(t)\left[\frac{1}{t}\frac{dZ}{dt}+\frac{d^2Z}{dt^2}\right] = \frac{E_1}{M} \tag{4.18}$$

Since an isothermal temperature is difficult to justify physically, a second model originally proposed by Anisimov *et al.* was also examined [1]. In this model (only for $t > t_L$), the density and pressure are constant on the ellipsoidal surfaces $x^2/X^2 + y^2/Y^2 + z^2/Z^2 = \text{const}$ and the temperature varies as $T \propto n^{\gamma-1}$ (here, $\{X, Y, Z\}$ represent the leading edge of the plasma). For the velocity given by Eq. 4.12 and a non-isothermal temperature, these density and pressure profiles are the only possible solutions to Eq. 4.13. The sharp boundary is a consequence of entropy conservation, which ensures that as the density goes to zero, so does the temperature. The density is given by

$$
\begin{aligned}
n(x,y,z,t) &= n_0(t)\left[1-\frac{x^2}{X(t)^2}-\frac{y^2}{Y(t)^2}-\frac{z^2}{Z(t)^2}\right]^{\frac{1}{\gamma-1}} \\
n_0(t) &= \frac{1}{I_1(\gamma)}\frac{N_0}{X(t)Y(t)Z(t)} \\
I_1(\gamma) &= \pi\frac{\Gamma\left(\frac{\gamma}{\gamma-1}\right)\Gamma(3/2)}{\Gamma\left(\frac{\gamma}{\gamma-1}+3/2\right)}
\end{aligned}
\tag{4.19}
$$

where Γ is the Gamma function. The temperature is given by

$$
T(x,y,z,t) = T_0\left[\frac{X_0Y_0Z_0}{X(t)Y(t)Z(t)}\right]^{\gamma-1}\left[1-\frac{x^2}{X(t)^2}-\frac{y^2}{Y(t)^2}-\frac{z^2}{Z(t)^2}\right] \tag{4.20}
$$

and the pressure is then given by

$$
\begin{aligned}
P(x,y,z,t) &= P_0(t)\left[1-\frac{x^2}{X(t)^2}-\frac{y^2}{Y(t)^2}-\frac{z^2}{Z(t)^2}\right]^{\frac{\gamma}{\gamma-1}} \\
P_0(t) &= \frac{1}{I_2(\gamma)}\frac{E_a}{X(t)Y(t)Z(t)}\left[\frac{X_0Y_0Z_0}{X(t)Y(t)Z(t)}\right]^{\gamma-1} \\
I_2(\gamma) &= \frac{\pi}{\gamma-1}\frac{\Gamma\left(\frac{\gamma}{\gamma-1}+1\right)\Gamma(3/2)}{\Gamma\left(\frac{\gamma}{\gamma-1}+5/2\right)} \\
E_a &= \frac{1}{\gamma-1}\iiint P(x,y,z,0)dxdydz
\end{aligned}
\tag{4.21}
$$

Substituting Eq. 4.21 into Eq. 4.13, the equations of motion become

$$
X(t)\left[\frac{d^2X}{dt^2}\right] = Y(t)\left[\frac{d^2Y}{dt^2}\right] = Z(t)\left[\frac{d^2Z}{dt^2}\right] = \frac{E_2}{M}\left[\frac{X_0Y_0Z_0}{X(t)Y(t)Z(t)}\right]^{\gamma-1} \tag{4.22}
$$

where $E_2 = (5\gamma-3)E_a$.

Using the dimensionless variables

$$
\begin{aligned}
\tau = \tfrac{t}{t_0} \quad & t_0 = \tfrac{R_0}{\sqrt{\beta(\gamma)}} \quad \beta(\gamma) = \tfrac{E}{M} \\
\chi(\tau) = \tfrac{X(t)}{R_0} \quad & \psi(\tau) = \tfrac{Y(t)}{R_0} \quad \zeta(\tau) = \tfrac{Z(t)}{R_0} \\
\kappa = \tfrac{X_0}{R_0} \quad & \lambda = \tfrac{Y_0}{R_0} \quad \mu = \tfrac{Z_0}{R_0}
\end{aligned}
\tag{4.23}
$$

where R_0 is a reference length, Eqs. 4.17 and 4.22 can both be rewritten as

$$\begin{aligned} \chi(\tau)\left[\frac{1}{\tau}\frac{d\chi}{d\tau}+\frac{d^2\chi}{d\tau^2}\right] = \psi(\tau)\left[\frac{1}{\tau}\frac{d\psi}{d\tau}+\frac{d^2\psi}{d\tau^2}\right] = \zeta(\tau)\left[\frac{1}{\tau}\frac{d\zeta}{d\tau}+\frac{d^2\zeta}{d\tau^2}\right] = 1 \quad \text{for} \quad t < t_L \\ \chi(\tau)\frac{d^2\chi}{d\tau^2} = \psi(\tau)\frac{d^2\psi}{d\tau^2} = \zeta(\tau)\frac{d^2\zeta}{d\tau^2} = \left[\frac{\kappa\,\lambda\,\mu}{\chi(\tau)\psi(\tau)\zeta(\tau)}\right]^{\gamma-1} \quad \text{for} \quad t \geq t_L \end{aligned} \tag{4.24}$$

Note that the difference between the two models is contained in τ through its dependence on the model energy in β. Also note that by setting $R_0 = X(0) = Y(0)$, $\kappa = \lambda \to 1$ and Eq. 4.24 is controlled by just two parameters, μ and γ. Eq. 4.24 can be solved by rewriting it as a set of six coupled ordinary differential equations (ODEs)

$t < t_L$	$t \geq t_L$
$\dot{\chi} = \phi$	$\dot{\chi} = \phi$
$\dot{\phi} = \frac{1}{\chi(\tau)} - \frac{\phi}{\tau}$	$\dot{\phi} = \frac{1}{\chi(\tau)}\left[\frac{\kappa\,\lambda\,\mu}{\chi(\tau)\psi(\tau)\zeta(\tau)}\right]^{\gamma-1}$
$\dot{\psi} = \varphi$	$\dot{\psi} = \varphi$
$\dot{\varphi} = \frac{1}{\psi(\tau)} - \frac{\varphi}{\tau}$	$\dot{\varphi} = \frac{1}{\psi(\tau)}\left[\frac{\kappa\,\lambda\,\mu}{\chi(\tau)\psi(\tau)\zeta(\tau)}\right]^{\gamma-1}$
$\dot{\zeta} = \theta$	$\dot{\zeta} = \theta$
$\dot{\theta} = \frac{1}{\zeta(\tau)} - \frac{\theta}{\tau}$	$\dot{\theta} = \frac{1}{\zeta(\tau)}\left[\frac{\kappa\,\lambda\,\mu}{\chi(\tau)\psi(\tau)\zeta(\tau)}\right]^{\gamma-1}$

(4.25)

The initial conditions for $t < t_L$ are $\dot{\chi}(0) = \dot{\psi}(0) = \dot{\zeta}(0) = 0$ and $\chi(0) = \psi(0) = \zeta(0) = 0$. For $t \geq t_L$, the initial conditions are $\chi(0) = \kappa$, $\psi(0) = \lambda$, and $\zeta(0) = \mu$, and the dimensionless velocities $\dot{\chi}(0)$, $\dot{\psi}(0)$, and $\dot{\zeta}(0)$ are taken from the output for $t < t_L$ or supplied independently. The ODEs in Eq. 4.25 were solved with a Runge-Kutta 45 algorithm.

Before comparing to data, it is instructive to highlight some of the general features of the solutions to these models. For $\gamma = 5/3$ and typical initial conditions, Fig. 4.7 shows the evolution of $\{\chi, \psi, \zeta\}$ and $\{\dot{\chi}, \dot{\psi}, \dot{\zeta}\}$. Here, the initial size of the plasma parallel to the target surface ($\hat{x}$ and $\hat{y}$) is taken to be the same (*i.e.* a circular spot size), so that $\chi = \psi$ and $\dot{\chi} = \dot{\psi}$. The plasma size perpendicular to the target surface ($\hat{z}$) is taken to be smaller ($\zeta(0) < \chi(0)$).

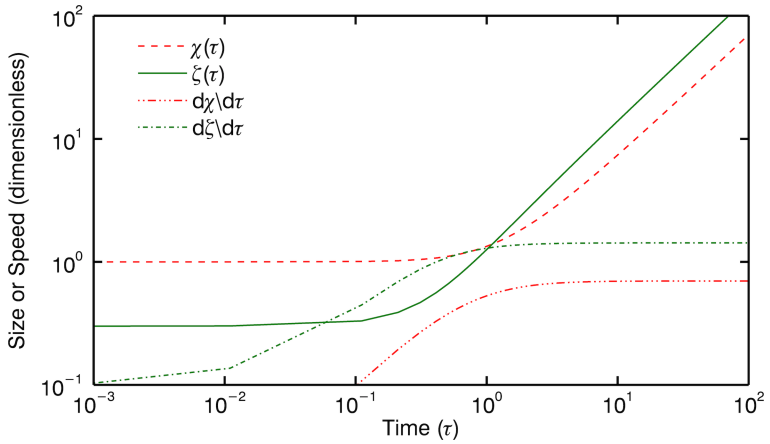

Figure 4.7: Solutions to Eq. 4.24 for components parallel (dashed) and perpendicular (solid) to the target surface. Also shown are the corresponding component velocities (dash dot). The solutions are for $\gamma = 5/3$, $\kappa = 1$, $\mu = 0.3$, $\dot{\chi}(0) = 0.1$, and $\dot{\zeta}(0) = 1$.

It can immediately be seen that due to the difference in plasma size in $\hat{z}$ versus $\hat{x}$ and $\hat{y}$, an anisotropic pressure gradient is set up that drives the plasma to quickly expand along $\hat{z}$ until reaching the parallel size around $\tau = 1$. Afterwards, all three directions expand nearly linearly with constant velocity as the plasma reaches a free-streaming state. As a result of this behavior, the plasma develops and maintains an ellipsoidal shape, with the long axis perpendicular to the target surface (see Fig. 1.2). It can also be seen that the velocity of the plasma increases (almost) linearly with distance, so that the farthest plasma elements are moving fastest. Additionally, changing γ affects how quickly the plasma expands, with plasmas of increasing γ moving more slowly.

4.2.4 Comparison to Data

The framework developed in Sections 4.2.2 and 4.2.3 can be applied to the datasets in Section 4.1 to extract further properties of the LPP. Density and temperature profiles from each fluid model were compared to all datasets (see Table 4.1). The profiles were taken from Eqs. 4.14-4.15 and 4.19-4.20, where for each, x and y were set to zero since data was taken only along $\hat{z}$. Additionally, derived quantities like the expansion speed and the total number of ablated

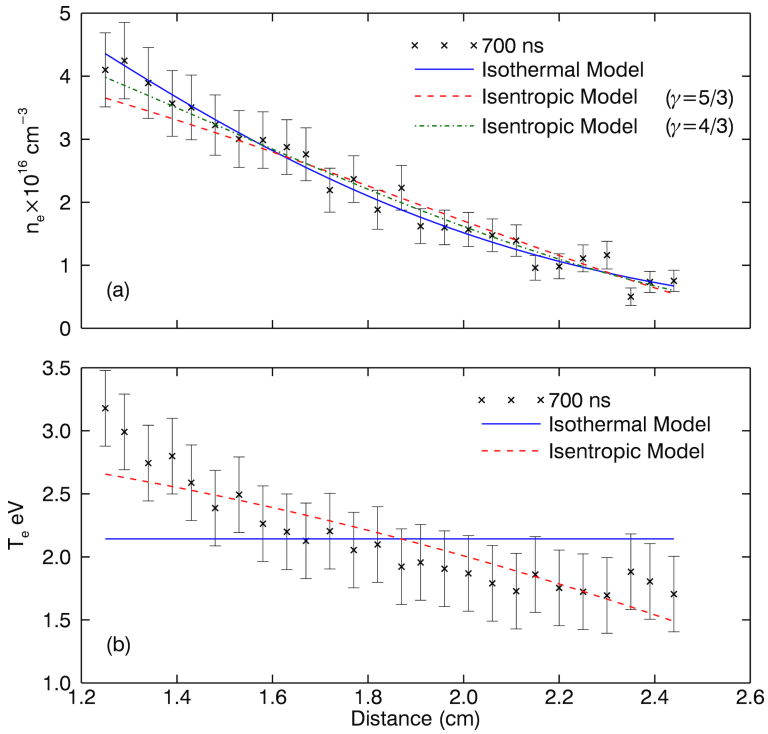

Figure 4.8: Isothermal (solid) and isentropic model fits to Thomson scattering data at $t = 700$ ns for $\gamma = 5/3$ (dashed) and $\gamma = 4/3$ (dash-dot). (a) Thomson scattering-derived density data and model best fits. (b) Thomson scattering-derived temperature data and model best fits.

particles were compared to the scaling laws in Eqs. 4.5 and 4.8.

The general shape of the expanding plasma is already known from the properties of the solutions to the fluid equations (see Section 4.2.3). The specific shape can be calculated by solving Eq. 4.24 using the laser spot radius for $X(0) = Y(0)$, an initial expansion distance $Z(0) \sim 0.1 - 0.5 \cdot X(0)$, and initial expansion speeds calculated from the $t < t_L$ equation. The only free parameter is the adiabatic index γ, which was set as either $\gamma = 5/3$ (monotonic gas) or $\gamma = 4/3$. The latter was chosen to mimic the effects of recombination (which are not modeled), since the temperature would then scale like $T \propto t^{-1}$ (see Section 4.2.1).

Solving the ODEs of Eq. 4.25 yields the dimensionless evolution of the plasma. To proceed, a specific point in the evolution is needed in order to extract dimensional parameters.

Fig. 4.8 shows example Thomson scattering data, along with best fit density and temperature profiles from the isothermal (Singh) and isentropic (Anisimov) models. The best fit profiles give a plasma size $Z(t)$ along $\hat{z}$ and the density and temperature at $z = 0$ at time t. Using the scalings from the ODEs, $Z(t)$ can be converted to $\zeta(\tau)$ and used to extrapolate the corresponding plasmas sizes in $\hat{x}$ and $\hat{y}$ at time t (see, for example, Fig. 4.7). With all three plasma dimensions, the total number of ablated particles N_0 can then be calculated from Eq. 4.14 or 4.19.

As can be seen in Fig. 4.8a, both the isothermal and isentropic models fit the density data well, though the isothermal model is generally a better fit. Furthermore, the choice of γ has little effect on the isentropic fit, though it has a greater effect on the model solutions. As expected, only the isentropic model fits the temperature data well (see Fig. 4.8b). For both models, the extracted plasma size was proportional to the delay time ($Z(t) \propto t$) at later times ($t > 400$ ns), as expected from the fluid solutions. Because the isothermal model associates the plasma size with the $1/e$ edge while the isentropic model associates it with the leading edge, the isothermal model tends to yield smaller expansion speeds and lower total energies. Since the isentropic model was generally a good fit for both density *and* temperature data, it will be assumed for the remainder of the analysis, unless otherwise stated.

The results of two example analyses for a high and low incident laser intensity and for both values of γ are shown in Table 4.2. As can be seen, the effect of increasing γ is to slow down the plasma expansion, resulting in a smaller plasma size at a given time and lower total energy. Also, the plasma size $Z(t)$ derived from the temperature fit tends to better agree with the density-derived value for $\gamma = 4/3$. It is interesting to note the seemingly slow expansion speed (also seen in the isothermal solutions), given that several experiments show plasma elements moving at several hundred km/s (see, for example, Figs. 4.5 and 4.6). However, these speeds (and those from shorter time delays) are consistent with the measured time-of-flight values and the spectroscopic data, suggesting that part of the discrepancy is because these speeds are not the actual leading edge, but rather the leading edge of a slower plasma element containing most of the mass. The reason it must be more massive is that

Run	Run 1	Run1	Run 3	Run 3
I_0 (10^{10} W cm^{-2})	18	18	2	2
Time t (ns)	500	500	700	700
γ	5/3	4/3	5/3	4/3
$X(t) = Y(t)$ (cm)	2.0	2.8	1.3	1.8
$Z(t)$ (cm)	3.0	3.7	2.8	3.3
$\dot{Z}(t)$ (km/s)	60	76	41	50
N_0 (10^{17})	4.0	5.4	1.4	2.1
E_0 (J)	19	23	2	3
T_0 (eV)	290	260	90	85

Table 4.2: Derived quantities using the isentropic fluid model for a high and low incident laser intensity I_0 and two values of the adiabatic index γ. $Z(t)$ is derived from fits to the data, allowing $X(t)$ and $Y(t)$ to be extrapolated from the ODE solutions. $\dot{Z}(t)$ is the expansion speed, N_0 is the total number of ablated particles, E_0 is the initial (total) plasma energy, and T_0 is the corresponding initial plasma temperature.

this element is the first to appear in the Thomson-scattered data, meaning it represents the smallest detectable density. The isothermal model also under-predicts the fastest plasma elements, even though the derived expansion speed actually corresponds to the $1/e$ edge. To calculate the isothermal leading edge speed, the number of particles moving faster than a given speed v_0 is derived from Eqs. 4.14 and 4.12 as

$$N_{v>v_0} = \sqrt{\frac{2}{\pi}} \left(\frac{N_0}{\dot{Z}} \right) \int_{v_0}^{\infty} dv_z \exp \left[-\frac{v_z^2}{2\dot{Z}^2} \right] \tag{4.26}$$

For typical values of $\dot{Z}$ and N_0, $N \to 0$ for $v \gtrsim 150$ km/s. Thus, both models fail to account for the fastest plasma elements seen in experiments. Evidently, the origin of the fastest particles, then, is not due to pressure gradients modeled by the fluid equations. An alternate explanation is discussed in Section 4.3.

Using N_0 and the value of $\beta(\gamma)$ set by $Z(t)$, the total plasma energy can also be calculated from $E = \beta(\gamma)\, N_0\, m$, where m is the mass of a carbon particle. The results, listed in Table 4.2, surprisingly show that the total plasma energy is significantly less than the laser energy (the total energy is even smaller for the isothermal model), indicating that most of the laser energy is not coupled into the expanding plasma. Most likely, the majority of the energy goes into shocking and deforming the solid target. The corresponding initial isothermal temperature $T_0 = E(Nk_B)^{-1}$ is consistent, for $\gamma = 4/3$, with the measured temperatures through adiabatic cooling ($T(t) = T_0(V_0/V)^{\gamma-1}$). For $\gamma = 5/3$, the predicted temperatures after adiabatic cooling are much smaller (< 0.5 eV) than the measured values, further suggesting that the plasma γ is closer to 4/3. Note also that small plasma energies are not inconsistent with expansions in a magnetic field. Because the plasma is ellipsoidal, the energy required to fully expel an external magnetic field B goes like $E_B = \frac{B^2}{8\pi}(\frac{4}{3}\pi ab^2)$, where a is the major radius and b is the minor radius. Typical parameters are: $B = 300$ G, $a = 15$ cm, and $b = 7.5$ cm. The required energy is then $E \simeq 1.1$ J.

As can be seen in Table 4.2, there is a pronounced effect on derived quantities with incident laser intensity. Expanding to all data runs, Fig. 4.9 shows this effect on the initial energy E_0, total ablated particles N_0, expansion speed $v_{expansion}$, and the laser-to-plasma energy efficiency for both adiabatic indexes. Also included, where applicable, are the corresponding predicted scaling laws from Section 4.2.2.

Unsurprisingly, the total plasma energy increases with laser intensity, as does N_0. The dependence of N_0 on intensity corresponds well with the predicted $I_0^{5/9}$ scaling (see Eq. 4.8 and Fig. 4.9b). The expansion speed shows a weak dependence on intensity, consistent with Eq. 4.5 (see Fig. 4.9c). Finally, the ratio of plasma energy to laser energy E_0/E_{laser} shows a strong dependence on intensity (see Fig. 4.9d). Plotting the ratio versus laser energy or spot size indicates that the laser spot size on target is primarily responsible for the observed intensity dependence (*i.e.* large spot sizes have lower energy conversion efficiencies and *vice versa*). In all cases, the adiabatic index does not have a significant effect.

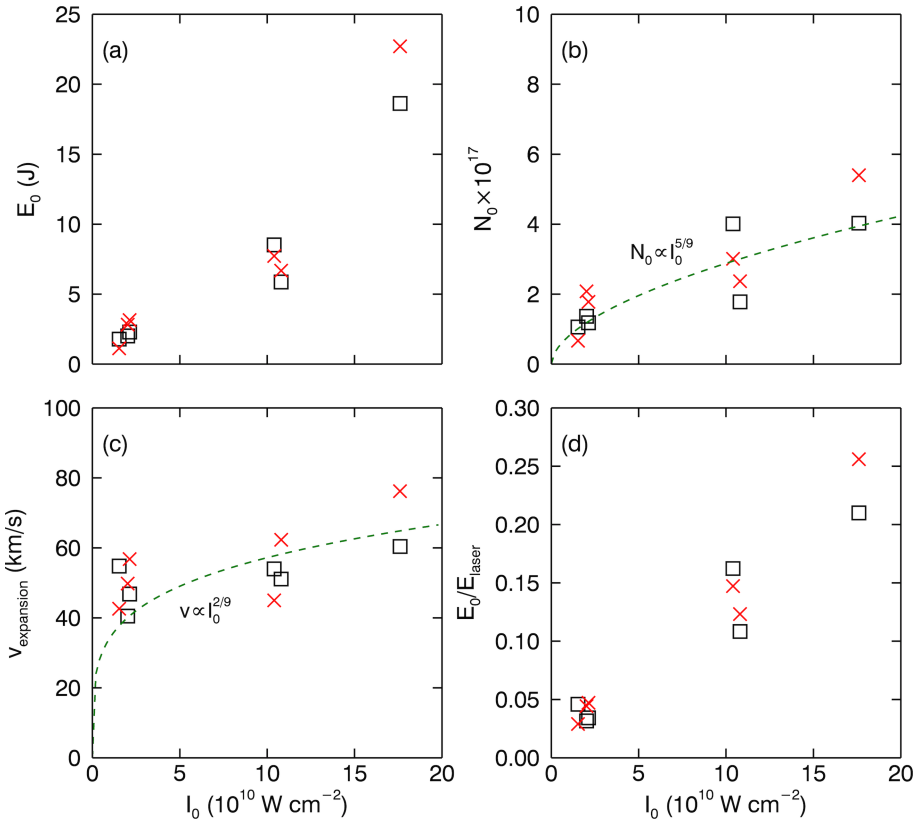

Figure 4.9: Derived quantities versus incident laser intensity I_0 for $\gamma = 5/3$ (squares) and $\gamma = 4/3$ (crosses). (a) Initial plasma energy E_0. (b) The total ablated particles N_0 and the predicted scaling $N_0 \propto I_0^{5/9}$ (dashed). (c) The expansion speed $v_{expansion}$ and the predicted scaling $v \propto I_0^{2/9}$ (dashed). (d) The ratio of plasma energy to laser energy E_0/E_{laser}.

4.3 1-D Laser-Target Simulations

While the fluid models developed in Section 4.2 are useful for describing the smooth, large-scale behavior of the LPP, they are limited to a neutral, single-fluid description that only models an already ablated, adiabatic plasma. To expand upon those models, the HELIOS [45] code was used to simulate the laser-target interaction and subsequent evolution for a single fluid with co-moving electrons and ions. Additionally, the code models atomic kinetics and radiation transport, allowing a detailed study of charge-state evolution and the effects of recombination.

4.3.1 HELIOS

HELIOS is a one-dimensional, Lagrangian radiation-magnetohydodynamic (MHD) simulation code. It solves the equation of motion for a single fluid with pressure contributions from electrons, ions, radiation, and magnetic fields. The electrons and ions are assumed to have Maxwellian distributions set by their respective temperatures, T_e and T_i. The code uses PROPACEOS equation of state (EOS) data and an inverse bremsstrahlung model to calculate laser energy deposition. Radiation emission and absorption are coupled to the electron temperature, and radiation transport is computed with a flux-limited diffusion or multi-angle transport model.

The code can be set up in planar, cylindrical, or spherical geometries. For a given geometry, one or more regions (*e.g.* a target) are defined, and within each region multiple zones are created. Each zone has a constant mass but flexible boundaries, allowing it to change size and location during the simulation. Material properties (species, mass density, EOS, thermal conductivity) can be set for each region, and multiple parameters (wavelength, incidence angle, pulse width, intensity) can be set for an incident laser.

While HELIOS is primarily designed to simulate high-energy density environments (such as the shock wave generated within a target by an incident laser), it can also model and track low density, low mass elements (zones) ablated from a target into vacuum. The validity of the simulation for these ablated elements is similar to that for the fluid models, as discussed in Section 4.2.1. As long as the electron and ion populations can be reasonably assumed to be Maxwellian, the code should be a valid approximation. This is the case for the time-scales of interest here.

For the simulations presented in this section, the following simulation parameters were used. Being the closest to the theoretical models, a planar geometry was employed. Only one region was created for the target. While the target thickness was largely irrelevant for the ablated zones (as long as it was larger than $\sim$ 100 μm), it was set to 2.5 mm in order to avoid reverse propagating shocks at later times. The code automatically generates

a mass distribution (generally Gaussian) for the zones within the target region. In order to sufficiently resolve the ablated plasma, 750 zones were used, since only $5 - 25$ % are actually ablated. The target region was setup as solid carbon, modeled on semiconductor grade graphite from POCO Graphite©. The region had an initial temperature $T_0 = 0.025$ eV (room temperature), mean atomic weight $A = 12.011$ amu, mass density $\rho = 2.15$ g cm^{-3}, PROPACEOS carbon (C) equation of state and opacity, and thermal conductivity at solid density $\kappa = 72$ W m^{-1} K^{-1}. For $\rho < 2$ g cm^{-3}, a Spitzer thermal conductivity was used. If a plastic (high-density polyethylene) target was used, the target region was setup as $A = 4.667$ amu, $\rho = 0.95$ g cm^{-3}, PROPACEOS CH_2 equation of state and opacity, and $\kappa = 0.47$ W m^{-1} K^{-1} for $\rho > 0.9$ g cm^{-3}. A Gaussian laser pulse was defined with a wavelength $\lambda = 1053$ nm, an incidence angle $\theta = 0$ deg, a pulse width $\Delta t = 25$ ns, and an incident intensity $I_0 = 10^9 - 10^{12}$ W cm^{-2}. To facilitate computation times, the electron and ion temperatures were set equal, since $T_e \neq T_i$ simulations showed that the two temperatures do not decouple significantly during the times of interest. The simulation was run for up to 500 ns, with computed parameters recorded every 1 ns for $0 \leq t \leq 100$ ns, and every 10 ns thereafter.

4.3.2 Code Validation

Before extracting information not readily available by measurement, it is important to verify the validity of the simulations. Figs. 4.10a and 4.11a show electron density and temperature contour streak plots, respectively, from a HELIOS simulation at $I_0 = 10^{11}$ W cm^{-2}. Figs. 4.10b-c and 4.11b-c compare spatial and temporal lineouts from the simulation with data at a comparable intensity and distance/time from Run 1 (see Table 4.1). As can be seen, there is generally good qualitative agreement between the simulation and measurements.

In Fig. 4.10 the density was scaled from 1D ($1/r$) to 3D ($1/r^3$) and normalized to the maximum measured density. Closer to the target (~ 1 cm), the simulated density is higher than measured, though at both 250 and 500 ns, the density then scales with distance similarly to the data. The temporal behavior of the density is less similar. HELIOS does

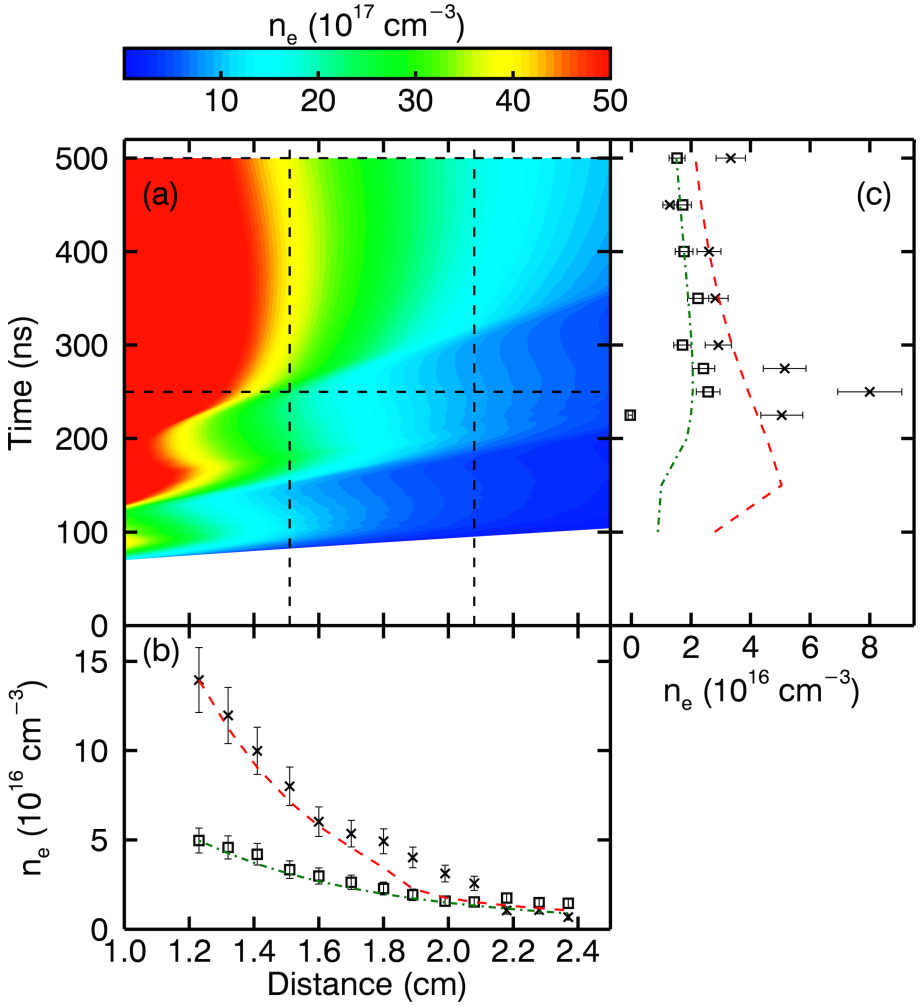

Figure 4.10: (a) Streaked contour plot of electron density n_e from HELIOS with $I_0 = 10^{11}$ W cm^{-2}, where n_e has been scaled from 1D to 3D. Spatial and temporal profiles from HELIOS (dashed) are compared to experimental values from Run 1 in (b) and (c), respectively. (b) Data at 250 (crosses) and 500 (squares) ns is compared to HELIOS profiles at the same times (dashed and dot dash, respectively). (c) Data at 1.5 (crosses) and 2.1 (squares) cm is compared to HELIOS profiles at 0.5 (dashed) and 1.1 (dot dash) cm. Qualitative agreement between simulation and experiment required comparing lineouts ~ 1 cm closer to the target in HELIOS relative to the location of measured values.

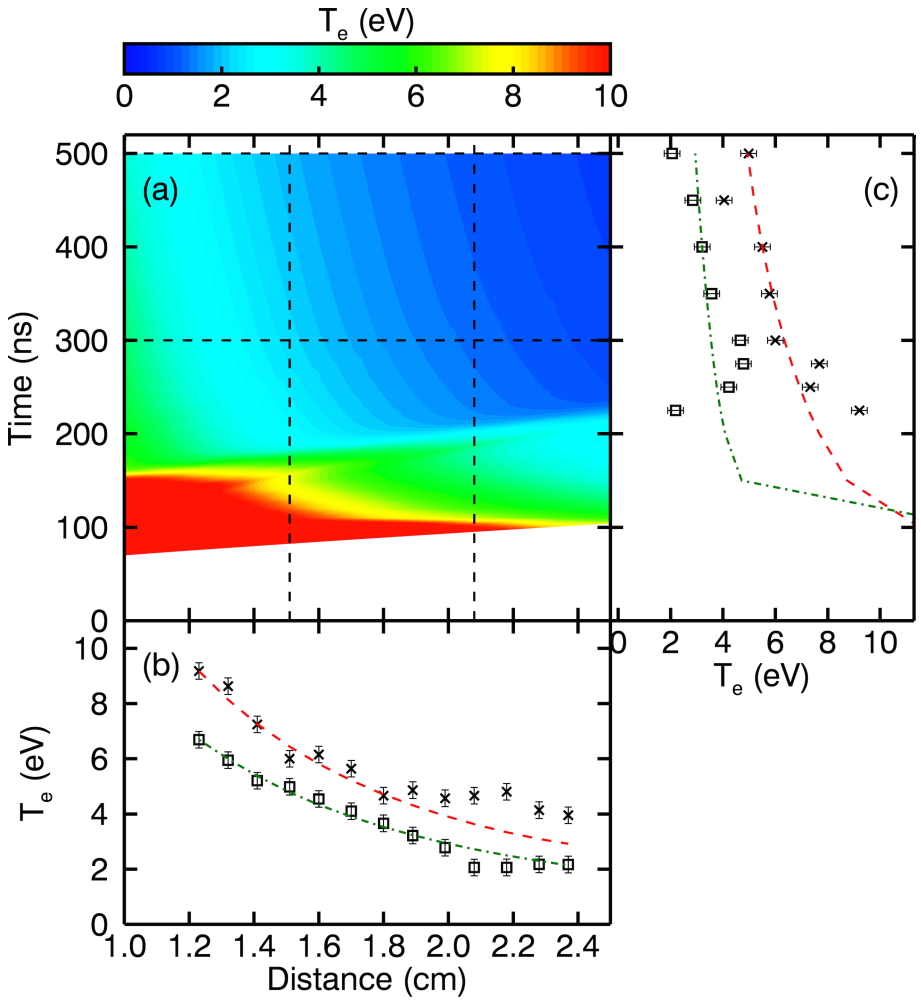

Figure 4.11: (a) Streaked contour plot of electron temperature T_e from HELIOS with $I_0 = 10^{11}$ W cm^{-2}. Spatial and temporal profiles from HELIOS (dashed) are compared to experimental values from Run 1 in (b) and (c), respectively. (b) Data at 300 (crosses) and 500 (squares) ns is compared to HELIOS profiles at the same times (dashed and dot dash, respectively). (c) Data at 1.5 (crosses) and 2.1 (squares) cm is compared to HELIOS profiles at 0.5 (dashed) and 1.1 (dot dash) cm. Qualitative agreement between simulation and experiment required comparing lineouts ~ 1 cm closer to the target in HELIOS relative to the location of measured values.

predict several "waves" of increased density at a given location as seen in data (see Figs. 4.1 and 4.2). However, the timing of those waves doesn't agree well. In general, it appears that for the measured density as a function of time at a given distance from the target, a good qualitative fit between simulation and data requires looking $\sim$ 1 cm closer to the target in the simulation. The formation of the density waves is a result of how laser energy is deposited into the plasma. Since the inverse bremsstrahlung process is inversely proportional to density, as more mass is ablated from the target, less laser energy is absorbed. This in turn causes less mass to be ablated, increasing laser absorption and repeating the process. Why the simulation predicts these waves occur closer to the target than seen experimentally is unclear, though it may have to do with the 1D nature of HELIOS.

Like the density, the electron temperature calculated by HELIOS (normalized to the maximum measured temperature) scales similarly with distance to measured values (see Fig. 4.11). In this case, the simulation temperature is slightly lower than the measured value at the same location and time. Also like the density, the temporal profile of temperature at a given distance is qualitatively similar only when comparing data to simulation profiles $\approx$ 1 cm closer to the target.

Fig. 4.12 shows various simulation parameters versus incident intensity, in comparison with Fig. 4.9. The number of particles in a zone was calculated by multiplying the density in that zone by the zone size and a reference laser spot size. The plasma energy was calculated by adding the kinetic energy in all ablated zones (using the derived number of particles and HELIOS-calculated zone speed) with the HELIOS-calculated internal energy in those zones. The total laser energy was derived by summing the HELIOS-calculated, time-integrated deposited laser energy in all zones.

In Figs. 4.9a-b, there is good qualitative and quantitate agreement in the total number of ablated particles N_0 and the total plasma energy E_0 between HELIOS and the derived values from experiment. In Fig. 4.9c, the dependence of expansion speed $v_{expansion}$ (defined as the speed of the leading zone) on intensity agrees well with the predicted scaling at lower intensities, while at higher intensities it begins to diverge as expected, since the predicted

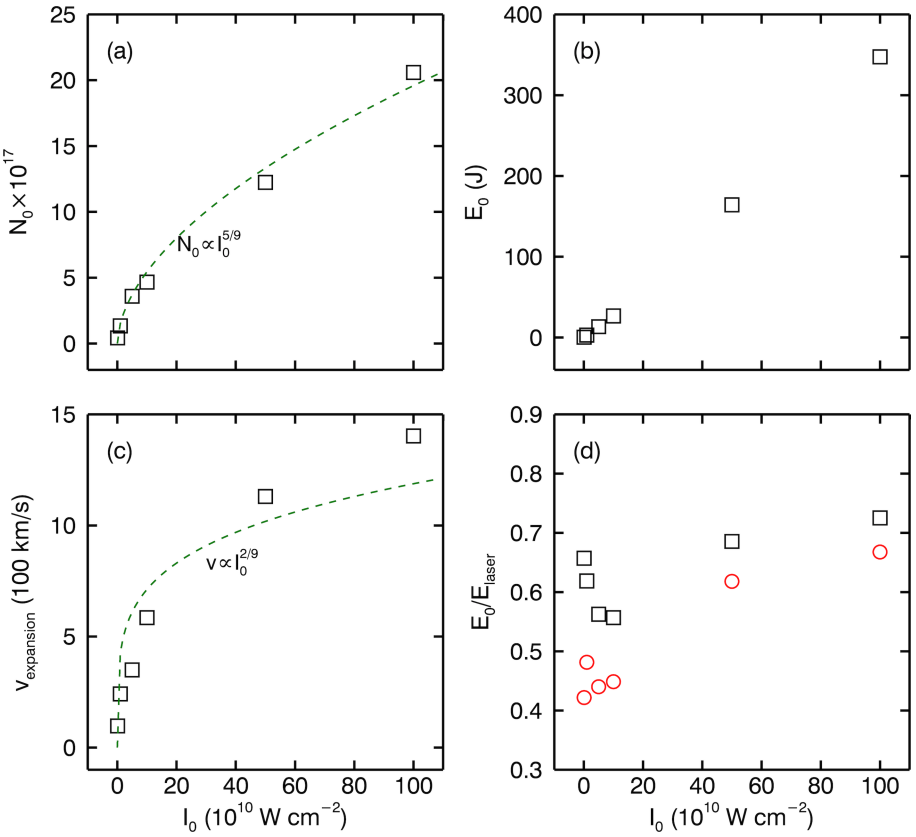

Figure 4.12: HELIOS plasma parameters (squares) versus incident intensity I_0. (a) The total ablated particles N_0 and the predicted scaling $N_0 \propto I_0^{5/9}$ (dashed). (b) Total plasma energy E_0. (c) The expansion speed $v_{expansion}$ and the predicted scaling $v \propto I_0^{2/9}$ (dashed). (d) The ratio of total (squares) and kinetic-only (circles) plasma energy to laser energy E_0/E_{laser}.

scaling starts to become invalid. At all intensities, the magnitudes of the velocities are generally an order of magnitude greater than the measured values. This is also expected, since in general the diagnostics were not able to detect the actual leading edges, but only a slower, more massive edge (the diagnostic that does detect the leading edge, the bdot probe, sees speeds consistent with HELIOS). Unlike the other parameters, the ratio of plasma energy to laser energy E_0/E_{laser} is markedly different in the simulations (see Fig. 4.9d). This discrepancy is primarily because HELIOS calculates not only the plasma's kinetic energy but also its internal energy, which was up to 35 % of the total energy. This additional energy increases the total efficiency of the the laser-to-plasma energy conversion. Furthermore, since

the internal energy at the lowest intensities is a large fraction of the total energy, but the total kinetic energy increases more quickly than the internal energy as intensity increases, this also accounts for the dip in the efficiency at $I_0 = 10^{11}$ W cm^{-2}. The plasma kinetic-only energy to laser energy ratio is also shown in Fig. 4.9d.

4.3.3 Charge State Evolution

HELIOS provides substantial information on the spatial and temporal evolution of the plasma charge states. An overview of these evolutions for CII (C^{+1}) to CVII (C^{+6}) at various incident laser intensities is shown in Fig. 4.13. The general trend is that of increasing charge state with intensity in the leading edges of the plasma. However, the nuances of these trends is more complex. In Fig. 4.14, Fig. 4.13 has been condensed by looking at only $t = 500$ ns. Fig. 4.14a shows the average charge state $\overline{Z}$ as a function of intensity I_0. While $\overline{Z}$ initially increases with I_0 as might be expected, it plateaus around $I_0 = 10^{11}$ W cm^{-2} as a larger and larger proportion of the ablated population remains in a lower charge state. This can be clearly seen in Fig. 4.14b, where, for example, the relative population of CI (C^{+0}) initially decreases to ∼10% before increasing again to almost 60% for $I_0 > 10^{11}$ W cm^{-2}, even though the populations of CV-CVII (C^{+4}-C^{+6}) also increase. This implies that despite high charge states at the leading edge of the plasma, the majority of the plasma mass lies in low charge state populations. In addition to being the most massive, the lowest charge states are also the slowest, as seen in Fig. 4.15.

Though most of the mass is slow, it is of particular interest to investigate the properties of the leading edge(s) of the plasma, given that this population will primarily interact with other environments (external magnetic field, ambient plasma, *etc.*). As can be seen in Figs. 4.13 and 4.15, the leading edge exhibits clear stratification by charge state. The fastest elements, especially at higher intensities, are primarily CVII, followed by a thin layer of CVI, and then a more substantial layer of CV. Farther behind is a mixture of CI-CV, with the lowest charge states dominating near the target.

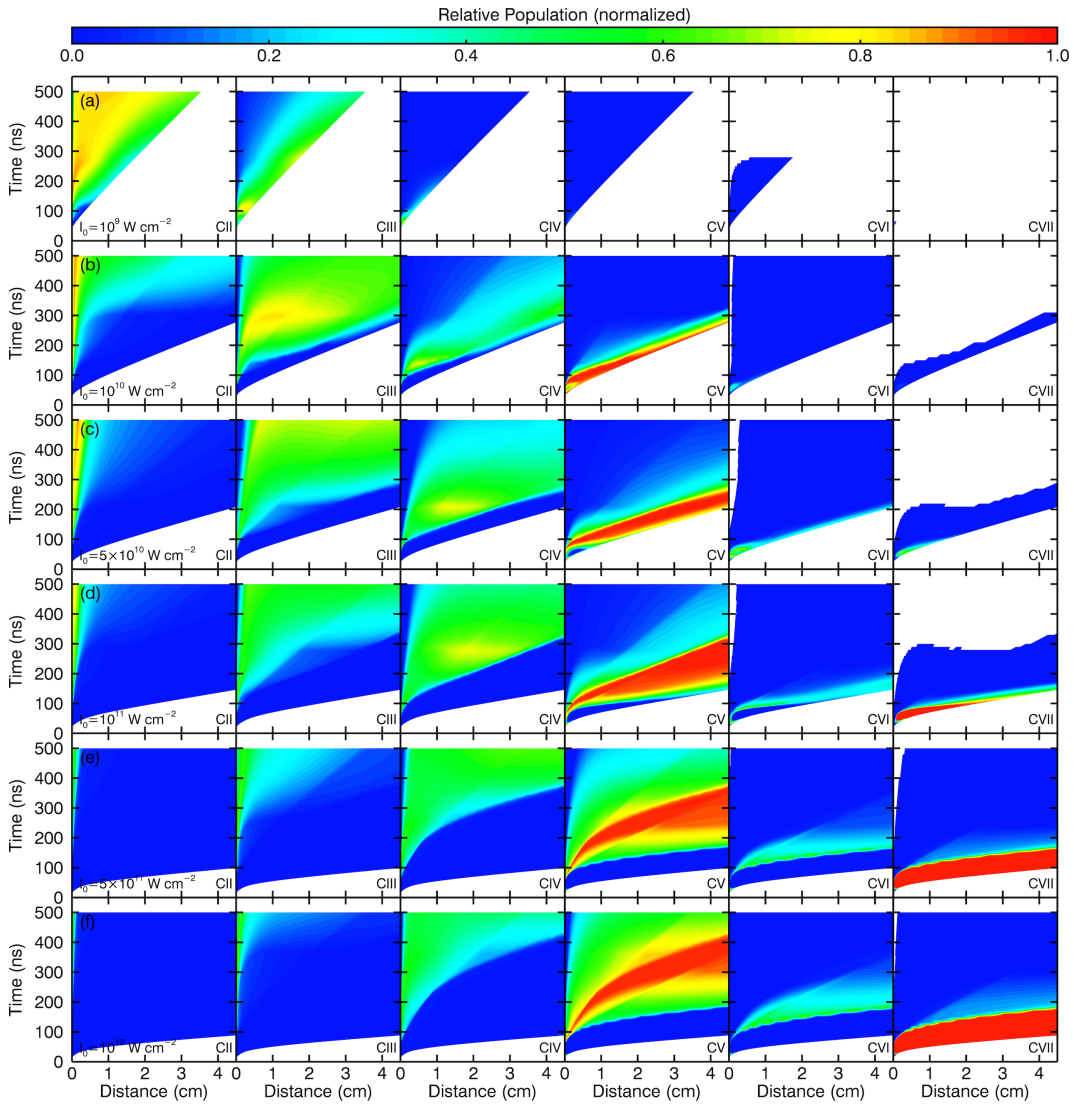

Figure 4.13: HELIOS contour streak plots of relative populations of charge states CII-CVII (C^{+1}-C^{+6}) for various incident laser intensities I_0 (rows a-f).

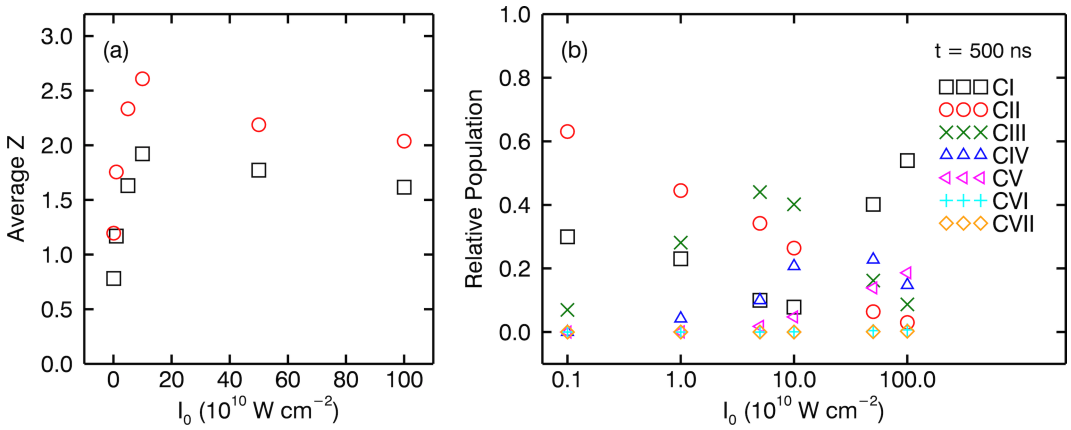

Figure 4.14: (a) HELIOS-calculated average charge state $\overline{Z}$ as a function of incident laser intensity I_0 at $t = 100$ ns (circles) and $t = 500$ ns (squares). (b) Relative populations of charge states CI-CVII (C^{+0}-C^{+6}) as a function of I_0 at $t = 500$ ns.

This stratification can also been seen in the velocity distribution of each charge state (see Figs. 4.16 and 4.15). Here, an average velocity for each ion species was calculated from a weighted mean of the relative population of that species in each ablated zone and that zone's speed. A weighted standard deviation was similarly calculated, allowing the construction of Gaussian distributions (recall HELIOS assumes the electron and ion populations are Maxwellian at all times). A clear separation by charge state in velocity space can be seen. Fig. 4.16 can be compared to Fig. 4.5, which was derived from spectroscopy measurements at a similar time and laser intensity. There is good agreement quantitatively, with both showing a CV distribution centered near 200 km/s, a CIV distribution centered near 100 km/s, and CIII and CII centered near 50 km/s and 25 km/s, respectively. Though unable to be measured spectroscopically, Fig. 4.16 also shows that the CVI and CVII distributions are substantially faster (400-450 km/s) than CV. While these states are consistent with some of the fastest elements seen in experiments, it is not clear whether there is a sufficient population of them to influence external elements like an ambient plasma (the relative population tends to be below 0.2%). In contrast, the next fastest state, CV, generally has a significantly higher relative population (up to 20%) for $I_0 > 10^{11}$ W cm^{-2}. It is interesting to note, however, that the two orders of magnitude difference between the populations of CVI/CVII

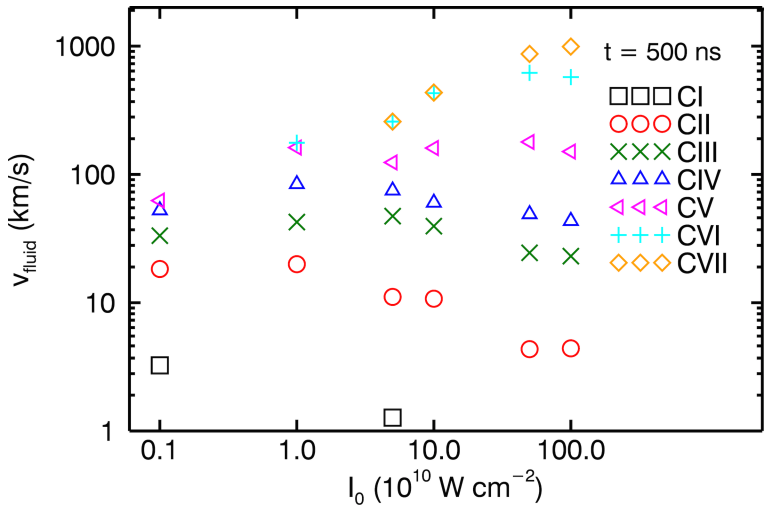

Figure 4.15: Population-weighted average fluid velocities of charge states CI-CVII (C^{+0}-C^{+6}) as a function of I_0 at $t = 500$ ns.

and CV are consistent with the sensitivity limits of the Thomson scattering diagnostic.

Given the results in Figs. 4.14 and 4.15 (or 4.16), it is of interest to determine which charge state(s) (the most massive or fastest) is(are) dominant, in the sense of which ion species is most able to influence the background magnetic field or ambient plasma. A useful measure, then, is the average kinetic energy in a given charge state. The results are shown in Fig. 4.17, which indicates that at typical incident laser intensities ($I_0 > 10^{11}$ W cm^{-2}), CV (C^{+4}) is the dominant charge state.

4.4 Summary

Using multiple diagnostics, along with 3D fluid models and the 1D HELIOS code, the following results were obtained:

- Thomson scattering measurements initially detect a high temperature, dense, slow moving plasma that cools and dissipates in time. The initial plasma edge is followed soon after by a second plasma edge that is slightly cooler and less dense than the first. HELIOS simulations indicate that this is an effect of how the laser is deposited into

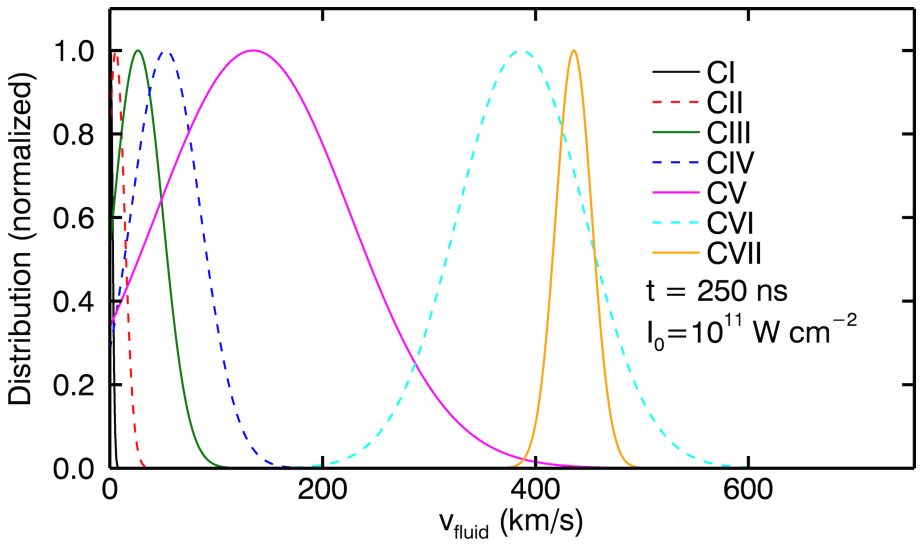

Figure 4.16: HELIOS-derived, normalized velocity distributions by charge state for $I_0 = 10^{11}$ W cm^{-2} and $t = 250$ ns.

the plasma/target.

- Spectroscopic measurements reveal a distinct separation by charge state in velocity space, with higher charge states moving faster. HELIOS simulations similarly see this effect, and agree well quantitatively with the velocity distributions.

- Electron density and temperature data agree well with an isentropic fluid model of an adiabatic plasma. The application of the model allows additional parameters – including the total number of ablated particles, total plasma energy, and expansion speed – to be calculated. These parameters agree well with theoretical scaling laws, but indicate that the plasma contains only a fraction of the laser energy and cannot account for the fastest observed plasma elements. Additionally, the isentropic model suggests that the adiabatic index $\gamma = 4/3$, which is consistent with a plasma that is dominated by collisional recombination.

- HELIOS simulations agree well with the measured electron density and temperature dependence on distance from the target, but have trouble matching their dependence on time. Nonetheless, the total number of ablated particles and total plasma energy

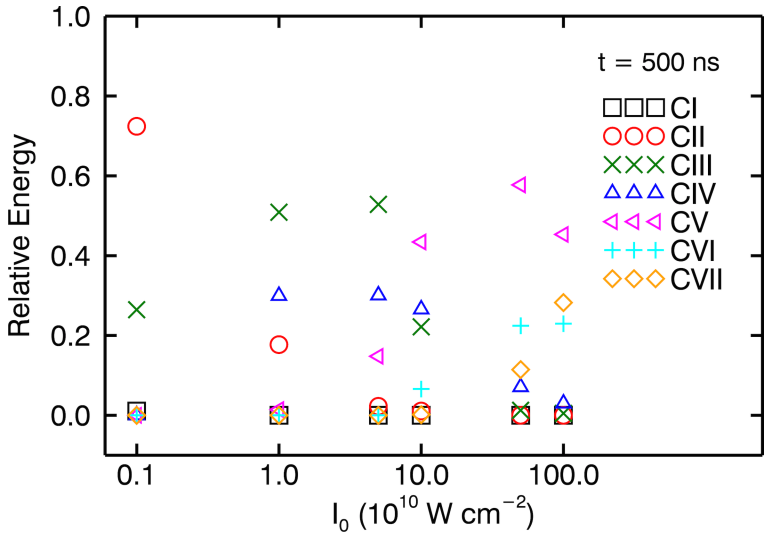

Figure 4.17: Relative average kinetic energy of charge states CI-CVII (C^{+0}-C^{+6}) as a function of I_0 at $t = 500$ ns.

from the simulation are quantitatively similar to the values derived from measurements. The HELIOS expansion speeds are also consistent with speeds seen by bdot probes and, as expected, higher than the slower edge speeds measured by Thomson scattering or spectroscopy. However, relative to empirically derived values, the ratio of total plasma energy to laser energy is larger. This effect is a result of additional internal plasma energy not captured by the fluid models.

- HELIOS simulations reveal a spatial-temporal stratification of charge states. While the fastest plasma elements have the highest charge states (CVI/CVII), most of the mass resides in ions with low charge states. While they have two orders of magnitude less mass than lower charge state ions, the speed of the fastest ion species agrees well with the observed fastest plasma elements. The relative populations and speeds for each ion species indicate that the charge state with the most energy (the dominant charge state) is CV at typical incident laser intensites.

CHAPTER 5

Laser Scattering of Plasmas in a Weakly Collective Regime

Laser scattering – a general class that includes Thomson, Rayleigh, and Raman scattering – is a powerful tool for diagnosing plasma state parameters, such as ion and electron temperature and density. The technique is non-invasive and non-perturbative, while still providing high spatial and temporal resolution over a large parameter regime. The theory of laser scattering (largely in response to radio wave scattering in the ionosphere) was already in development [24, 69] before the invention of the laser, and its use as a diagnostic was proposed soon after [9]. Already by the late 1960s, laser scattering was being used to study collisionless shocks [18, 78, 62]. Since then, the diagnostic has been employed in a wide variety of plasma environments and parameter regimes, including non-magnetized high-density ($> 10^{18}$ cm-3, $\sim$ keV) laser-driven plasmas [28, 26, 66], non-magnetized low-density ($< 10^{14}$ cm-3, $\sim$ eV) arc or discharge plasmas [82, 5], θ-pinches [78], and tokamaks [36, 90, 62].

Unlike these previous efforts, the work presented in this chapter involves the development of a Thomson scattering diagnostic in a novel environment - a moderate density ($\sim 10^{15} - 10^{17}$ cm^{-3}), low temperature (< 20 eV) laser-driven, magnetized plasma. Furthermore, the plasmas are large-scale, allowing detailed measurements several cm from the target and hundreds of ns after target ablation. This unique collection of parameters allowed for the first time high-resolution spatial imaging of the transition from a non-collective to collective scattering regime. These results and related efforts are presented in sections 5.2-5.3, while the theory of laser scattering is presented in section 5.1. Efforts to develop the laser systems necessary to run the Thomson diagnostic are detailed in the Appendicies, while results

relevant to collisionless shocks are detailed in Chapter 4.

5.1 Theory of Laser Scattering

The scattering of electromagnetic radiation by particles can be divided into three types: scattering by charged particles, *i.e.* Thomson scattering; elastic scattering by neutral particles, *i.e.* Rayleigh scattering; and inelastic scattering by neutral molecules with rotational and vibrational modes, *i.e.* Raman scattering. There are many excellent resources that cover the theory of laser scattering – see for example [74, 21, 17, 69]. An abbreviated outline of the theory is provided here. The main focus of this section will be Thomson scattering, with a brief discussion of Raleigh scattering provided in section 5.1.8.

5.1.1 Assumptions

Several conditions will be assumed throughout this section.

Due to their much larger mass, scattering by ions will be neglected. The recoil of an electron by an incident photon (the Compton effect) is also neglected, which is justified for incident photon energies much less than the electron rest energy, $\hbar\omega \ll m_e c^2$. The electrons are assumed to be traveling slow compared to the speed of light, $v \ll c$, and so are treated non-relativistically, except where stated otherwise. For this reason, the effect of the incident radiation's magnetic field on an electron is also ignored.

The scattered radiation is detected in the far field, $R \gg L, \lambda_i$, where L is a characteristic length scale in the scattering volume and λ_i is the incident wavelength. The frequency of the incident radiation ω_i is assumed to be much larger than any other characteristic frequencies in the system, $\omega_i \gg \omega_{pe}, \Omega_e$, where ω_{pe} is the electron plasma frequency and Ω_e is the electron cyclotron frequency. The plasma is assumed to be optically thin, such that incident radiation is easily transmitted, each electron sees the same incident intensity, and no multiple scatterings occur. The laser power is required to not perturb the plasma, mainly through heating.

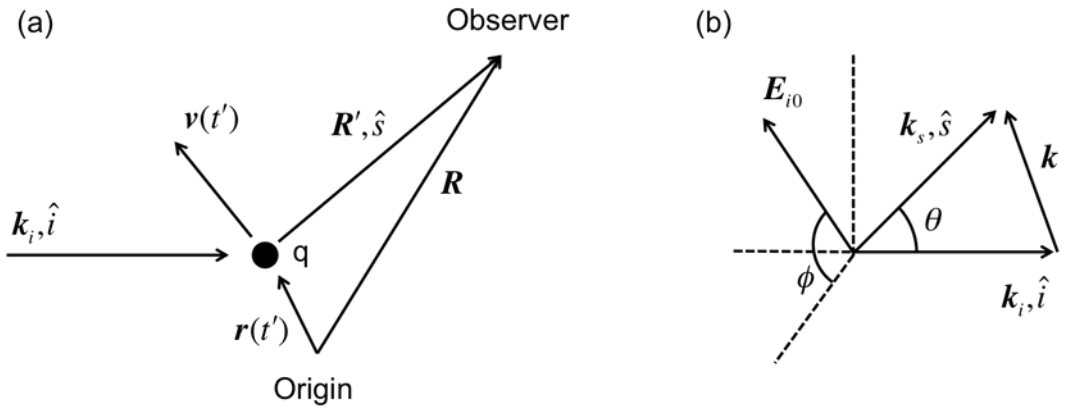

Figure 5.1: (a) Scattering geometry for wave incident along $\hat{i}$ on charge q and scattered along $\hat{s}$. (b) Scattering geometry showing scattering angle θ and incident polarization angle ϕ.

Only two-particle interactions are considered, such that the particle distribution functions can be linearized and written as an average term plus a fluctuating term, $f = f_0 + \tilde{f}_1$. This also allows the contributions from multiple electrons to be linearly superimposed. The plasma species are assumed to be in thermal equilibrium so that the distribution functions can be written as Maxwellians.

These conditions are readily satisfied in the work described here.

5.1.2 Scattering by a Single Charge

A monochromatic, linearly polarized electromagnetic wave given by

$$\boldsymbol{E_i}\left(\boldsymbol{r}, t'\right) = \boldsymbol{E_{i0}} \cos\left(\boldsymbol{k_i} \cdot \boldsymbol{r} - \omega_i t'\right) \qquad \boldsymbol{B_i}\left(\boldsymbol{r}, t'\right) = n\left(\hat{i} \times \boldsymbol{E_i}\right) \tag{5.1}$$

is incident upon a charge q, where $\boldsymbol{k_i}$ and ω_i are the incident wavenumber and frequency, respectively, and $\hat{i}$ is the unit vector pointing in the direction of the incident wave (see Fig. 5.1). The electric field of the wave causes the charge to accelerate (ignoring the effect of $\boldsymbol{B_i}$), which in turn causes the charge to radiate, *i.e.* scatter. The equation of motion of the charge is

$$m_e \frac{d\boldsymbol{v}}{dt'} = q\boldsymbol{E_i} \tag{5.2}$$

where the motion is evaluated at the retarded time $t' = t - R'/c$ and $\boldsymbol{R'}$ is the distance from the charge to the observer. Note, by the assumption that the observer is in the far field, $\boldsymbol{R'} \approx \boldsymbol{R}$, where $\boldsymbol{R}$ is the distance from the origin to the observer.

The resulting scattered electric and magnetic fields at a distance $\boldsymbol{R} \gg L$, where L is a characteristic length of the system, are [74]

$$\begin{aligned} \boldsymbol{E_s}(\boldsymbol{R}, t) &= \frac{q}{c^2}\left[\frac{\hat{s} \times ((\hat{s} - \boldsymbol{v}) \times \dot{\boldsymbol{v}})}{(1 - \hat{s} \cdot \boldsymbol{v})^3 R}\right]_{ret} \\ \boldsymbol{B_s}(\boldsymbol{R}, t) &= n(\hat{s} \times \boldsymbol{E}) \end{aligned} \tag{5.3}$$

where $\hat{s}$ is the unit vector pointing from the charge to the observer (see Fig. 5.1), $n = ck/\omega$ is the index of refraction, and the fields are evaluated at the retarded time.

From Eq. 5.2 and the assumption of non-relativistic motion, the scattered electric field can be written in terms of the incident wave as

$$\boldsymbol{E_s}(\boldsymbol{R}, t) = \frac{q^2}{m_e c^2 R}\left[\hat{s} \times (\hat{s} \times \boldsymbol{E_{i0}})\right] \cos(\boldsymbol{k_i} \cdot \boldsymbol{r} - \omega_i t') \tag{5.4}$$

After evaluating at the retarded time, $\boldsymbol{E_s}$ becomes

$$\boldsymbol{E_s}(\boldsymbol{R}, t) = \frac{q^2}{m_e c^2 R}\left[\hat{s} \times (\hat{s} \times \boldsymbol{E_{i0}})\right] \cos(k_s R - \omega_s t - \boldsymbol{k} \cdot \boldsymbol{r}(0)) \tag{5.5}$$

where $\boldsymbol{r}(0)$ is the position of the charge at $t = 0$ and

$$\omega_s = \omega_i \frac{\left(1 - \hat{i} \cdot \frac{\boldsymbol{v}}{c}\right)}{\left(1 - \hat{s} \cdot \frac{\boldsymbol{v}}{c}\right)} \tag{5.6}$$

$$\boldsymbol{k_s} = \frac{\omega_s}{c} \hat{s} \tag{5.7}$$

$$\omega \equiv \omega_s - \omega_i = \boldsymbol{k} \cdot \boldsymbol{v} \tag{5.8}$$

$$\boldsymbol{k} \equiv \boldsymbol{k_s} - \boldsymbol{k_i} \tag{5.9}$$

In other words, in response to the incident wave, the charge moving with velocity $\boldsymbol{v}$ radiates a Doppler-shifted wave at frequency ω_s and wavenumber $\boldsymbol{k_s}$. The Doppler shift is a result of two effects. The charge first sees the incident wave at a Doppler-shifted frequency $\omega' = \omega_i - \boldsymbol{k_i} \cdot \boldsymbol{v}$. A second shift then occurs because the charge moves relative to the observer, $\omega_s = \omega' + \boldsymbol{k_s} \cdot \boldsymbol{v}$. Note that Eqs. 5.8 and 5.9 are also statements of conservation of energy and momentum, respectively.

The scattered power per unit solid angle centered at position $\boldsymbol{R}$ is given by

$$\frac{dP_s}{d\Omega} = R^2 \boldsymbol{S} \cdot \hat{s} = \frac{R^2 c}{4\pi} E_s^2 \tag{5.10}$$

where $\boldsymbol{S} \equiv (c/4\pi)\boldsymbol{E} \times \boldsymbol{B}$ is the Poynting flux. Substituting Eq. 5.5 into Eq. 5.10, the time-averaged scattered power per unit solid angle is

$$\overline{P_s(\boldsymbol{R})} d\Omega = P_i Z^2 r_0^2 d\Omega \left[\hat{s} \times \left(\hat{s} \times \hat{E_{i0}}\right)\right]^2 \tag{5.11}$$

where $P_i = cE_{i0}^2/8\pi$ is the incident power and $r_0^2 = e^2/m_e c^2 = 2.82 \times 10^{-13}$ cm is the classical electron radius. It can be seen from the mass dependence in Eq. 5.11 that ions will not appreciably scatter. The angular dependence of the scattered power is given by the term in brackets, which for a linearly polarized incident wave reduces to (see Fig. 5.1)

$$\left[\hat{s} \times \left(\hat{s} \times \hat{E_{i0}}\right)\right]^2 = 1 - \sin^2\theta \cos^2\phi \tag{5.12}$$

Note that the total scattering cross section $\int P_s d\Omega / P_i = (8\pi/3) r_0^2 = \sigma_T = 6.65 \times 10^{-25}$ cm^2 is just the Thomson cross section.

5.1.3 Scattering by Multiple Electrons

Now consider the scattering of incident radiation by N electrons and N/Z ions with charge Ze in a volume V (recall, though, that the ions do not appreciably scatter). The total scattered electric field is just the vector sum of the individual scattered fields, *i.e.*

$$\boldsymbol{E_s^T}(\boldsymbol{R}, t) = \sum_{n=1}^{N} \boldsymbol{E_{s,n}}(\boldsymbol{R}, t) \tag{5.13}$$

where each $\boldsymbol{E_{s,n}}$ has a form like Eq. 5.5. In other words, the individual scattered fields are identical up to a phase that depends on the individual electron's motion. The total scattered power, in turn, goes like

$$\frac{dP_s}{d\Omega} \propto \left|\boldsymbol{E_s^T}\right|^2 = \sum_{n=1}^{N} \boldsymbol{E_{s,n}} \cdot \sum_{m=1}^{N} \boldsymbol{E_{s,m}^*} \tag{5.14}$$

If the electrons are all randomly distributed, then on average the phases of the scattered fields will cancel and the total scattered power will just reflect the sum of the individual motions, *i.e* the velocity distribution of the electrons. This is incoherent or non-collective scattering and is represented by the $n = m$ terms in Eq. 5.14. If instead the motions of the electrons (and scattered waves) are correlated, then the cross terms ($n \neq m$) in Eq. 5.14 become important and the scattered power will reflect both individual and wave motions. This is coherent or collective scattering.

The effect of multiple electrons' motions on the scattered power is represented by the spectral density function $S(\boldsymbol{k}, \omega) d\omega_s$, which is the probability that the frequency shift of a scattered photon lies within the range $d\omega_s$ around ω. In terms of $S(\boldsymbol{k}, \omega)$, the total scattered power in a solid angle $d\Omega$ in the frequency range $w_s \rightarrow \omega_s + d\omega_s$ can be written

$$\overline{P_s\left(\boldsymbol{R},\omega_s\right)}d\Omega d\omega_s = \frac{P_i r_0^2}{2\pi A} d\Omega d\omega_s \left|\hat{s}\times\left(\hat{s}\times\hat{E_{i0}}\right)\right|^2 NS(\boldsymbol{k},\omega) \tag{5.15}$$

$S(\boldsymbol{k},\omega)$ can be evaluated by looking at the evolution of the charged-particle distribution function $F_q(\boldsymbol{r},\boldsymbol{v},t)$, which satisfies the Klimontovich equation and Maxwell's equations. To get a closed system of equations, F_q is linearized, *i.e.* $F_q \approx F_{q,0} + \tilde{F}_{q,1}$, where $F_{q,0}$ is the ensemble-average and $\tilde{F}_{q,1}$ are the fluctuations about this average. Note that the ensemble-average is related to the single-particle velocity distribution function: $F_{q,0} = n_{q,0} f_{q,0}(\boldsymbol{v})$, where $n_{q,0}$ is the mean density, *i.e.* $n_q \approx n_{q,0} + \tilde{n}_{q,1}$.

It can then be shown [74] that $S(\boldsymbol{k},\omega)$ has the form

$$S\left(\boldsymbol{k},\omega\right) = \frac{2\pi}{k}\left|1-\frac{\chi_e}{\epsilon}\right|^2 f_{e,0}(w/k) + \frac{2\pi Z}{k}\left|\frac{\chi_e}{\epsilon}\right|^2 f_{i,0}(w/k) \tag{5.16}$$

where

$$\chi_e\left(\boldsymbol{k},\omega\right) \equiv \frac{4\pi e^2 n_{e,0}}{m_e k^2}\int_{-\infty}^{\infty} d\boldsymbol{v}\frac{\boldsymbol{k}\cdot\frac{\partial f_{e,0}}{\partial \boldsymbol{v}}}{\omega-\boldsymbol{k}\cdot\boldsymbol{v}-i\gamma} \tag{5.17}$$

$$\chi_i\left(\boldsymbol{k},\omega\right) \equiv \frac{4\pi Z^2 e^2 n_{i,0}}{m_i k^2}\int_{-\infty}^{\infty} d\boldsymbol{v}\frac{\boldsymbol{k}\cdot\frac{\partial f_{i,0}}{\partial \boldsymbol{v}}}{\omega-\boldsymbol{k}\cdot\boldsymbol{v}-i\gamma} \tag{5.18}$$

$$\epsilon(\boldsymbol{k},\omega) = 1 + \chi_e(\boldsymbol{k},\omega) + \chi_i(\boldsymbol{k},\omega) \tag{5.19}$$

χ_e and χ_i are the electron and ion susceptibilities, respectively, and are components of the dielectric function ϵ. It can be seen in Eq. 5.16 that the total scattered spectrum is the sum of an electron scattered spectrum (the first term) and an ion scattered spectrum (the second term). The electron term is due to the response of free electrons, *i.e.* electrons that follow unperturbed orbits, and perturbed electrons due to electron correlations. The ion term is due to the response of electrons as they try to shield ions.

To proceed, particular distribution functions $f_{e,0}$ and $f_{i,0}$ must be chosen.

5.1.4 Plasmas with a Maxwellian Distribution Function

For the purpose of this work, the particles are assumed to be in thermal equilibrium and represented by Maxwellian distribution functions (see section 5.1.1). Since Thomson scattering only probes along $\boldsymbol{k}$, it is inherently a one-dimensional measurement, and so the one-dimensional Maxwellian velocity distribution function is used:

$$f_{q,0}(v) = \left(\frac{1}{\pi v_{Tq}^2}\right)^{1/2} \exp\left(-\frac{v^2}{v_{Tq}^2}\right) \tag{5.20}$$

where $v_{Tq} = \sqrt{2\kappa_B T_q/m_e}$ is the thermal speed. Using the definitions

$$x_e \equiv \frac{\omega}{k v_{Te}} \qquad x_i \equiv \frac{\omega}{k v_{Ti}} \qquad \alpha \equiv \frac{1}{k\lambda_{De}} \tag{5.21}$$

where λ_{De} is the Debye length, and substituting Eq. 5.20 into Eqs. 5.17 and 5.18, the susceptibilities can be written

$$\begin{aligned}
\chi_e(\boldsymbol{k},\omega) &= -\frac{\alpha^2}{2}\frac{\partial}{\partial x_e}W(x_e) = \alpha^2\left[RW(x_e) + iIW(x_e)\right] \\
\chi_i(\boldsymbol{k},\omega) &= -\frac{\alpha^2}{2}\frac{ZT_e}{T_i}\frac{\partial}{\partial x_i}W(x_i) = \alpha^2\frac{ZT_e}{T_i}\left[RW(x_i) + iIW(x_i)\right] \\
W(x_q) &= \left(\frac{1}{\pi}\right)^{1/2}\int_{-\infty}^{\infty} dz \frac{\exp(-z^2)}{z - x_q}
\end{aligned} \tag{5.22}$$

where $RW(x_q)$ and $IW(x_q)$ are the real and imaginary parts, respectively, of the plasma dispersion function $W(x_q)$. The spectral density function then becomes

$$\begin{aligned}
S(\boldsymbol{k},\omega) &= \frac{2\pi^{1/2}}{k v_{Te}}\left|\frac{1+\chi_i}{\epsilon}\right|^2 \exp\left(-x_e^2\right) + \frac{2\pi^{1/2}Z}{k v_{Ti}}\left|\frac{\chi_e}{\epsilon}\right|^2 \exp\left(-x_i^2\right) \\
&= \frac{2\pi^{1/2}}{k v_{Te}}\left[\frac{A_e}{|\epsilon|^2} + \frac{A_i}{|\epsilon|^2}\right]
\end{aligned} \tag{5.23}$$

where

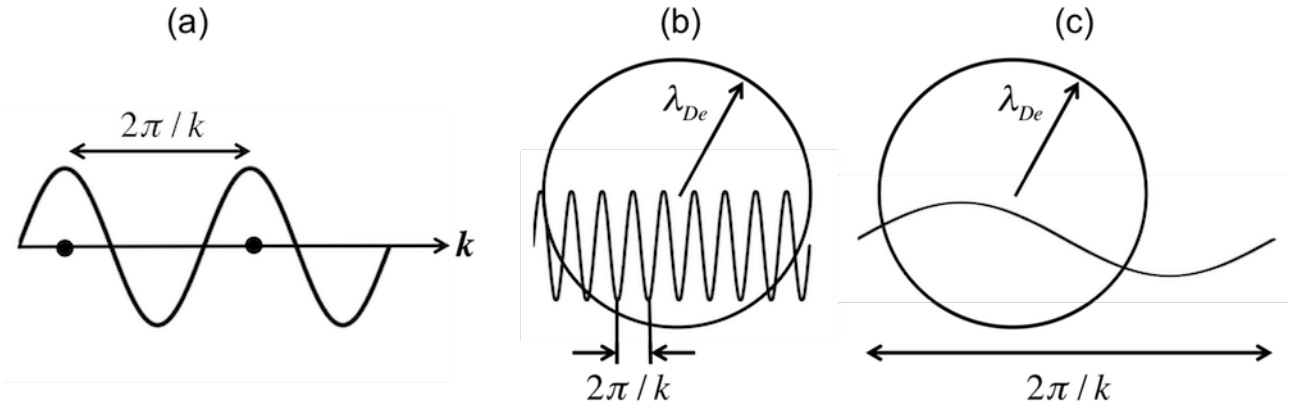

Figure 5.2: (a) Waves that are scattered by electrons separated by a distance $2\pi/k$ along $\boldsymbol{k}$ are in phase. (b) Non-collective scattering, $\alpha \ll 1$. (c) Collective scattering, $\alpha \gtrsim 1$. Adapted from [83].

$$
\begin{aligned}
A_e &= \exp\left(-x_e^2\right)\left[\left(1+\alpha^2\frac{ZT_e}{T_i}RW(x_i)\right)^2+\left(\alpha^2\frac{ZT_e}{T_i}IW(x_i)\right)^2\right] \\
A_i &= Z\left(\frac{m_iT_e}{m_eT_i}\right)^{1/2}\exp\left(-x_i^2\right)\alpha^4\left[(RW(x_e))^2+(IW(x_e))^2\right] \\
|\epsilon|^2 &= \left[1+\alpha^2\left(RW(x_e)+\frac{ZT_e}{T_i}RW(x_i)\right)\right]^2+\alpha^4\left[IW(x_e)+\frac{ZT_e}{T_i}IW(x_i)\right]^2
\end{aligned}
\tag{5.24}
$$

It can be seen from Eq. 5.23 and 5.24 that α controls the relative contribution of the electron and ion terms. For example, for $\alpha \ll 1$, $S(\boldsymbol{k},\omega)$ is just proportional to the incoherent electron distribution (see section 5.1.5), while for $\alpha \gg 1$, long-range correlations come into play. Thus α is a measure of how collective the scattered power is, and is, appropriately, termed the scattering parameter. To understand why, recall that the phase of the scattered waves depend on $\boldsymbol{k}\cdot\boldsymbol{r}(0)$ (see Eq. 5.5), so that electrons separated by a distance $2\pi/k$ along $\boldsymbol{k}$ are in phase. If electrons are randomly distributed within this distance, then the phases of their scattered waves will also be random and the scattered power will be non-collective. Conversely, if the electron positions are correlated over this length, then they will coherently scatter. Thus, $2\pi/k$ is a characteristic scale over which the behavior of the electrons (in particular, the density fluctuations) are sampled. Recall also that

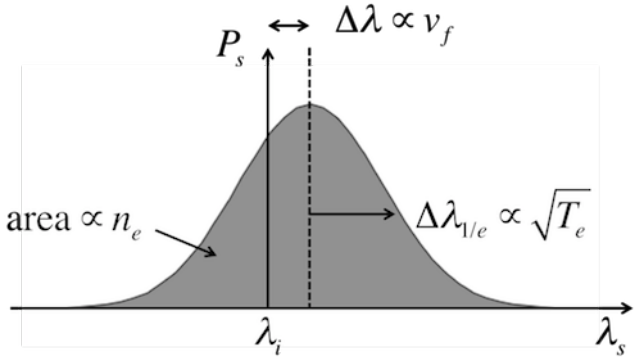

Figure 5.3: Diagram of a non-collective Thomson scattering spectrum with Maxwellian electron velocity distribution. The area and width of the spectrum are proportional to the electron density n_e and temperature $\sqrt{T_e}$, respectively. The shift of the spectrum relative to λ_i is proportional to the fluid speed v_f.

$$\alpha = \frac{1}{k\lambda_{De}} \approx \frac{e\lambda_i}{\sin(\theta/2)} \left(\frac{\pi n_{e,0}}{\kappa_B T_e}\right)^{1/2} \tag{5.25}$$

where λ_i is the incident wavelength and the non-relativistic approximation $|k| = 2|k_i| \sin\theta/2$ has been used. Since electrons within a Debye sphere are uncorrelated *i.e.* randomly distributed, if $2\pi/k$ is small compared to λ_{De}, then a random population of electrons are sampled and the scattering is incoherent. If instead $2\pi/k > \lambda_{De}$, then long-range correlations between electrons are probed and the scattering can be coherent. Since the motions of electrons over longer scales necessarily are affected by ions, coherent scattering will reflect both electron and ion velocity distributions, as seen in Eq. 5.16. The scattering parameter, then, just characterizes what scale length relative to λ_{De} is being probed (see Fig. 5.2). For $\alpha \ll 1$, the scattering is non-collective, while for $\alpha \gtrsim 1$ the scattering is collective.

Note, from Eq. 5.25, that α can take a range of values for fixed plasma parameters (through θ) or fixed geometry (through plasma parameters). Thus, it is possible to probe collective behavior in any plasma.

5.1.5 Non-Collective Thomson Scattering

For a Maxwellian electron distribution function in the non-collective regime ($\alpha \ll 1$, see section 5.1.4), the total scattered power in a solid angle $d\Omega$ in the frequency range $w_s \rightarrow \omega_s + d\omega_s$ reduces to

$$\overline{P_s\left(\boldsymbol{R},\omega_s\right)}d\Omega d\omega_s = \frac{P_i r_0^2 N}{A} d\Omega d\omega_s \left|\hat{s}\times\left(\hat{s}\times\hat{E_{i0}}\right)\right|^2 \frac{\exp[-\left(\omega/kv_{Te}\right)^2]}{\pi^{1/2}kv_{Te}} \tag{5.26}$$

Thus, the scattered spectrum just reflects the Maxwellian distribution of the electrons, *i.e.* the spectrum shape is a Gaussian (see Fig. 5.3). Consequently, the electron temperature can be directly obtained from the shape of the spectrum using

$$T_e = \frac{m_e c^2}{8\kappa_B}\left(\frac{\Delta\lambda_{1/e}}{\lambda_i \sin\theta/2}\right)^2 \tag{5.27}$$

where $\Delta\lambda_{1/e}$ is the spectral (e^{-1}) half-width.

If the plasma has a fluid speed $\boldsymbol{v_f}$, it will appear as an additional frequency shift in the scattered spectrum according to $\omega_{c,f} - \omega_i = \boldsymbol{k}\cdot\boldsymbol{v_f}$, where $\omega_{c,f}$ is the observed central frequency of the scattered spectrum (*e.g.* for a Gaussian, the peak frequency). If the electrons have a drift $\boldsymbol{v_D}$ relative to the ions, there is a further frequency shift of $\omega/k \rightarrow \omega/k - v_D/\cos\gamma$, where γ is the angle between $\boldsymbol{k}$ and $\boldsymbol{v_D}$. Note that this frequency shift will only affect the electron scattered spectrum, and so is indistinguishable from a fluid drift in the non-collective regime.

5.1.6 Collective Thomson Scattering

In the collective regime ($\alpha \gtrsim 1$), the full spectral density function must be used and the total scattered power is given by Eqs. 5.15 and 5.23. While the shape of the scattered spectrum will depend heavily on α, it nonetheless has some general features (see Fig. 5.4). Recall that the total scattered spectrum is just the sum of the electron and ion scattered spectrums, and that each term in the spectral density function depends on the dielectric function ϵ.

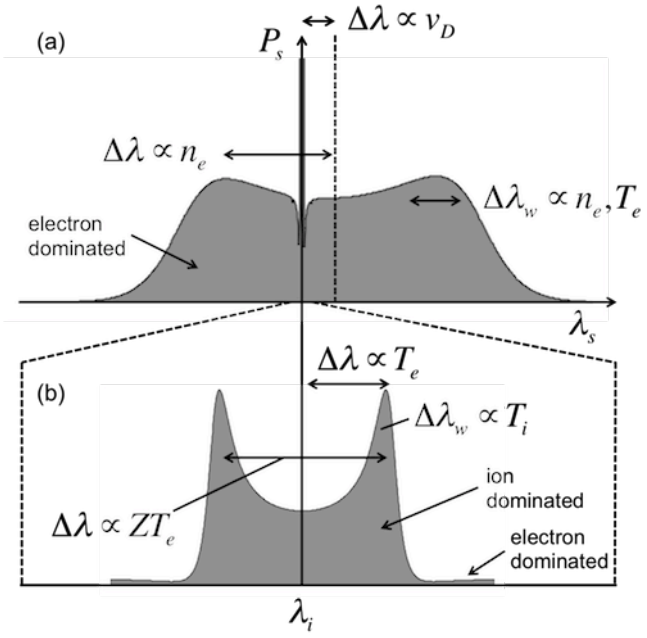

Figure 5.4: Diagram of a collective Thomson scattering spectrum ($\alpha \sim 1$) with Maxwellian electron velocity distribution. (a) Electron feature. (b) Ion feature. For both features, the separation of the peaks is proportional to the wavelength of the corresponding wave (λ_{pe} or λ_{ac}). The amplitude and widths of the peaks are related to parameters of the corresponding Landau damping.

Consequently, the scattered spectrum will have natural resonances when $|\epsilon|^2$ is small, *i.e.* at the electron plasma ω_{pe} and ion-acoustic ω_{ac} frequencies.

At low α, the electron scattered spectrum (electron feature) corresponds to the thermal motions of electrons and is thus Gaussian in shape (see section 5.1.5). As α increases, the probing frequency ω approaches ω_{pe}, and peaks corresponding to forward and reverse traveling electron plasma waves appear (see Fig. 5.4a). Since these peaks are at $\omega_{pe} \propto \sqrt{n_e}$, their shift relative to ω_i can be used to extract the electron density n_e. The amplitude and width of the peaks are governed by the damping of the waves, which for Landau damping depends on n_e and temperature T_e. Additionally, if there's a relative electron-ion drift, the peaks will be shifted accordingly (see section 5.1.5).

Due to the strong damping of ion-acoustic waves, the ion feature is only appreciable

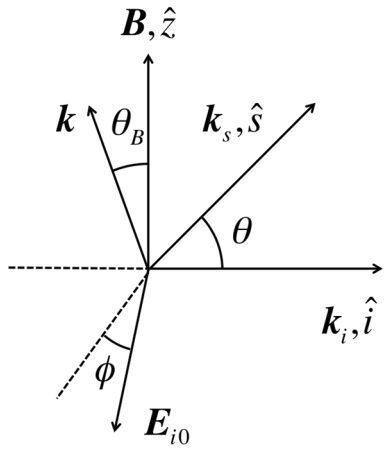

Figure 5.5: Scattering geometry in a magnetic field $\boldsymbol{B}$ at an angle θ_B relative to $\boldsymbol{k}$.

in the collective regime, though within this regime it is generally much more intense than the electron feature. Similar to the electron feature, peaks corresponding to forward and reverse traveling ion-acoustic waves will appear in the ion feature as the probe frequency ω approaches ω_{ac} (see Fig. 5.4b). From the frequency separation and width of the peaks, the ion temperature T_i and ZT_e can be determined. If T_e is know, the charge state Z can also be determined (and vice versa). If there are multiple ion species in the plasma, resonant peaks for each species will appear and uniquely depend on ZT_e/T_i.

Finally, as described in section 5.1.5, a plasma fluid drift will result in a frequency shift of the entire spectrum (electron and ion features).

5.1.7 Thomson Scattering in a Magnetic Field

Since many of the experiments presented in this work take place in a static magnetic field B, it is relevant to study the effect B has on the scattered power. The addition of an external magnetic field will cause the particles to gyrate, which will affect the particle distributions in the spectral density function $S(\boldsymbol{k}, \omega)$. It is reasonable to expect the electron Ω_e and ion Ω_i cyclotron frequencies to appear in the dielectric function, and hence for new resonances to appear in the scattered spectra.

For simplicity, ions will be assumed to be unmagnetized, though for most of the ex-

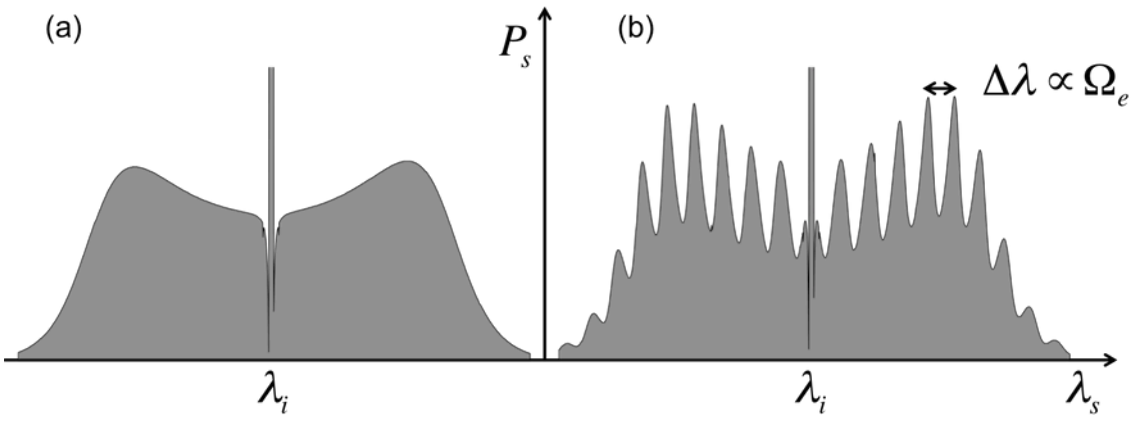

Figure 5.6: Diagram of a collective Thomson scattering spectrum in a magnetic field. (a) Electron feature with $B = 0$ or $\theta_B = 0$. (b) Electron feature with $B \neq 0$ and $\theta_B \sim 90°$. The spacing of the modulations is proportional to the electron cyclotron frequency Ω_e.

periments in this work, this assumption is justified. Maxwellian distribution functions will continue to be assumed. It can then be shown [74] that

$$\begin{aligned} S\left(\boldsymbol{k},\omega\right) &= \frac{2\pi^{1/2}}{k_{\parallel}v_{Te}}\left|\frac{1+\chi_i}{\epsilon_m}\right|^2 \sum_n \exp\left[-k_{\perp}^2\eta_e^2\right] I_n\left[k_{\perp}^2\eta_e^2\right] \exp\left(-x_{en}^2\right) \\ &\quad + \frac{2\pi^{1/2}Z}{kv_{Ti}}\left|\frac{H_e}{\epsilon_m}\right|^2 \exp\left(-x_i^2\right) \\ \epsilon_m &= 1 + H_e + \chi_i \end{aligned} \tag{5.28}$$

where $\eta_e = v_{Te}/\sqrt{2}\Omega_e$, $x_{en} = (\omega - n\Omega_e)/k_{\parallel}v_{Te}$, $k_{\parallel} = k\cos\theta_B$, $k_{\perp} = k\sin\theta_B$, θ_B is the angle between $\boldsymbol{B}$ and $\boldsymbol{k}$, and I_n is the modified Bessel function of the first kind (see Fig. 5.5). The magnetic electron susceptibility H_e is given by

$$
\begin{aligned}
H_e\left(\boldsymbol{k},\omega\right) &= \alpha^2\left[1-\sum_n \exp\left(-k_\perp^2\eta_e^2\right) I_n\left(k_\perp^2\eta_e^2\right)\left(\frac{\omega}{\omega-n\Omega_e}\right)\right], k_\parallel = 0 \\
H_e\left(\boldsymbol{k},\omega\right) &= \alpha^2 - \alpha^2\sum_n \exp\left(-k_\perp^2\eta_e^2\right) I_n\left(k_\perp^2\eta_e^2\right)\left(\frac{\omega}{\omega-n\Omega_e}\right) \\
&\quad\times\left[2x_{en}\exp\left(-x_{en}^2\right)\int_0^{x_{en}}\exp\left(z^2\right)dz + i\pi^{1/2}x_{en}\exp\left(-x_{en}^2\right)\right], k_\parallel \neq 0
\end{aligned}
\tag{5.29}
$$

Note that the term in brackets for the $k_\parallel \neq 0$ case is essentially the plasma dispersion function.

It can be seen from Eq. 5.28 and Fig. 5.6 that the addition of a magnetic field introduces damped modulated satellite peaks at the cyclotron frequencies into the scattered spectrum (compare to Eq. 5.23). For $\alpha \ll 1$ or $k_\perp\eta_e \gg 1$ ($B \to 0$), $S(\boldsymbol{k},\omega)$ reduces to the non-magnetic, non-collective case (see section 5.1.5). For $\theta_B \to 0$, $S(\boldsymbol{k},\omega)$ reduces to the unmagnetized case (Eq. 5.16). For $B \neq 0$ but small ($\Omega_e/kv_{Te} \ll \cos\theta_B$), the modulation is largely washed out and can be ignored [42]. This is the case in all experiments detailed in this work.

5.1.8 Rayleigh Scattering

Rayleigh scattering is the elastic scattering of electromagnetic radiation by neutral atoms, specifically the electron cloud around ions. Functionally, it can be treated similarly to the ion feature in Thomson scattering. Like the Thomson ion feature, the Rayleigh spectrum is very narrow due to slow ions with small Doppler shifts. Unlike Thomson scattering, the correlation length for atoms is typically much larger than the sampling length $2\pi/k$, so that Rayleigh scattering is incoherent.

As discussed in [83], the Rayleigh scattering cross section goes like

$$
\frac{d\sigma_R}{d\Omega} = \frac{4\pi^2}{\lambda_i^4}\left(\frac{\mu-1}{n_\mu}\right)^2\left(1-\sin^2\theta\cos^2\phi\right) \tag{5.30}
$$

Particle	$d\sigma_R/d\Omega$ (10^{-32} m^2)	σ_{th}/σ_R
Ar	5.40	–
Ar^+	2.12	–
H	–	1769
He	0.087	–
N_2	6.07	380
O_2	4.99	462
Dry Air	–	401

Table 5.1: Common values for the differential Rayleigh scattering cross section $d\sigma_R/d\Omega$ given by [83] for $\lambda_i = 532$ nm and $\theta = \phi = 90°$. Also listed are the Thomson-to-Rayleigh cross section ratios σ_{th}/σ_R given by [17].

where n_μ is the gas density at which the index of refraction μ is measured. Common values are listed in Table 5.1.

For the purposes of this work, Rayleigh scattering is primarily useful as a density calibration mechanism for non-collective Thomson scattering [73, 52]. For both non-collective Thomson and Rayleigh scattering, the collected scattered signal W can be written

$$W_a = \frac{I_a}{h\nu_i} \cdot \tau_i \cdot n_a \cdot \Delta V \cdot \sigma_f \cdot \Delta\Omega \cdot f_{system} \tag{5.31}$$

where I is the laser intensity, h is Plank's constant, ν_i is the laser frequency, τ_i is the laser pulse length, n is the density, σ is the scattering cross section, f_{system} is a characterization of the collection efficiency, and the subscript a corresponds to Thomson (th) or Rayleigh (R) parameters. Therefore, by taking the ratio of the Thomson and Rayleigh scattered powers, the experimental parameters (ΔV, $\Delta\Omega$, f_{system}) drop out and the electron density can be obtained by

$$n_e = n_g \left(\frac{W_{th}}{W_R}\right)\left(\frac{L_R}{L_{th}}\right)\left(\frac{\sigma_R}{\sigma_{th}}\right) \tag{5.32}$$

where n_g is the Rayleigh gas density and L is the laser energy. The collected signal W is the total integrated intensity of the signal. For Gaussian spectrums, this reduces to: $W = \sqrt{2\pi}\, W_{peak}\, \Delta\lambda$, where W_{peak} is the peak signal intensity and $\Delta\lambda$ is the standard deviation. The Rayleigh gas density can be calculated from the ideal gas law: $n_g[\mathrm{cm}^{-3}] = 9.66 \times 10^{18}\, P[\mathrm{Torr}]\, T^{-1}[\mathrm{K}]$.

5.2 Diagnostic Considerations

The main difficulty in any Thomson scattering setup is the paucity of scattered photons due to the extremely small scattering cross section ($\sigma_T = 6.65 \times 10^{-25}$ cm^2). Since there is so little signal to begin with, additional effects like photon noise, plasma noise, or laser stray-light can overwhelm the desired signal. This section examines common sources of unwanted signal, their effect on the scattered spectrum, and where possible, ways to mitigate them.

5.2.1 Signal-to-Noise Ratio

The total number of photons N_p^T scattered into a solid angle $\Delta\Omega$ can be estimated from the total scattered power P_s derived in section 5.1:

$$\begin{aligned} N_p^T \approx \frac{P_s \tau_L \Delta\Omega}{h\nu_i} &= \frac{\tau_L}{2\pi h\nu_i} \cdot I_L \cdot n_e \cdot \Delta V \cdot \sigma_T \cdot \Delta\Omega \cdot \int_{-\infty}^{+\infty} S\left(\boldsymbol{k}, \omega\right) d\omega_s \\ &\overset{ncol}{=} \frac{\tau_L}{h\nu_i} \cdot I_L \cdot \Delta V \cdot n_e \cdot \sigma_T \cdot \Delta\Omega \end{aligned} \tag{5.33}$$

where τ_L is probe laser pulse length, ν_i is the frequency of the laser[1], h is Plank's constant,

[1]Technically, the collection time τ_s and scattered photon frequency ν_s should be used. However, generally $\tau_s \approx \tau_l$ and $\nu_s \approx \nu_i$

I_L is the intensity of the laser, ΔV is the scattering volume, n_e is the electron density, σ_T is the Thomson cross section, and the last equality is taken in the non-collective limit.

Not all of the photons scattered will make it through the collection system (due to losses in optics, the spectrometer, *etc.*) and be detected. Let μ be the efficiency of the collection system, so that the number of photons that make it through the collection system is $N_p = N_p^T \mu$. Additionally, photons that make it to the detector are generally spread over multiple detector channels: $N_{pc} = N_p/C$, where C is the number of channels (*e.g.* pixels in an CCD). Note, the scattered signal is assumed here to be evenly distributed across all detector channels, though in general this is not the case. Finally, photons are converted by the detector photocathode to photo-electrons with efficiency η and then to signal counts with gain g. Additional effects, like the noise in the detector's multi-channel plate (MCP) or readout noise, are ignored, though the reader is encouraged to study [83] for a more comprehensive overview.

Due to the small number of photons involved, the distribution of photo-electrons per channel in the CCD can be well described by a Poisson distribution and Poisson statistics. The number of photo-electrons per channel N_{pec} detected is then

$$N_{pec} = \frac{N_p^T \, \mu \, \eta \, g}{C} \pm \left(\frac{N_p^T \, \mu \, \eta \, g}{C} \right)^{1/2} \tag{5.34}$$

with a signal-to-noise ratio

$$S/N = \frac{N_{pec}}{(N_{pec})^{1/2}} = (N_{pec})^{1/2} \tag{5.35}$$

Background emission, predominately from stray-light (see section 5.2.2) but also from bremsstrahlung and line radiation, will also contribute scattered photons to the total signal. However, these sources are generally constant and independent of Thomson scattering, so their signals can be subtracted using a non-Thomson spectrum. Thus, only their photon noise contributes to the signal-to-noise ratio. Let N_{bec} be the number of photo-electrons per

channel generated by background emission with standard deviation $(N_{bec})^{1/2}$. The signal-to-noise ratio then becomes

$$S/N = \frac{N_{pec}}{(N_{pec} + N_{bec})^{1/2}} \tag{5.36}$$

Typical parameters for the experiments in this work are: $\tau_L = 5$ ns, $\lambda_i = c/\nu_i = 532$ nm, $I_L = 10^{11}$ W/cm^2, $\Delta V = 0.5$ mm^3, $N_e = 10^{15}$ cm^{-3}, $\Delta\Omega = 0.01$ sr, $\mu = 0.5$, $\nu = 0.3$, $g = 1$, $C = 512$, and $N_{bec} \sim 10^4$. These parameters then yield: $N_p^T \sim 5.5 \times 10^6$, $N_{pec} \sim (1.6 \pm 0.04) \times 10^3$, and $S/N \sim 15$. For $N_e = 10^{13}$ cm^{-3}, the values are: $N_p^T \sim 5.5 \times 10^4$, $N_{pec} \sim (1.6 \pm 0.4) \times 10^1$, and $S/N \sim 0.16$. Since these are single-shot measurements, $S/N < 1$ is essentially undetectable. To get $S/N \geq 3$ at $N_e \sim 10^{13}$ cm^{-3}, it is necessary for $N_{bec} \lesssim 10$, *i.e.* the background emission must be effectively eliminated. In other words, at these parameters, the lowest density that can be detected under ideal conditions in a single measurement is $N_e \sim 10^{13}$ cm^{-3}.

5.2.2 Stray-Light

Stray-light generally refers to unwanted scattered light from the probe laser. Since the probe laser has to terminate somewhere, it will inevitably interact with components of the experiment (*e.g.* vacuum chamber) and scatter. This scattering tends to be isotropic and specular, making it difficult to shield the collection optics. Because it is at the laser wavelength, stray-light is difficult to filter without affecting the desired spectrum. Furthermore, since it primarily exists during the laser pulse, stray-light cannot be limited by reducing the collecting time without also reducing the desired signal.

There are many ways to mitigate stray-light effects – see for example [83] and [21]. In the ideal case, stray-light is prevented from ever reaching the collection optics by limiting the interaction of the probe laser with other components. In the experiments presented in this work, this is often done by terminating the laser in a highly absorptive beam dump or by terminating the laser far from the collection volume (so that it can be temporally filtered).

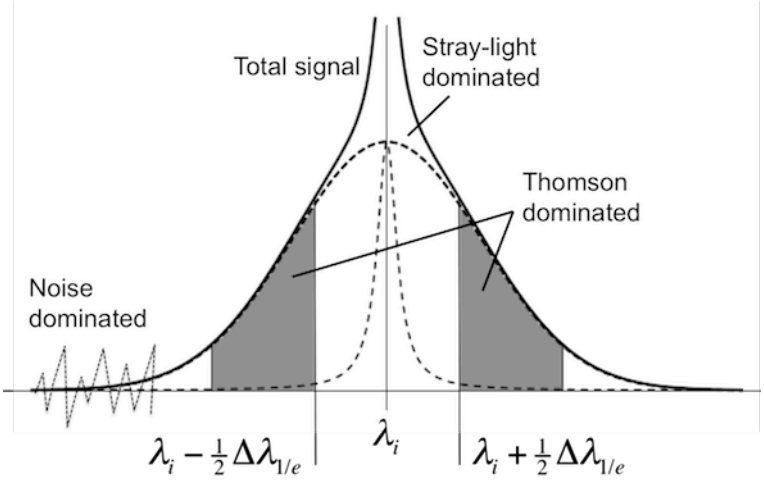

Figure 5.7: Schematic spectrum with Thomson and stray-light signals. The stray-light tends to dominate the spectrum near the laser wavelength λ_i, while noise dominates in the far wings. Adapted from [83].

Baffles, masks, and viewing dumps were also added to the collection setup. The baffles and masks act like apertures that limit the field of view of the collection optics, thereby limiting the effect of stray-light. Viewing dumps provide a dark background so that highly reflective objects, such as a chamber wall, aren't projected back to the detector. Filters were also used to try and block the stray-light directly, both before the spectrometer with a notch filter, and between the spectrometer and detector with a physical mask that blocked a range of diffracted wavelengths. In both cases, the filters tended to remove too much of the spectrum to be helpful.

The problem with stray-light that makes it to the spectrometer is that it is redistributed (broadened) due to the spectrometer's instrument function. This shifts unwanted signal into the lower-intensity wings of the Thomson spectrum, reducing the effective spectrum that can be used to infer the spectral density function (*i.e.* the shape of the scattered signal, see Fig. 5.7). How important this effect is depends on both the intensity of the stray-light and the width of the Thomson spectrum. Higher intensity stray-light will have a larger redistribution, requiring a broader Thomson spectrum in order to have sufficient signal in the wings of the spectrum to accurately reconstruct the shape. Subtracting a stray-light

only spectrum will remove most of the unwanted signal, but it will also remove parts of desired signal – if no Thomson signal exists outside of the redistributed stray-light, then it is essentially unrecoverable. An effective rule of thumb [83] is that the stray-light intensity should be less than the Thomson intensity at half the e^{-1} half width $\frac{1}{2}\Delta\lambda_{1/e}$ of the Thomson spectrum (see Fig. 5.7). Fortunately, in most of the cases presented in this work, this condition is satisfied and the stray-light can be safely subtracted.

The stray-light is broadened due to the finite-width of the entrance slit, the finite diffraction pattern of the grating, and image aberrations in the spectrometer optics. These effects can be represented as a convolution of a delta function (monochromatic stray-light) with the spectrometer instrument function, which just yields the instrument function. The instrument function is itself a convolution of a boxcar function (slit), Lorentzian function (grating), and Gaussian function (aberrations), though this last contribution is much smaller than the others and will be subsequently ignored. The instrument function Γ is then given by

$$\Gamma(x) = \Pi(x) * \Lambda(x) = \int_{-\infty}^{+\infty} \Pi(y)\, \Lambda(x-y)\, dy \tag{5.37}$$

where

$$\begin{aligned} \Pi(x) &= \frac{\Theta\left(x+\frac{c}{2}\right) - \Theta\left(x-\frac{c}{2}\right)}{c} \\ \Lambda(x) &= \frac{1}{\pi}\frac{b}{x^2+b^2} \end{aligned} \tag{5.38}$$

are the normalized boxcar $\Pi(x)$ and Lorentzian $\Lambda(x)$ functions, $\Theta(x)$ is the Heaviside function, and b and c are width parameters. Substituting Eq. 5.38 into Eq. 5.37 and evaluating the convolution yields

$$\Gamma(x) = \frac{1}{\pi c}\left[\arctan\left(\frac{x+\frac{c}{2}}{b}\right) - \arctan\left(\frac{x-\frac{c}{2}}{b}\right)\right] \tag{5.39}$$

Properties of Γ include:

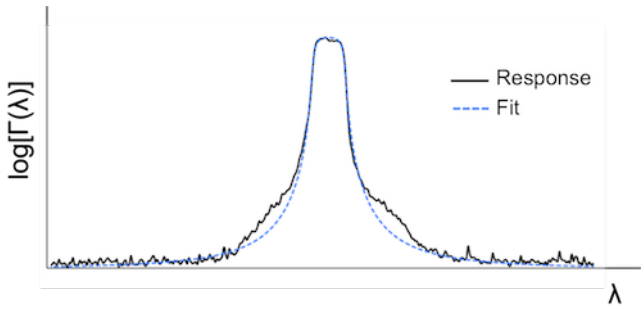

Figure 5.8: Example instrument response (solid) to a monochromatic source with instrument function fit $\Gamma(\lambda)$ (dashed). The broad flat portion is due to the finite slit size, while the wings are due to the finite diffraction pattern of the grating.

- $\int_{-\infty}^{+\infty} \Gamma(x)dx = 1$
- Maximum value $\Gamma(0) = 2\arctan\left(\frac{c}{2b}\right)$
- Halfwidth at half maximum $x_h = \pm\frac{1}{2}\sqrt{4b^2 + c^2}$

An example of the instrument function is shown in Fig. 5.8.

5.2.3 Effect of Laser on Plasma

Since the intense electric fields of a laser can heat electrons in a plasma, it is necessary to gauge the importance of this effect. Heating can take place through inverse bremmstrahlung, in which a photon is absorbed by an electron. The resulting change in temperature is estimated in [41], where it is assumed the laser pulse length is long enough to heat electrons but less than the electron-ion collision time, so that energy is not transferred to ions. It is also assumed that the energy gained by an electron is much less than the energy of a laser photon (this is readily satisfied in this work). The change in temperature T_e is then approximated as

$$\frac{\Delta T_e}{T_e} \approx 3.9 \times 10^{-12} \frac{n_i Z^2 \lambda_i^3}{T_e^{3/2}} \left[1 - \exp\left(\frac{h\nu_i}{T_e\,[\mathrm{J}]}\right)\right] Q_i \tag{5.40}$$

where n_i is the ion density with charge state Z, $\nu_i = c/\lambda_i$ is the laser frequency, h is Planck's constant, $Q_i = E_L/A$ is the laser energy per area, T_e is in eV unless otherwise noted, and all other units are in mks. Typical parameters for this work are: $n_i = 10^{21}$ m^{-3}, $Z = 3$, $\lambda_i = 532$ nm, $T_e = 5$ eV, $E_L = 10$ J, and $A = 3 \times 10^{-8}$ m^2. The resulting estimated heating is then $\Delta T_e \approx 0.3$ eV, which is generally less than the measurement accuracy. In most cases, then, plasma heating by the laser can be neglected.

5.3 Diagnostic Development

Much effort went into the development of a Thomson scattering diagnostic that could be deployed on the laser-ablated and ambient plasmas used to generate collisionless shocks. This section details the major components of that development and relevant results. These include the creation of a novel multipassing laser cavity for low-density plasmas, the design and construction of a fiber-based probe for flexible light collection, and the implementation of Thomson scattering in a weakly collective regime.

5.3.1 Multipassing Thomson Scattering Cavity

Before the development of a second laser system capable of driving higher-density plasmas, it was necessary to design a single-shot Thomson scattering diagnostic that could be effective at low ($\sim 5 \times 10^{12}$ cm^{-3}) densities. As discussed in section 5.2.1, the number of scattered photons at these low densities is generally insufficient to overcome noise from background emission, particularly stray-light. Since most of the laser energy is not scattered during a sampling event, one solution is to try and reuse the laser energy in order to increase the number of sampling events per shot. This led to the development of a multipass laser cavity based on injection by frequency conversion [72].

Multipassing schemes had been implemented before with a similar goal to integrate the scattered signal over multiple measurements [3, 8, 36]. Unlike these designs though, the multipass cavity developed at UCLA used frequency conversion to trap the beam inside the

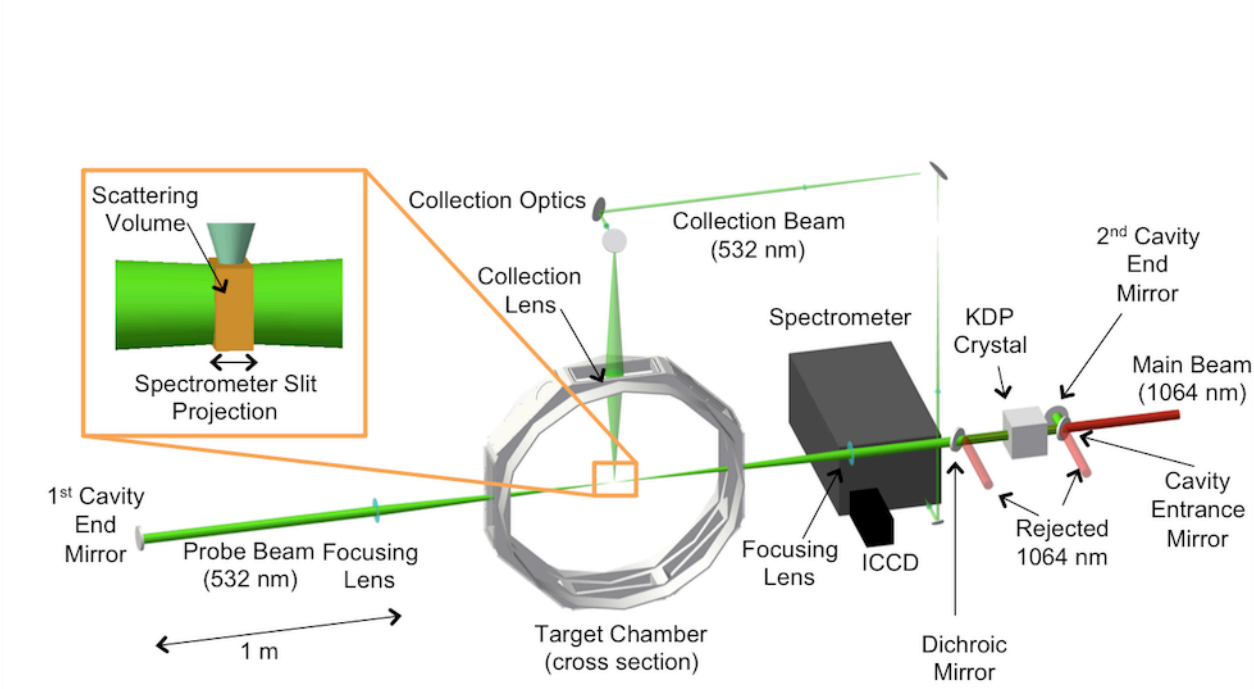

Figure 5.9: Schematic layout on the LAPD for the Thomson scattering multipass cavity. Adapted from [72].

cavity. This has the advantages that the input laser energy is only limited by the optics' damage thresholds, that the laser beam size is only limited by the size of the optics, and that the probe beam passes through the same scattering volume and is collected at the same scattering angle (within alignment errors) every cycle of the cavity. The primary limitation is the integrated sampling time, which may be longer than the event of interest.

A schematic of the multipass cavity is shown in Fig. 5.9. Details on the cavity construction can be found in [72]. The salient features are the inclusion of a frequency-doubling crystal (type 2 potassium dihydrogen phosphate [KDP]) inside the cavity cell and the use of a dichroic mirror to reject unconverted laser light but transmit converted light. The scattered light was collected with a standard optical imaging transport system. A mask was placed between the spectrometer and the camera to block diffracted light around the laser wavelength. The cavity was aligned and evaluated with the use of photodiodes and CCD cameras placed at the leaks of the cavity mirrors. Fig. 5.10 shows the performance of the

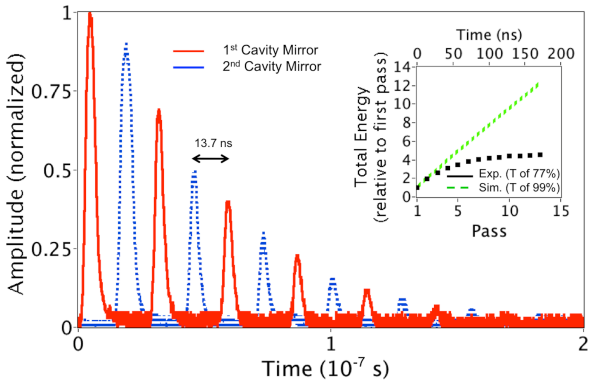

Figure 5.10: Interlaced diode signal from leaks of the first cavity mirror (solid line) and second cavity mirror (dotted line). Inset shows total energy on target (squares) for a KDP crystal transmission of 77% and the simulated total energy on target (dotted line) for a crystal transmission of 93%. Adapted from [72].

cavity and integrated energy over time. The cycle-to-cycle degradation ($\sim 30\%$) was dominated by the low transmission efficiency (77%) of the KDP crystal. Despite the losses, the integrated energy in the scattering volume asymptoted to $4\times$ the input energy over 160 ns.

The Thomson scattering multipass cavity was deployed on the LAPD (see Chapter 2) to study the ambient plasma in a purely non-collective regime. Note that the ambient plasma persisted for several ms, much longer than the integrated sampling time. A more efficient YCOB crystal [23] was used, reducing the losses per pass and increasing the integrated energy to $\sim 10\times$ the input energy. Even with the increased energy, it was still necessary to average over 100-1000 measurements and to bin the ICCD into 16×1 superpixels in order to achieve sufficient signal[2]. A sample Thomson spectrum is shown in Fig. 5.11 with an applied instrument-broadened (see section 5.2.2) Gaussian fit. The electron temperature was measured to be $T_e = 6.3^{+5.8}_{-4.1}$ eV, consistent with measurements made with Langmuir probes.

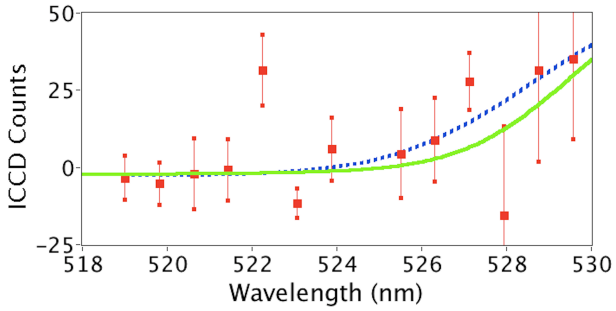

Figure 5.11: Stray-light and background subtracted Thomson spectrum (squares) per laser pulse using the multipass cavity on the LAPD. Also shown are the best non-collective fit (dotted line) and a simulated Thomson spectrum (solid line) for an electron temperature of 5 eV, normalized to the amplitude of the best fit. Adapted from [72].

5.3.2 Fiber Probe Design and Construction

One of the limiting factors of a Thomson scattering diagnostic is the relatively inflexible optical collection setup. For the work presented here, it was generally desirable to probe multiple spatial locations without sacrificing spatial resolution or placing optics near the scattering volume. In the environment of the LAPD, it is especially difficult to mount collection optics. Inside the chamber, optics tend to be destroyed by the plasma, while outside the chamber optics have to be large in order to collect sufficient signal. In both cases, the optics are fixed, requiring either a large field of view (and reduced resolution) to probe many locations or a single, fixed scattering volume.

To overcome these limitations, a custom fiber-optic probe was designed that could be translated in place while providing sufficient collection power and resolution. A schematic of the fiber probe is shown in Fig. 5.12. The core of the probe is a custom-built, flexible fiber-optic bundle from Fiberoptic Systems, Inc. The bundle consists of 20 200 μm or 40 100 μm UV-grade cladded silica fibers ($NA = 0.22$) arranged in a 0.5 cm long linear array. The fibers are protected by a heat-resistant (400° C) polyimide buffer and encased in a flexible

[2]This is consistent with the results of section 5.2.1. Repeating the measurement 100 times while decreasing the number of channels by a factor of 10 increases the signal-to-noise ratio by approximately a factor of 30 – just enough to yield $S/N \approx 3$.

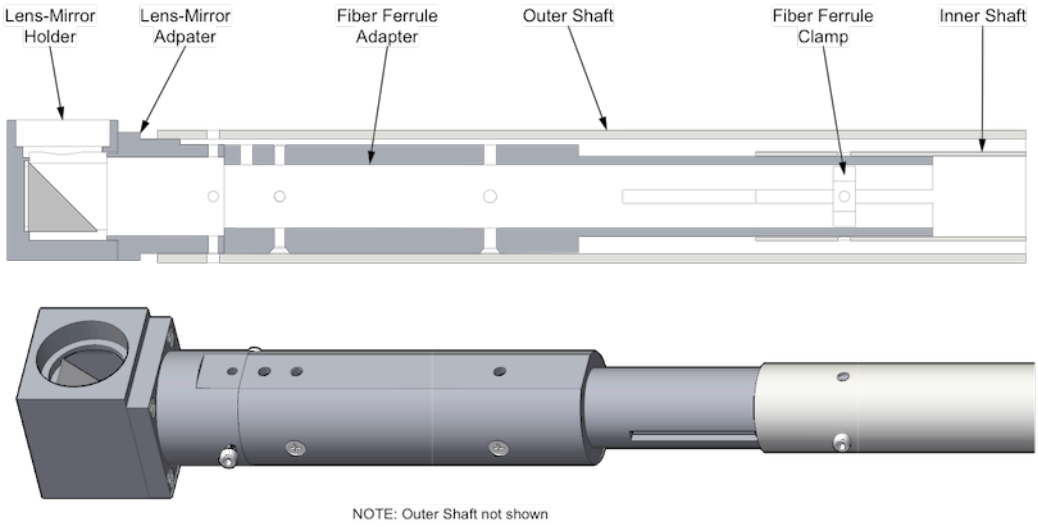

Figure 5.12: Schematic of fiber probe (vacuum end). The 90° lens-mirror holder can be replaced with a 0° version (*i.e.* no mirror).

stainless steel interlock with specially-designed stainless steel end caps. A KF-40 vacuum flange with epoxy feedthroughs allows the fibers to pass from vacuum to atmosphere. The fiber bundle can be mounted in a telescoping cage. The outer tube of the cage allows the fibers to translate freely, while the inner tube allows the fibers to be adjusted relative to a lens. On the vacuum side, the fibers are coupled to a Ø0.5″ SM05 lens threaded into a 0° or 90° holder mounted to the outer tube of the cage. The holder allows an image to be projected parallel or perpendicular to the fiber axis. On the spectrometer (air) side, the fibers can be mounted directly against the entrance slit.

To understand the properties of the collected image, it is easiest to work backwards. The final image plane, by design, is the CCD of the detector camera. Since the spectrometer is of the imaging type, this image plane will be projected 1:1 (*i.e.* magnification $M = 1$) to the spectrometer entrance slit. The fibers will transport this image plane unaffected from one end to the other, since the f# of the fibers ($N_{f,fibers} \sim 2.3$) is smaller than that of the spectrometer ($N_{f,s} = 4 - 8$). The role of the lens is to project the image plane at the end of the fibers to the desired scattering plane. To maximize light coupling, the position i of the lens should be set so that the f# of the light cone matches the spectrometer: $i = 2r \cdot N_{f,s}$,

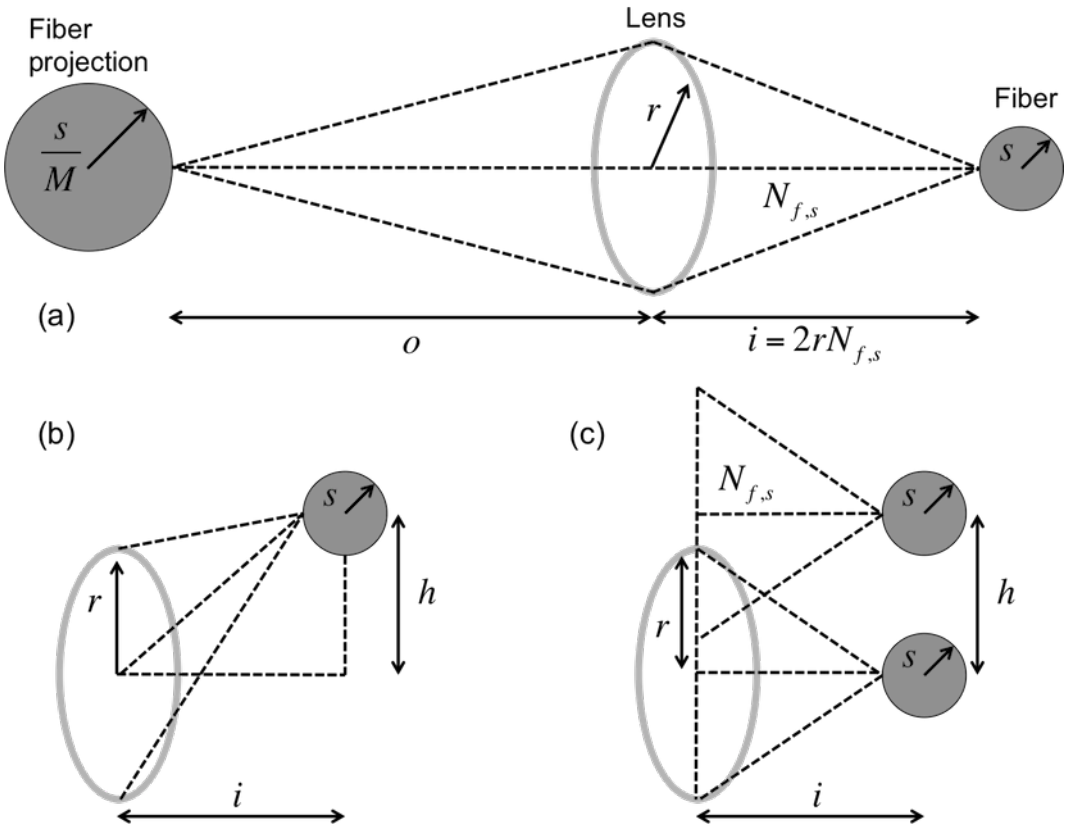

Figure 5.13: (a) Diagram of fiber probe imaging, where the image distance i is chosen such that the beam cone has the spectrometer f# $N_{f,s}$. The projected fiber image is magnified by a factor M. (b) Diagram of an off-axis fiber. (c) Diagram of overlapping light cones, each with f# $N_{f,s}$, from two fibers. The center fiber fully utilizes the lens, while a fiber at height h collects an amount proportional to the overlap between the lens and its light cone.

where r is the radius of the lens (see Fig. 5.13a). This will give the lens an effective focal length $f = (i \cdot o)/(i + o)$, where o is the distance from the lens to the scattering plane and the thin lens equation $\frac{1}{f} = \frac{1}{i} + \frac{1}{o}$ has been used. Ideally, the actual focal length of the lens should be close to the effective focal length. The image will also be demagnified by a factor $1/M = o/i$.

The above calculations are valid for a single fiber positioned on the center axis of the lens. Because there's an array of fibers, the image properties on each fiber will vary. The position of the lens was chosen so that the f# of the light cone on the *center* fiber matches

the spectrometer. The effective f# on a fiber a distance h from the center axis goes like (see Fig. 5.13b)

$$N_{f,fibers}(h) \simeq \frac{1}{2}\left[\sin\left(\frac{h+r}{\sqrt{(h+r)^2+(2rN_{f,s})^2}}\right)\right]^{-1} \tag{5.41}$$

Note that as $h \to 0$ or $r \to \infty$, $N_{f,fibers}(h) \to N_{f,s}$. It is also of interest to calculate how much light is collected by off-axis fibers compared to the central fiber. To proceed, a useful geometric equation for the area A of overlapping circles is used:

$$\begin{aligned} A(h) = {} & s^2 \arccos\left(\frac{h^2+s^2-r^2}{2h\,s}\right) + r^2 \arccos\left(\frac{h^2+r^2-s^2}{2h\,r}\right) \\ & - \frac{1}{2}\left[(-h+s+r)(h+s-r)(h-s+r)(h+s+r)\right]^{1/2} \end{aligned} \tag{5.42}$$

where r and s are the circle radii separated by a distance h (see Fig. 5.13c). Recall that the position of the lens relative to the center fiber is chosen to maximize light collection; it follows, then, that the radius of the central fiber s projected onto the lens is equal to the lens radius r, *i.e.* $s = r$. From Eq. 5.42 (and common sense), the area of collection for the center fiber ($h = 0$) is just $A_0 = \pi s^2$. A fiber at the edge of the lens ($h = s$) then has a collection area of $A_s = 0.4\pi s^2 = 0.4\,A_0$, or 40% of the center fiber's collection. The collection area goes to zero for fibers at a height $h \geq 2s$. Note that increasing the lens radius while keeping the distance between the fibers and lens fixed ($r > s$) will increase the collection area for off-axis fibers.

For an LAPD experiment, the fiber probe was placed a distance $o = 300$ mm from the scattering plane and used a $2r = 12.7$ mm lens and $N_{f,s} = 4$ spectrometer. Additionally, the image height (determined by the magnification and detector CCD size) was $2h = 17$ mm. This yields $i = 50.8$ mm, $f \sim 43$ mm, and $1/M \sim 6$. The light collected by the farthest fiber was then 22% of the light collected by the center fiber. The total light collected (integrated over all fibers) was 59% of the light that would have been collected if all fibers collected the same amount of light as the center fiber. A typical spectrum taken by the fiber probe in the LAPD in shown in Fig. 5.14.

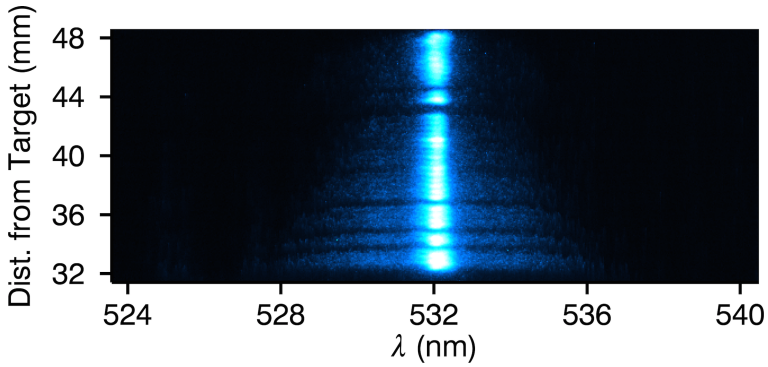

Figure 5.14: Example spectrum taken by the fiber probe in the LAPD. Missing data (dark streaks) is due to broken fibers.

5.3.3 Single-Shot Thomson Scattering

With the addition of a second laser system to the Phoenix laboratory, a single-shot Thomson scattering diagnostic became feasible. However, this required a different beamline construction than the multipassing cavity (see section 5.3.1). A schematic of the single-shot Thomson beamline is shown in Fig. 5.15a.

The Phoenix laser was used as the seed laser with a wavelength of 1064 nm (1ω). It was frequency-doubled to 532 nm (2ω) using a type 2 KDP crystal. The crystal could be rotated to accept any incident linear polarization, and it output the 1ω and 2ω beams with orthogonal polarizations, both rotated 45° relative to the input polarization (see Fig. 5.15b). The 1ω light could be readily removed with a lowpass filter or through attrition from multiple non-1ω-coated optics. The polarization of the 2ω beam was fixed based on the scattering geometry. As a result, a 1/2 waveplate was necessary to rotate the 2ω beam to the correct polarization. This rotation could be done before or after the crystal with the aid of a Glan-Thompson polarizer (GTP) as follows (the pre-waveplate polarization of the laser was assumed known).

If before, the GTP is placed between the waveplate and the crystal. If after, the waveplate is placed after the crystal and the GTP after the waveplate. Before installing the waveplate, the GTP is zeroed by rotating it until the 1ω (2ω if after) beam disappears (this will be at

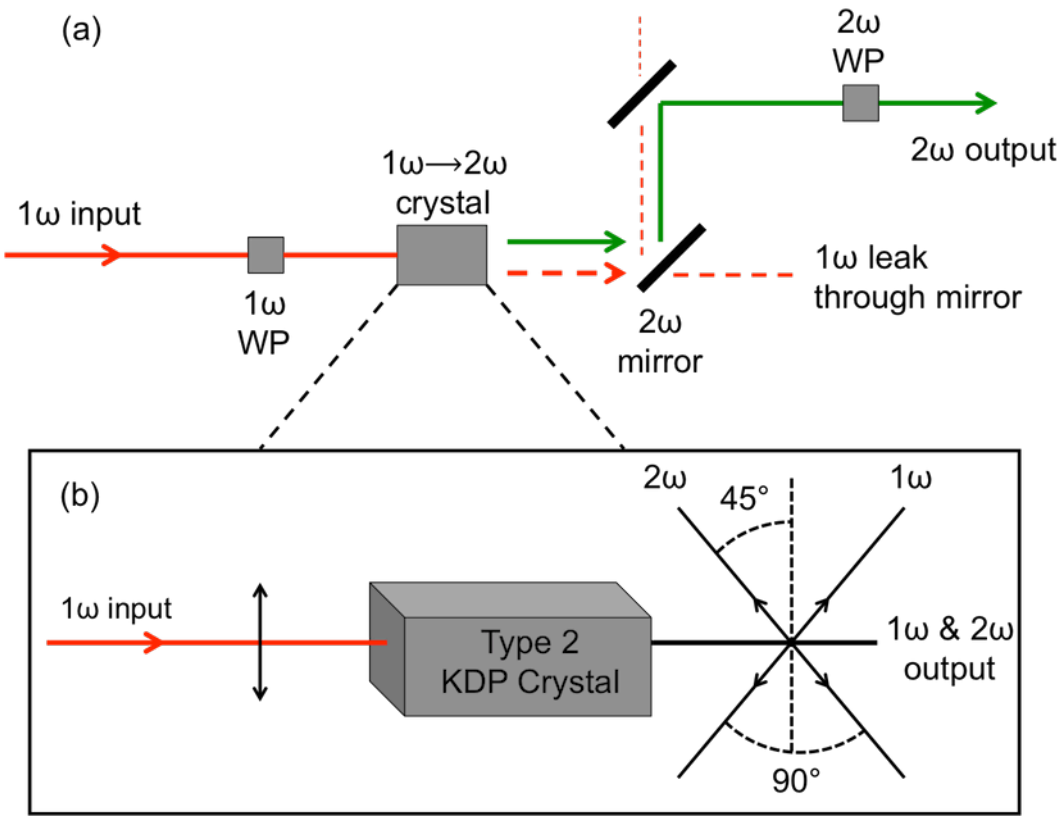

Figure 5.15: (a) Schematic of a single-shot Thomson scattering beamline. The input beam at frequency 1ω is doubled by a type 2 KDP crystal, which outputs both 1ω and 2ω beams. The final polarization of the 2ω beam is accomplished by a waveplate (WP) either before or after the crystal. (b) Diagram of the effect of a type 2 KDP crystal on an input 1ω beam with linear polarization.

some GTP angle θ_0). The 1/2 waveplate is installed and zeroed by rotating it until the 1ω (2ω) beam disappears behind the GTP fixed at θ_0 (this will be at some waveplate angle ϕ_0). The waveplate is then rotated by an angle $\Delta\phi$ that is half the total desired rotation (since it is a 1/2 waveplate). The 1ω (2ω) beam should now disappear by rotating the GTP an angle $\Delta\theta = 2\Delta\phi$. If done before, note that the crystal will also have to be rotated by $\Delta\theta$ and that the 2ω beam will be rotated by $\Delta\theta + 45°$.

Alignment techniques and collection beamlines for multiple setups are described in Chapter 2. An important constraint on the collection setup is that it relay the image plane at the

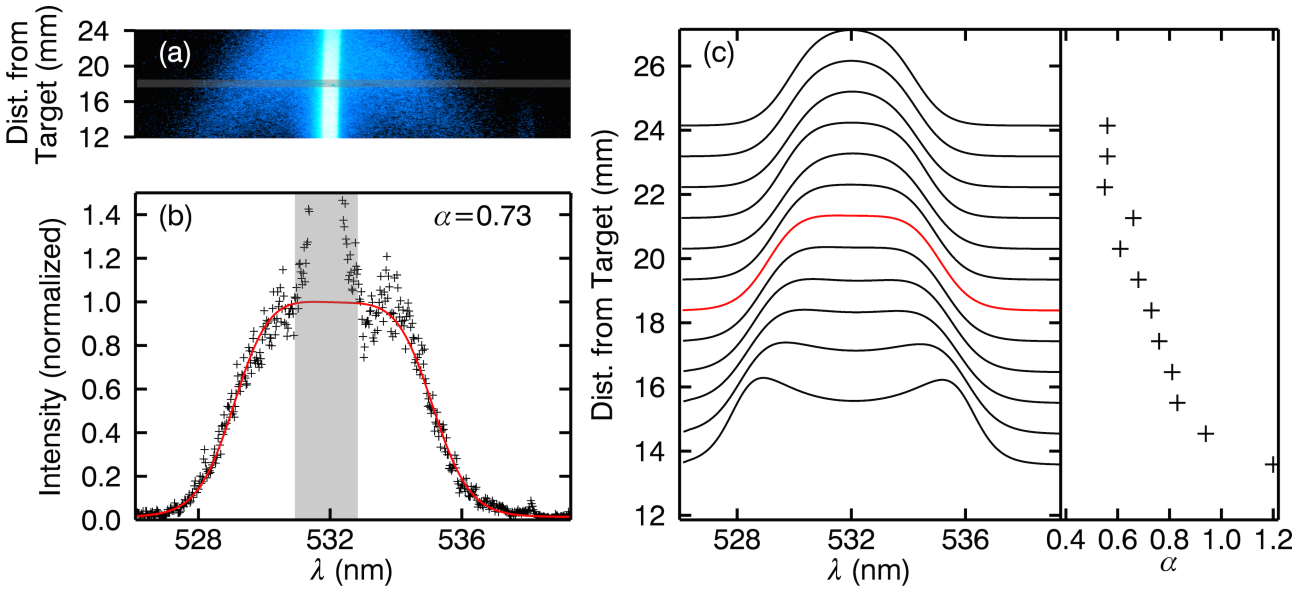

Figure 5.16: (a) An example false-color, spatially-resolved Thomson spectrum. (b) A stray-light and background subtracted lineout (crosses) from the highlighted region in (a) with corresponding collective Thomson fit (solid line). The ion feature is visible near the laser wavelength ($\lambda_i = 532$ nm), but is not spectrally resolved and so is masked (highlighted region) for the purpose of fitting. (c) Collective Thomson fits derived in a similar manner to (b) [shown in red] for multiple spatial locations. Also shown is the value of the scattering parameter α for each fit as a function of distance. The spatial gradient from relatively non-collective ($\alpha \sim 0.4$) scattering farther from the target to weakly collective ($\alpha \sim 1$) scattering nearer to the target is clearly visible.

scattering volume to the detector CCD (see for example section 5.3.2). A useful technique for aligning the collection beamline is to use a continuous HeNe laser that originates at the detector plane and passes through the optical setup to the scattering plane. Combined with a similar HeNe laser passing through the probe beamline, these lasers define a precise scattering volume (where, for example, an alignment pin could be placed for reference).

5.3.4 Scattering in a Weakly Collective Regime

An example Thomson spectrum taken using the setup described in section 5.3.3 is shown in Fig. 5.16. The spectrum is spectrally, spatially, and temporally (with a 3 ns gate width) resolved. Since CCD or grating non-uniformities can introduce a spectral non-uniformity along the spatial dimension, the image was divided into multiple, equally-spaced sets, and each set was calibrated using spectral lines from neon and mercury spectral calibration lamps. The spatial dimension was calibrated by placing an object of known size (such as a pin head) in the scattering plane and imaging it onto the detector.

Spectra taken without a plasma or with the probe beam polarized parallel to the collection axis provide the stray-light response, which can then be subtracted from the Thomson spectra (see Fig. 5.16b). If necessary, spectra taken with just an ablated plasma can provide the plasma emission response and can be similarly removed. The remaining Thomson-only spectrum is fit using a Levenberg-Marquardt best-fit algorithm. At each iteration of the algorithm, a full collective spectral density function (see Eq. 5.23) is generated at a given set of plasma parameters (T_e, n_e, *etc.*) and convolved with the spectrometer instrument function (also obtained using calibration lamps, see section 5.2.2). Note that in general, the ion feature was not resolvable, so only the electron contribution to the collective spectral density function was used. The result is compared with the real spectrum and the parameters are modified until they minimize the weighted mean square error between the fit and real spectrum. Note that Thomson spectra are unique – it is not possible to generate the same spectrum using two unique sets of plasma parameters. The final fits generally had errors of $T_e \pm 0.3$ eV from $1 - 5$ eV, $n_e \pm 0.2 \times 10^{16}$ cm^{-3} from $10^{15} - 10^{16}$ cm^{-3}, and $n_e \pm 0.7 \times 10^{16}$ cm^{-3} from $10^{16} - 10^{17}$ cm^{-3}.

It can be seen in Fig. 5.16b that a weakly collective ($\alpha \sim 0.73$) spectrum fits well with the real spectrum. It can also be seen that the degree of the collective effect smoothly varies over the image, with the least collective ($\alpha \sim 0.55$) spectrum farthest from the target and the most collective ($\alpha \sim 1.2$) spectrum nearest the target (see Fig. 5.16c). This is expected,

since while the plasma nearest the target is the hottest and most dense, the density falls off faster than the temperature, decreasing α overall (see Eq. 5.25 and Chapter 4). This is the first spatially-resolved imaging of the transition from collective to non-collective scattering.

CHAPTER 6

Conclusion

The primary goal of this research project was to generate in a laboratory setting magnetized, quasi-perpendicular collisionless shocks using a laser-driven magnetic piston. This was a collaborative effort and required extensive resources to build the necessary laser hardware and operating software. The result was the successful (albeit limited) creation of a subcritical collisionless shock. This process can be used to further study collisionless shock formation in a regime not readily available to spacecraft

The secondary goal was to develop a Thomson scattering diagnostic capable of studying plasma parameters in moderate density, low temperature plasmas such as laser-produced plasmas a few cm from the target or the shock transition layer. A Thomson scattering diagnostic was successfully designed and deployed in multiple environments and in multiple configurations, including a classical optical image relay, a multipassing laser cavity, and a fiber-based probe relay. The diagnostic provided spatially and temporally resolved measurements of electron temperature above 1 eV and electron density above 10^{13} cm^{-3}.

The principle findings of this work include:

- Magnetic field measurements indicate that a subcritical, quasi-perpendicular, magnetized collisionless shock was created using a laser-driven magnetic piston. Before dissipating in a low-density ambient plasma, the magnetic pulse moved super-Alfvénically ($M_A = 2.1$) with a magnetic compression $B_z/B_0 = 2.0$, consistent with the Rankine-Hugoniot jump conditions for a low-Mach number collisionless shock. The pulse also had a steep leading edge ramp ($\delta = 0.5c/\omega_{pi}$), consistent with subcritical shock formation, and was beginning to separate from the piston. 2D hybrid simulations reproduced

these features.

- In combination with the above result, previous shock experiments in which no shock or a pre-shock was formed allowed the various experiments to be organized by weak, moderate, or strong coupling. These categories correspond to distinct features in the magnetic profiles of the shock structures, with weak coupling corresponding to weakly compressed super-Alfvénic pulses, moderate coupling corresponding to well-compressed but un-steepened pulses, and strong coupling corresponding to a full shock.

- Multiple shock formation criteria were investigated, revealing that the most important criteria, in addition to being super-Alfvénic ($M_A > 1$), were the coupling $\epsilon > 0.5$ and magnetization $\mu > 1$ parameters. Within these parameters, the most important experimental consideration for shock formation was the amount of space (D_0) over which ambient conditions were relatively constant. The successfully created laboratory shock was the only one with experimental conditions that satisfied all shock formation criteria.

- Using the results of laser plasma characterization studies to calculate shock formation criteria, the shock experiments were found to lie in distinct regions of an ϵ-μ parameter space, which agreed well with the observed shock formation regimes of weak coupling ($\epsilon < 0.5$, $\mu < 1$), moderate coupling ($\epsilon > 0.5$, $\mu < 1$), and strong coupling ($\epsilon > 0.5$, $\mu > 1$). This indicates that the ϵ and μ parameters are capturing most of the physics of laboratory shock formation.

- Data from experiments on a laser-produced plasma were best fit with an isentropic, adiabatic fluid model, which agreed well with measured spatial temperature and density profiles over a range of laser intensities. Fits to the temperature profiles further suggest a modified plasma adiabatic index $\gamma = 4/3$ instead of its ideal gas value $\gamma = 5/3$. This is consistent with a recombination-dominated plasma for which $T_e \propto t^{-1}$. The fluid model predicted values for total ablated particle number and expansion speed that agreed well with empirical scaling laws. However, the overall slow expansion speeds

indicated that the Thomson scattering and spectroscopic diagnostics were primarily probing a higher mass bulk plasma and not the leading plasma edge. The results also indicated that most laser energy is not transferred to the ablated plasma as kinetic energy ($< 25\%$), though the efficiency increases with laser intensity.

- 1D HELIOS simulations of the laser-target interaction agreed well qualitatively, and in some cases quantitatively, with measurements and analytic modeling. In particular, the simulations matched well with the model-derived ablated particle number and its dependence on laser intensity. The simulation-derived expansion speeds also agreed well with magnetic field measurements, which are generally much faster than speeds measured by Thomson scattering or spectroscopy and more indicative of the plasma's leading edge. The simulations, like the data, predicted increasing laser-to-plasma efficiency with intensity, though the value of the efficiency was higher. This was largely due to the addition of the plasma's internal energy, was was not included in the fluid models, and suggests the laser-to-plasma energy conversion efficiency may be better than what was observed through plasma motion alone.

- Spectroscopic measurements and HELIOS simulations both saw velocity separation by charge state, with the highest charge states moving fastest. Simulations also agreed well quantitatively with the average speed of the charge states as measured spectroscopically. However, most of the plasma mass lay in the lowest charge states, especially at higher laser intensities. Simulations were used to track the relative population of each charge state with laser intensity, which revealed that the fastest non-trivial population (the dominant charge state) at typical experimental conditions was CV (C^{+4}).

- The Thomson scattering diagnostic was used to measure for the first time a spatially-resolved image of the transition from the collective to non-collective scattering regime. Since collective scattering can directly yield density measurements, the result allowed accurate modeling of the spatial density profile of a laser plasma, even at low densities that normally require additional calibration.

- Thomson scattering was successfully utilized on the Large Plasma Device in both a single-shot and high-repetition configuration. With a single-shot setup, laser plasma parameters were measurable up to 10 cm from the target. With a high-repetition setup, the lower-density ambient plasma was directly probed. The diagnostic was also successfully deployed on the Trident Laser Facility and Phoenix chambers.

The results of this work lay the foundation for multiple future research directions. Additional laser-plasma characterization is needed, especially measurements on charge state evolution to better benchmark simulations. With further reductions in stray-light, the Thomson scattering diagnostic can directly probe low-density ($\sim 10^{13}$ cm^{-3}) ambient plasmas. This will be critical when trying to studying density compressions, dissipation, or anomalous electron heating in the shock ramp. With a process for generating collisionless shocks now available, higher Mach number (supercritical) or quasi-parallel shocks, never achieved in a laboratory setting, can also be attempted.

APPENDIX A

Hardware Development for the Phoenix Laser Laboratory

When the Phoenix laser laboratory consisted of just the Phoenix laser and pulsed power systems, it was possible to manually operate the laser from within the laser bay. With the addition of the Raptor high-energy and Peening high-repetition lasers, this was no longer safe or feasible. As a result, it was necessary to find a way to integrate all of the laser system components – including the pulsed power systems, diagnostics, water chillers, and interlocks – such that they were automated and remotely accessible. The solution was to incorporate a series of National Instruments (NI) CompactRIO (cRIO) platforms.

A.1 NI cRIO Architecture

The cRIO platform consists of a hardware chassis – containing a field-programmable gate array (FPGA) and slots for I/O modules – and an integrated controller containing a CPU, memory, and ethernet ports. The cRIO is programmable in LabVIEW and is divided into a real-time host VI (virtual instrument) and a FPGA VI. The host VI lives on the controller, which acts like a standard PC and supports most LabVIEW functions, including networking. By adding I/O modules to the chassis, I/O channels are exposed to the FPGA. The FPGA VI then configures the behavior of the FPGA through logic on the I/O channels, and is only accessible through the host VI. It is programmed with a transparent (but more limited) extension of LabVIEW and is, once compiled, flashed to the FPGA. While the FPGA is programmable, it remains deterministic. A schematic of the cRIO architecture is shown in

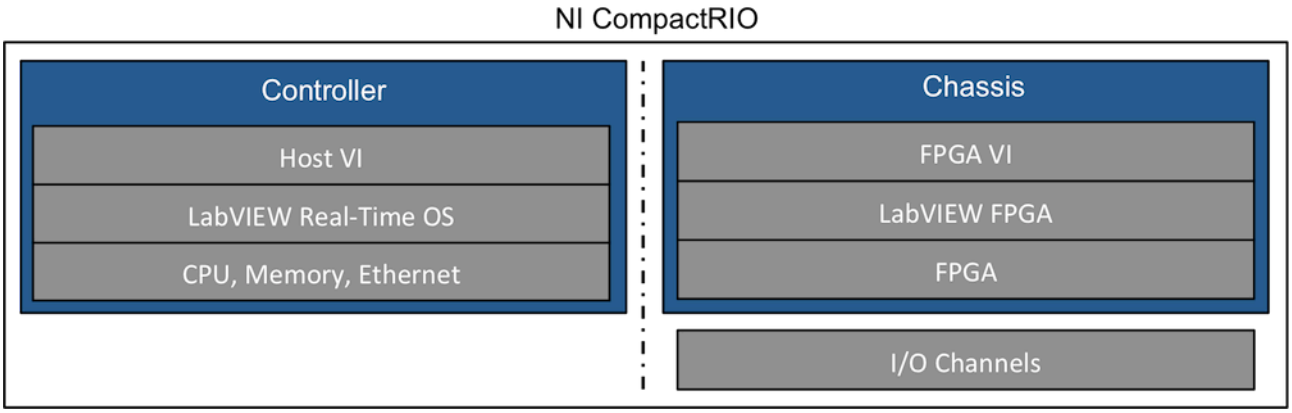

Figure A.1: Schematic of the NI CompactRIO architecture.

Fig. A.1.

Because the cRIOs are self-contained, they can be set up as stand-alone systems. As such, they run independently of any of the higher-level software systems while remaining accessible through network ports. To achieve hardware integration, related-function I/O channels and FPGA logic (*e.g* pulsed power) are combined into a "RIO" instrument, with one or more RIO instruments hosted on a cRIO. RIO instruments are then presented transparently through custom cRIO drivers as a hardware resource to higher-level software.

Multiple RIO instruments on several cRIO devices were created for the laboratory. Laser frontend instruments – including Phoenix, Raptor, and Peening – handle logic for configuring the frontends. Pulsed power instruments – also including Phoenix, Raptor, and Peening – control the precise (μs) timing of the charging and discharging sequences, in addition to monitoring and logging the state of the system during these sequences. Interlock instruments were created for each interlock zone in the lab, such as a laser frontend or pulsed power system, and control and monitor the state of that zone, including applicable doors, shutters, and status lights. Interlock instruments can also be aggregated to monitor the state of a larger zone. Scope instruments can acquire multiple voltage traces with configurable sample rates up to 1 MHz from diagnostics such as energy calorimeters. Timing box (pulse generator) instruments can monitor input signals and configure the pulse width and timing of output signals with sub-μs resolution. Switchboard instruments are used to get and set the digital

state of general-purpose DIO channels. Finally, chiller instruments control and monitor the flow of cooling water to various amplifiers. Together, these instruments control and monitor ~ 1000 I/O channels throughout the lab.

A.2 cRIO Driver Architecture

The cRIOs use a common instrument driver architecture to facilitate modularity and scalability. The instrument driver utilizes LabVIEW object-oriented programming (LVOOP) and defines a root driver class that specifies network communication and message handling (see Appendix B for details on OOP). Type-specific driver classes (*e.g* laser frontend, pulsed power, *etc.*) then inherit from the root driver class and add functionality. Network communication is by default handled through LabVIEW network streams, but can be configured to use any network protocol. The message handler translates instrument commands sent over the network and processes them for hardware output through the FPGA. Conversely, it also takes hardware input from the FPGA, processes it, and passes it out over the network as requested. cRIO driver classes include scopes, timing boxes (pulse generators), switchboards, shutters, laser frontends, pulsed power systems, and interlocks.

A cRIO RIO instrument (*e.g* Phoenix laser frontend) is defined by a series of I/O channels and corresponding FPGA logic. The RIO instruments are encapsulated by an instrument-specific class that inherits from the appropriate driver class. In this way, instrument-specific I/O can be called through more general dynamic dispatch methods without having to write new drivers for every RIO instrument. For example, a cRIO scope driver can define an "Enable Channel" method. This method can then call an abstract dynamic dispatch method "Enable Channel Core". An individual RIO scope can then override the dynamic dispatch method to pass the channel state to the appropriate FPGA I/O channel. A schematic of the cRIO driver architecture is shown in Fig. A.2

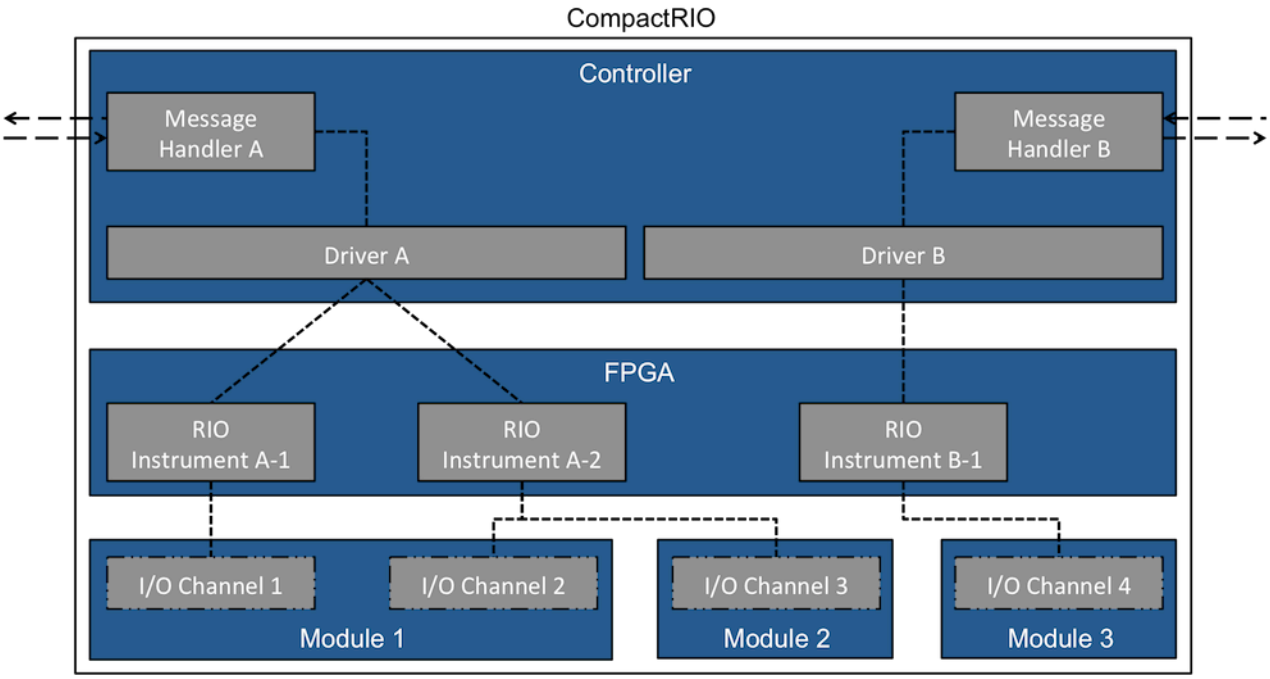

Figure A.2: Schematic of the cRIO driver architecture.

APPENDIX B

Software Development for the Phoenix Laser Laboratory

Development of multiple laser systems, pulsed power systems, interlocks, and diagnostics necessitated the development of a comprehensive software framework to control and monitor these systems. Requirements of the software included: simultaneous operation of one or more lasers and corresponding pulsed power systems; real-time monitoring of multiple laser diagnostics, such as cameras, energy calorimeters, and photodiodes; and real-time monitoring of all interlock systems, including doors and shutters. Additionally, due to the inherently unsafe nature of high-energy lasers and high-voltage power supplies, the software needed to have remote access to this hardware. The solution was the creation of a custom National Instruments (NI) LabVIEW software package known as the Phoenix System Terminal (PST). The PST was featured in the NI *Sweet Apps* blog, in the NI worldwide *Instrumentation* newsletter, and at NI Week.

B.1 Global Architecture

The PST is a custom LabVIEW application (a "terminal", see following sections for more details) that can run simultaneously on multiple computers. Each terminal is independent, but can communicate with other terminals on a local subnet to create a decentralized network architecture. A terminal stores machine-specific configurations on the local machine, but accesses global configurations (such as instrument settings) common to all terminals from a shared server.

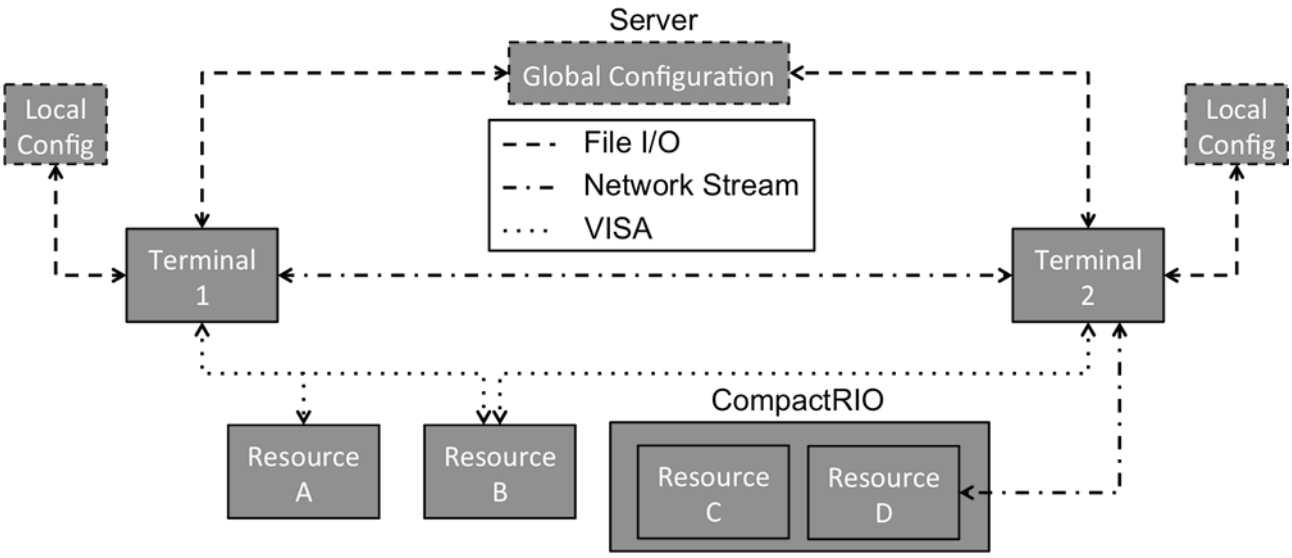

Figure B.1: Schematic of PST global architecture. Terminals can communicate with local and global configurations through file operations, with one another through the network stream protocol, or with hardware resources through network streams or the VISA protocol.

Custom drivers for laser and pulsed power systems, as well as custom systems like interlocks and closed-loop water chillers, are encoded on NI CompactRIO FPGA systems (see Appendix A). All hardware resources, including diagnostics and CompactRIOs, are made available to every terminal through transparent network protocols. As a result, any terminal at any location on the local network can operate any hardware resource. This allows, for example, the lasers to be aligned from within the laser bay but controlled remotely during full-system operation.

In addition to communicating with hardware, programs within a terminal can communicate with non-local programs running on another terminal using LabVIEW network streams, which are a 1-to-1 lossless network protocol. This allows, for example, a program controlling a laser to indicate when a shot has completed to a program monitoring laser diagnostics. A schematic of the PST global architecture is shown in Fig. B.1.

B.2 Programming Architecture

The entire PST application stack is written in LabVIEW and makes extensive use of LabVIEW object-oriented programming (LVOOP). In OOP, code is organized by "objects" instead of functions. An object is an instantiation of an object class, which includes all the methods that can act on the object. There are three distinct advantages of LVOOP compared to procedural programming: encapsulation, inheritance, and dynamic dispatch. Encapsulation is the process by which private data is assigned to an object class, and the mechanism by which methods can access this data. An object class (the child class) can inherit from another object class (the parent class), allowing the child class to encapsulate new data while retaining the data associated with the parent class. Finally, a method in a parent class can be designated as dynamic dispatch, allowing a child class to override that method with its own implementation. Together, these features make LVOOP a powerful tool for creating modular, large-scale software applications.

The PST utilizes the actor framework (AF), which is a software framework that supports applications in which multiple VIs (virtual instruments) run independently while communicating with each other. In this sense, each VI is an "actor" that carries out an independent task within the system, such as a user interface or background process. The AF is an OOP implementation of a queue-driven state machine (QDSM), in which messages queued elsewhere are dequeued in the QDSM and trigger different cases depending on the message. In the AF, the root actor class encapsulates a message queue and defines a public method for launching new actors. The launching method calls a private dynamic dispatch method that defines a QDSM. This private method is also reentrant, which allows multiple copies of it to run simultaneously. Thus, every actor runs a copy of the same method but can add new functionality (like a user interface) by overriding it.

Actors can launch or be launched by other actors, and can communicate with other actors through messages using the encapsulated queue. The messages are themselves objects of a message class, and each child message class defines a dynamic dispatch execution method

that specifies what action to perform. When the actor's QDSM receives a message object, it calls that message's execution method, processes errors, and then waits for the next message. By using objects as messages, the AF allows new functionality to be easily added through the creation of new message classes.

Because actors can inherit from and override parent classes, the AF also enables the PST to utilize a plugin architecture. In a plugin architecture, an actor (interface) class defines a plugin interface, which is a collection of methods that define how actors (plugins) that inherit from the interface class should be called. Plugins themselves are pre-compiled packed project libraries (PPLs) that include the plugin actor class, its messages, and any dependencies. Actors (not necessarily related to the interface class) can then load any class that inherits from the interface class by calling the plugin interface methods. This allows an actor to dynamically call plugins that may not be loaded at run-time, including plugins that are made available after the actor is already running. For example, a camera diagnostic program (actor) might provide functionality common to all cameras, and also define a camera-specific plugin interface. It could then call a camera-specific configuration panel (plugin actor) as needed, even if the panel isn't made available until after the program is running. In addition to loading specific plugins, the plugin architecture also allows an actor to scan a directory for any available plugins at run-time, such as all available programs for a terminal.

B.3 Application Architecture

A schematic of the PST application stack is shown in Fig. B.2. The first software layer is the resource driver classes. These classes are divided into abstract resource type classes (*e.g.* scope class, camera class, *etc.*), each of which includes one or more child driver classes (*e.g.* Tektronix class, Axis class, *etc.*) that call the instrument driver libraries (which do the actual communication with the instrument). This allows instruments that share common functionality to be grouped together, despite differences in driver commands, protocols,

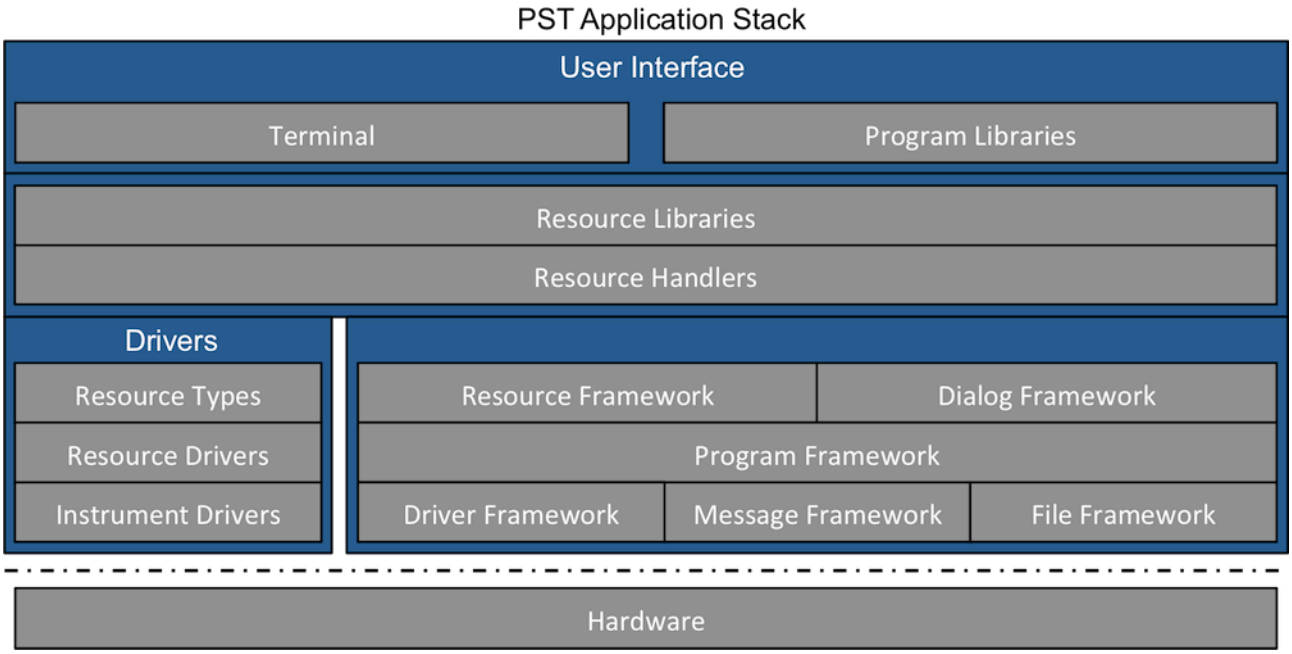

Figure B.2: Schematic of the PST application stack.

etc. Parallel to the driver layer are the application programming interfaces (APIs). These include the low-level driver, message, and file frameworks, the program framework (including the parent program [actor] class), and the dialog and resource frameworks. Building on this first software layer are the resource handlers (actors), which utilize the resource framework to send commands to instruments through the resource drivers. Because resource handlers run independently, they are invoked in the resource libraries layer by resource classes, which are higher-level abstractions of the resource driver classes that can send messages to the resource handlers. These resource classes are, in turn, called by program libraries at the top software level.

When executing the PST application, the application instance first launches a special actor (the splash screen) that loads critical libraries before launching the terminal actor. The terminal is the main graphical interface for interacting with various PST programs, and, being reentrant, can run simultaneously on multiple screens. It includes user-selected programs (plugin actors) arranged in a hierarchical folder structure. Since programs are stand-alone plugin libraries – containing the main program actor, associated messages, child

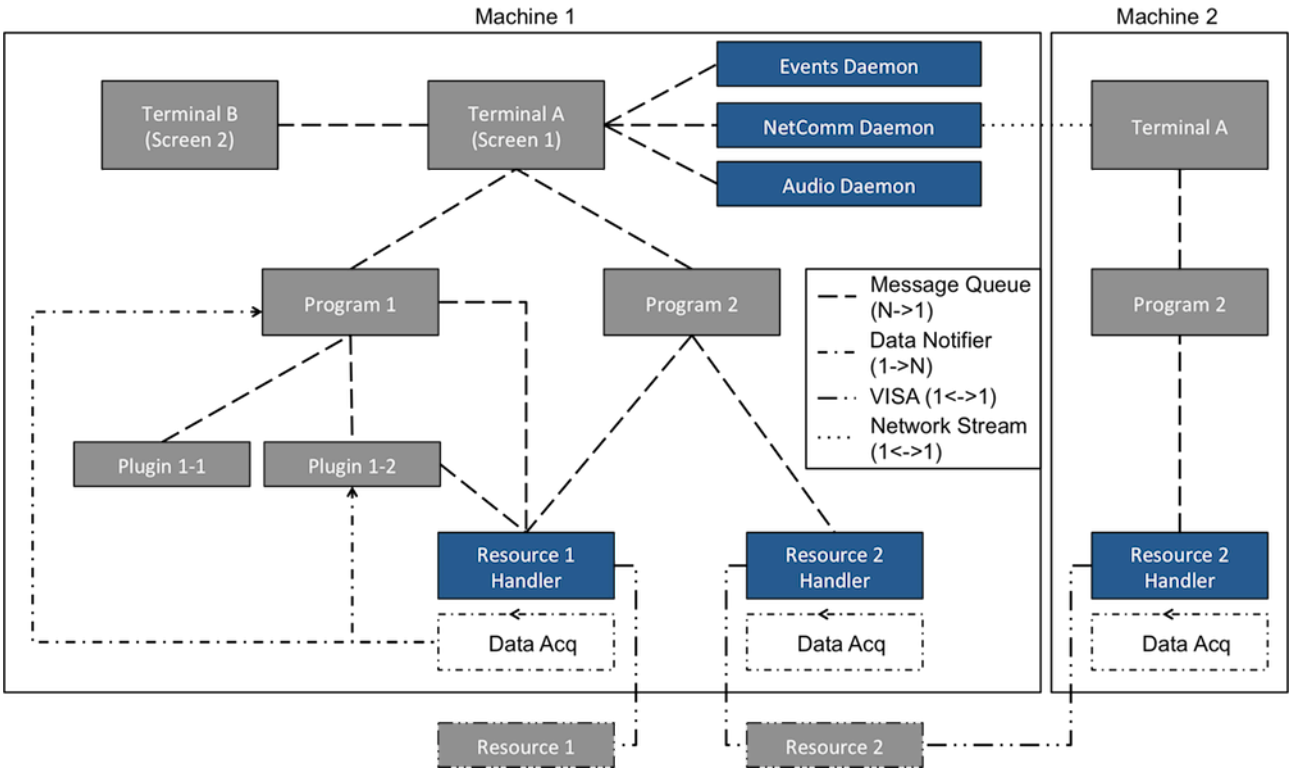

Figure B.3: Schematic of the PST architecture. Programs (including resource handlers and terminals) communicate with one another using N-to-1 message queues. Data acquired by resource handlers is broadcast using 1-to-N notifiers. Resource handlers communicate with hardware using the 1-to-1 VISA protocol. Terminals on different machines communicate with 1-to-1 network streams.

actors, and any additional plugin interfaces – new programs can be added at run-time. When a program is selected, the terminal loads and launches the corresponding program actor. Even though actors are inherently reentrant, by default only one instance of a program can be running on a given machine. Individual programs can modify this behavior. The terminal also launches daemon (background) actors that monitor keyboard events, network communication (netcomm), and audio messages. The terminal keeps track of all running programs, and only it can communicate directly with them. Terminals on different machines, programs within a terminal, or programs within different terminals can communicate with each other through the network communication daemon(s).

In addition to programs, the PST also includes resource handlers (actors). Programs launch resource handlers as necessary when communicating with resource hardware. Within a terminal, only one resource handler is created for each unique hardware device, allowing all communication to that device (including from multiple programs) to be centralized. Data acquisition is also centralized, with only one data acquisition loop per resource handler. Acquired data can then be broadcast to multiple programs. Resource handlers are also stand-alone libraries and are loaded as plugins. A schematic of the PST architecture is shown in Fig. B.3.

References

[1] S. I. Anisimov, D. Bauerle, and B. S. Luk'yanchuk. Gas dynamics and film profiles in pulsed-laser deposition of materials. *Phys. Rev. B*, 48(16):12076–12081, Oct 1993.

[2] V. M. Antonov, V. P. Bashurin, A. I. Golubev, V. A. Zhmailo, Yu. P. Zakharov, A. M. Orishich, A. G. Ponomarenko, V. G. Posukh, and V. N. Snytnikov. A study of the collisionless interaction of interpenetrating super-Alfven plasma flows. *Journal of Applied Mechanics and Technical Physics*, 26(6):757–763, 1986.

[3] C. J. Barth, C. C. Chu, and A. J. H. Donné. Photon recycling system for multiposition tangential Thomson scattering. *Review of Scientific Instruments*, 66(1):501, 1995.

[4] V. P. Bashurin, A. I. Golubev, and V. A. Terekhin. The collisionless deceleration of an ionized cloud dispersing in a uniform plasma in a magnetic field. *Journal of Applied Mechanics and Technical Physics*, 24(5):614–620, September 1983.

[5] S. G. Belostotskiy, R. Khandelwal, Q. Wang, V. M. Donnelly, D. J. Economou, and N. Sadeghi. Measurement of electron temperature and density in an argon microdischarge by laser Thomson scattering. *Applied Physics Letters*, 92(22):221507, 2008.

[6] Yu. A. Berezin, G. I. Dudnikova, M. P. Fedoruk, and V. A. Vshivkov. Explosion phenomena in collisionless plasmas at super-Alfvenic speed. *International Journal of Computational Fluid Dynamics*, 10(2):117–126, 1998.

[7] B. C. Boland, F. E. Irons, and R. W. P. McWhirter. A spectroscopic study of the plasma generated by a laser from polyethylene. *Journal of Physics B: Atomic and Molecular Physics*, 1(6):1180–1228–2, November 1968.

[8] M. D. Bowden, Y. Goto, H. Yanaga, P. J. A. Howarth, K. Uchino, and K. Muraoka. A Thomson scattering diagnostic system for measurement of electron properties of processing plasmas. *Plasma Sources Science and Technology*, 8(2):203, 1999.

[9] T. S. Brown. Plasma diagnostics using lasers: Relations between scattered spectrum and electron-velocity distribution. *Journal of Applied Physics*, 37(7):2709, 1966.

[10] D. Burgess. Collisionless shocks. In M. G. Kivelson and C. T. Russel, editors, *Introduction to Space Physics*, pages 129–163. Cambridge University Press, New York, 1995.

[11] S. E. Clark, D. Winske, D. B. Schaeffer, E. T. Everson, A. S. Bondarenko, C. G. Constantin, and C. Niemann. Hybrid simulation of shock formation for super-Alfvénic expansion of laser ablated debris through an ambient, magnetized plasma. *Physics of Plasmas*, 20(8):082129–082129–8, August 2013.

[12] A. Collette and W. Gekelman. Structure of an exploding laser-produced plasma. *Physical Review Letters*, 105(19):195003, November 2010.

[13] A. Collette and W. Gekelman. Structure of an exploding laser-produced plasma. *Physics of Plasmas*, 18(5):055705, 2011.

[14] Andrew Collette. *Structure of an Expanding Laser-Produced Plasma*. PhD thesis, University of California, Los Angeles, 2010.

[15] C. Constantin, W. Gekelman, P. Pribyl, E. Everson, D. Schaeffer, N. Kugland, R. Presura, S. Neff, C. Plechaty, S. Vincena, A. Collette, S. Tripathi, M. Muniz, and C. Niemann. Collisionless interaction of an energetic laser produced plasma with a large magnetoplasma. *Astrophysics and Space Science*, 322(1):155–159, 2009.

[16] C. D. David and H. Weichel. Temperature of a laser-heated carbon plasma. *Journal of Applied Physics*, 40(9):3674–3679, 1969.

[17] A. W. DeSilva, G. C. Goldenbaum, H. R. Griem, and R. H. Lovberg. *Plasma Diagnostics by Light Scattering*, volume Volume 9, Part 1. Academic Press, New York, 1971.

[18] A. W. DeSilva and J. A. Stamper. Observation of anomalous electron heating in plasma shock waves. *Physical Review Letters*, 19(18):1027, October 1967.

[19] G. Dimonte and L. G. Wiley. Dynamics of exploding plasmas in a magnetic field. *Physical Review Letters*, 67(13):1755, 1991.

[20] R. P. Drake. The design of laboratory experiments to produce collisionless shocks of cosmic relevance. *Physics of Plasmas*, 7(11):4690, 2000.

[21] D. E. Evans and J. Katzenstein. Laser light scattering in laboratory plasmas. *Reports on Progress in Physics*, 32(1):207–271, 1969.

[22] E. T. Everson, P. Pribyl, C. G. Constantin, A. Zylstra, D. Schaeffer, N. L. Kugland, and C. Niemann. Design, construction, and calibration of a three-axis, high-frequency magnetic probe (B-dot probe) as a diagnostic for exploding plasmas. *Review of Scientific Instruments*, 80(11):113505, 2009.

[23] Y. Fei, B. H. T. Chai, C. A. Ebbers, Z. M. Liao, K. I. Schaffers, and P. Thelin. Large-aperture YCOB crystal growth for frequency conversion in the high average power laser system. *Journal of Crystal Growth*, 290(1):301–306, April 2006.

[24] J. A. Fejer. Scattering of radio waves by an ionized gas in thermal equilibrium. *Canadian Journal of Physics*, 38:1114, 1960.

[25] K. A. Flippo, J. Workman, D. C. Gautier, S. Letzring, R. P. Johnson, and T. Shimada. Scaling laws for energetic ions from the commissioning of the new Los Alamos National Laboratory 200 TW Trident laser. *Review of Scientific Instruments*, 79(10):10E534–10E534–4, October 2008.

[26] D. H. Froula, J. S. Ross, L. Divol, and S. H. Glenzer. Thomson-scattering techniques to diagnose local electron and ion temperatures, density, and plasma wave amplitudes in laser produced plasmas (invited). *Review of Scientific Instruments*, 77(10):10E522, 2006.

[27] W. Gekelman, H. Pfister, Z. Lucky, J. Bamber, D. Leneman, and J. Maggs. Design, construction, and properties of the large plasma research device–the LAPD at UCLA. *Review of Scientific Instruments*, 62(12):2875, 1991.

[28] S. H. Glenzer, W. E. Alley, K. G. Estabrook, J. S. De Groot, M. G. Haines, J. H. Hammer, J.-P. Jadaud, B. J. MacGowan, J. D. Moody, W. Rozmus, L. J. Suter, T. L. Weiland, and E. A. Williams. Thomson scattering from laser plasmas. *Physics of Plasmas*, 6(5):2117, 1999.

[29] S. H. Glenzer, W. Rozmus, B. J. MacGowan, K. G. Estabrook, J. D. De Groot, G. B. Zimmerman, H. A. Baldis, J. A. Harte, R. W. Lee, E. A. Williams, and B. G. Wilson. Thomson scattering from high-Z laser-produced plasmas. *Physical Review Letters*, 82(1):97, 1999.

[30] G. C. Goldenbaum. Experimental study of collision-free shock waves and anomalous electron heating. *Physics of Fluids*, 10(9):1897, 1967.

[31] J. Grun, R. Decoste, B. H. Ripin, and J. Gardner. Characteristics of ablation plasma from planar, laser-driven targets. *Applied Physics Letters*, 39(7):545–547, October 1981.

[32] S. S. Harilal, C. V. Bindhu, R. C. Issac, V. P. N. Nampoori, and C. P. G. Vallabhan. Electron density and temperature measurements in a laser produced carbon plasma. *Journal of Applied Physics*, 82(5):2140–2146, 1997.

[33] D. W. Hewett, S. H. Brecht, and D. J. Larson. The physics of ion decoupling in magnetized plasma expansions. *Journal of Geophysical Research*, 116:12 PP., November 2011.

[34] F. C. Jones and D. C. Ellison. The plasma physics of shock acceleration. *Space Science Reviews*, 58(1):259–346, December 1991.

[35] S. Kacenjar, M. Hausman, M. Keskinen, A. W. Ali, J. Grun, C. K. Manka, E. A. McLean, and B. H. Ripin. Magnetic field compression and evolution in laser-produced plasma expansions. *Physics of Fluids*, 29(6):2007, 1986.

[36] M. Yu Kantor, A. J. H. Donné, R. Jaspers, H. J. van der Meiden, and TEXTOR Team. Thomson scattering system on the TEXTOR tokamak using a multi-pass laser beam configuration. *Plasma Physics and Controlled Fusion*, 51(5):055002, 2009.

[37] R. Kelly. On the dual role of the Knudsen layer and unsteady, adiabatic expansion in pulse sputtering phenomena. *The Journal of Chemical Physics*, 92(8):5047–5056, April 1990.

[38] R. Kelly and B. Braren. On the direct observation of the gas-dynamics of laser-pulse sputtering of polymers. *Applied Physics B*, 53(3):160–169, September 1991.

[39] C. F. Kennel, J. P. Edmiston, and T. Hada. A quarter century of collisionless shock research. In R. G. Stone and B. T. Tsurutani, editors, *Collisionless Shocks in the Heliosphere: A Tutorial Review*, volume 34. American Geophysical Union, Washington, D. C., 1985.

[40] M. H. Key, W. T. Toner, T. J. Goldsack, J. D. Kilkenny, S. A. Veats, P. F. Cunningham, and C. L. S. Lewis. A study of ablation by laser irradiation of plane targets at wavelengths 1.05, 0.53, and 0.35 m. *Physics of Fluids*, 26(7):2011, 1983.

[41] H. J. Kunze. The laser as a tool for plasma diagnostics. In W. Lochte-Holtgreven, editor, *Plasma Diagnostics*, page 550. North-Holland Publishing Company, Amsterdam, 1968.

[42] Thomas Lasspere. *An Analysis of the Effect of an Imposed Magnetic Field on the Spectrum of Incoherent Scattering.* PhD thesis, Cornell University, 1960.

[43] B. Lembege, J. Giacalone, M. Scholer, T. Hada, M. Hoshino, V. Krasnoselskikh, H. Kucharek, P. Savoini, and T. Terasawa. Selected problems in collisionless-shock physics. *Space Science Reviews*, 110(3):161–226, 2004.

[44] V. V. Lobzin, V. V. Krasnoselskikh, J.-M. Bosqued, J.-L. Pinçon, S. J. Schwartz, and M. Dunlop. Nonstationarity and reformation of high-Mach-number quasiperpendicular shocks: Cluster observations. *Geophysical Research Letters*, 34(5):L05107, March 2007.

[45] J. J. MacFarlane, I. E. Golovkin, and P. R. Woodruff. HELIOS-CR - a 1-D radiation-magnetohydrodynamics code with inline atomic kinetics modeling. *Journal of Quantitative Spectroscopy and Radiative Transfer*, 99(1-3):381–397, 2006.

[46] W. Marshall. The structure of magneto-hydrodynamic shock waves. *Proceedings of the Royal Society of London. Series A. Mathematical and Physical Sciences*, 233(1194):367–376, December 1955.

[47] M. Mattioli. Recombination processes during the expansion of a laser-produced plasma. *Plasma Physics*, 13(1):19, January 1971.

[48] J.B. McBride and E. Ott. Electromagnetic and finite e effects on the modified two stream instability. *Physics Letters A*, 39(5):363–364, June 1972.

[49] E. C. Merritt, A. L. Moser, S. C. Hsu, C. S. Adams, J. P. Dunn, A. M. Holgado, and M. A. Gilmore. Experimental evidence for collisional shock formation via two obliquely merging supersonic plasma jets. *Physics of Plasmas (1994-present)*, 21(5):055703, April 2014.

[50] B. Meyer and G. Thiell. Experimental scaling laws for ablation parameters in plane target–laser interaction with 1.06 m and 0.35 m laser wavelengths. *Physics of Fluids*, 27(1):302, 1984.

[51] N. K. Moncur, R. P. Johnson, R. G. Watt, and R. B. Gibson. Trident: a versatile high-power Nd:glass laser facility for inertial confinement fusion experiments. *Appl. Opt.*, 34(21):4274–4283, Jul 1995.

[52] K. Muraoka, K. Uchino, and M. D. Bowden. Diagnostics of low-density glow discharge plasmas using Thomson scattering. *Plasma Physics and Controlled Fusion*, 40(7):1221, 1998.

[53] L. Nemes, A. M. Keszler, J. O. Hornkohl, and C. G. Parigger. Laser-induced carbon plasma emission spectroscopic measurements on solid targets and in gas-phase optical breakdown. *Applied Optics*, 44(18):3661–3667, June 2005.

[54] A. Neogi and R. K. Thareja. Laser-produced carbon plasma expanding in vacuum, low pressure ambient gas and nonuniform magnetic field. *Physics of Plasmas*, 6(1):365–371, 1999.

[55] C. Niemann, A. S. Bondarenko, C. G. Constantin, E. T. Everson, K. A. Flippo, S. A. Gaillard, R. P. Johnson, S. A. Letzring, D. S. Montgomery, L. A. Morton, D. B. Schaeffer, T. Shimada, and D. Winske. Collisionless shocks in a large magnetized laser-plasma plume. *IEEE Transactions on Plasma Science*, 39(11):2406–2407, November 2011.

[56] C. Niemann, C. G. Constantin, D. B. Schaeffer, A. Tauschwitz, T. Weiland, Z. Lucky, W. Gekelman, E. T. Everson, and D. Winske. High-energy Nd:glass laser facility for collisionless laboratory astrophysics. *Journal of Instrumentation*, 7(03):P03010, 2012.

[57] C. Niemann, W. Gekelman, C. G. Constantin, E. T. Everson, D. B. Schaeffer, A. S. Bondarenko, S. E. Clark, D. Winske, S. Vincena, B. VanCompernolle, and P. Pribyl. Observation of collisionless shocks in a large current-free laboratory plasma. *Geophysical Research Letters*, 41, 2014.

[58] C. Niemann, W. Gekelman, C. G. Constantin, E. T. Everson, D. B. Schaeffer, S. E. Clark, D. Winske, A. B. Zylstra, P. Pribyl, S. K. P. Tripathi, D. Larson, S. H. Glenzer, and A. S. Bondarenko. Dynamics of exploding plasmas in a large magnetized plasma. *Physics of Plasmas*, 20(1):012108–012108–12, January 2013.

[59] N. Omidi, X. Blanco-Cano, C. T. Russell, H. Karimabadi, and M. Acuna. Hybrid simulations of solar wind interaction with magnetized asteroids: General characteristics. *Journal of Geophysical Research: Space Physics*, 107(A12):1487, December 2002.

[60] K. Papadopoulos, R. C. Davidson, J. M. Dawson, I. Haber, D. A. Hammer, N. A. Krall, and R. Shanny. Heating of counterstreaming ion beams in an external magnetic field. *Physics of Fluids (1958-1988)*, 14(4):849–857, April 1971.

[61] J. W. M. Paul, G. C. Goldenbaum, A. Iiyoshi, L. S. Holmes, and R. A. Hardcastle. Measurement of electron temperatures produced by collisionless shock waves in a magnetized plasma. *Nature*, 216(5113):363–364, 1967.

[62] N. J. Peacock, D. C. Robinson, M. J. Forrest, P. D. Wilcock, and V. V. Sannikov. Measurement of the electron temperature by Thomson scattering in Tokamak T3. *Nature*, 224(5218):488–490, November 1969.

[63] I. Podgorny. Collisionless shocks: Simulation and laboratory experiments. *Il Nuovo Cimento C*, 2(6):834–853, November 1979.

[64] R. Presura, S. Neff, and L. Wanex. Experimental design for the laboratory simulation of magnetized astrophysical jets. *Astrophysics and Space Science*, 307(1-3):93–98, 2007.

[65] B. H. Ripin, J. D. Huba, E. A. McLean, C. K. Manka, T. Peyser, H. R. Burris, and J. Grun. Sub-Alfvénic plasma expansion. *Physics of Fluids B: Plasma Physics*, 5(10):3491–3506, October 1993.

[66] J. S Ross, S. H Glenzer, P. Amendt, R. Berger, L. Divol, N. L Kugland, O. L Landen, C. Plechaty, B. Remington, D. Ryutov, W. Rozmus, D. H Froula, G. Fiksel, C. Sorce, Y. Kuramitsu, T. Morita, Y. Sakawa, H. Takabe, R. P Drake, M. Grosskopf, C. Kuranz, G. Gregori, J. Meinecke, C. D Murphy, M. Koenig, A. Pelka, A. Ravasio, T. Vinci, E. Liang, R. Presura, A. Spitkovsky, F. Miniati, and H. -S Park. Characterizing counter-streaming interpenetrating plasmas relevant to astrophysical collisionless shocks. *Physics of Plasmas*, 19(5):056501–056501–8, March 2012.

[67] P. T. Rumsby and J. W. M. Paul. Temperature and density of an expanding laser produced plasma. *Plasma Physics*, 16(3):247, 1974.

[68] C. T. Russell. An introduction to the physics of collisionless shocks. *AIP Conference Proceedings*, 781(1):3–16, 2005.

[69] E. E. Salpeter. Electron density fluctuations in a plasma. *Physical Review*, 120(5):1528–1535, December 1960.

[70] D. B. Schaeffer, E. T. Everson, A. S. Bondarenko, S. E. Clark, C. G. Constantin, S. Vincena, B. Van Compernolle, S. K. P. Tripathi, D. Winske, W. Gekelman, and C. Niemann. Laser-driven, magnetized quasi-perpendicular collisionless shocks on the Large Plasma Device. *Physics of Plasmas (1994-present)*, 21(5):056312, May 2014.

[71] D. B. Schaeffer, E. T. Everson, D. Winske, C. G. Constantin, A. S. Bondarenko, L. A. Morton, K. A. Flippo, D. S. Montgomery, S. A. Gaillard, and C. Niemann. Generation of magnetized collisionless shocks by a novel, laser-driven magnetic piston. *Physics of Plasmas*, 19(7):070702–070702–4, July 2012.

[72] D. B. Schaeffer, N. L. Kugland, C. G. Constantin, E. T. Everson, B. Van Compernolle, C. A. Ebbers, S. H. Glenzer, and C. Niemann. A scalable multipass laser cavity based on injection by frequency conversion for noncollective Thomson scattering. *Review of Scientific Instruments*, 81(10):10D518, 2010.

[73] D. B. Schaeffer, D. S. Montgomery, A. S. Bondarenko, L. A. Morton, R. P. Johnson, T. Shimada, C. G. Constantin, E. T. Everson, S. A. Letzring, S. A. Gaillard, K. A. Flippo, S. H. Glenzer, and C. Niemann. Thomson scattering measurements of temperature and density in a low-density, laser-driven magnetized plasma. *Journal of Instrumentation*, 7(02):P02002–P02002, February 2012.

[74] J. Sheffield, D. H. Froula, S. H. Glenzer, and N. Luhmann. *Plasma Scattering of Electromagnetic Radiaiton*. Academic Press, 2nd edition, 2011.

[75] R. K. Singh, O. W. Holland, and J. Narayan. Theoretical model for deposition of superconducting thin films using pulsed laser evaporation technique. *Journal of Applied Physics*, 68(1):233–247, July 1990.

[76] R. K. Singh and J. Narayan. Pulsed-laser evaporation technique for deposition of thin films: Physics and theoretical model. *Physical Review B*, 41(13):8843–8859, May 1990.

[77] D. S. Spicer, S. P. Maran, and R. W. Clark. A model of the pre-Sedov expansion phase of supernova remnant-ambient plasma coupling and X-ray emission from SN 1987A. *The Astrophysical Journal*, 356:549–571, June 1990.

[78] J. A. Stamper and A.W. DeSilva. Experimental study of the structure of plasma shock waves in a fast pinch. *Physics of Fluids*, 12(7):1435, 1969.

[79] D. A. Tidman and N. A. Krall. *Shock waves in collisionless plasmas*. Wiley Interscience, New York, 1971.

[80] B. Toftmann, J. Schou, T. N. Hansen, and J. G. Lunney. Angular distribution of electron temperature and density in a laser-ablation plume. *Phys. Rev. Lett.*, 84:3998–4001, Apr 2000.

[81] R. A. Treumann. Fundamentals of collisionless shocks for astrophysical application, 1. Non-relativistic shocks. *The Astronomy and Astrophysics Review*, 17(4):409–535, 2009.

[82] M. J. van de Sande and J. J. A. M. van der Mullen. Thomson scattering on a low-pressure, inductively-coupled gas discharge lamp. *Journal of Physics D: Applied Physics*, 35(12):1381–1391, 2002.

[83] Marcus Johannes van de Sande. *Laser scattering on low temperature plasmas - High resolution and stray light rejection*. PhD thesis, Technische Universiteit Eindhoven, 2002.

[84] Michael Anthony Van Zeeland. *Generation of shear Alfven waves by expanding plasmas*. PhD thesis, University of California, Los Angeles, United States – California, 2003.

[85] M. VanZeeland and W. Gekelman. Laser-plasma diamagnetism in the presence of an ambient magnetized plasma. *Physics of Plasmas*, 11(1):320, 2004.

[86] D. Winske and S. P. Gary. Hybrid simulations of debris-ambient ion interactions in astrophysical explosions. *Journal of Geophysical Research*, 112:11 PP., October 2007.

[87] D. Winske, J. Giacalone, M. F. Thomsen, and M. M. Mellott. A comparative study of plasma heating by ion acoustic and modified two-stream instabilities at subcritical quasi-perpendicular shocks. *Journal of Geophysical Research*, 92(A5):PP. 4411–4422, May 1987.

[88] C. S. Wu, D. Winske, Y. M. Zhou, S. T. Tsai, P. Rodriguez, M. Tanaka, K. Papadopoulos, K. Akimoto, C. S. Lin, M. M. Leroy, and C. C. Goodrich. Microinstabilities associated with a high Mach number, perpendicular bow shock. *Space Science Reviews*, 37(1-2), 1984.

[89] Y. P. Zakharov. Collisionless laboratory astrophysics with lasers. *IEEE Transactions on Plasma Science*, 31:1243–1251, December 2003.

[90] S. J. Zweben, J. Caird, W. Davis, D. W. Johnson, and B. P. Le Blanc. Plasma turbulence imaging using high-power laser Thomson scattering. *Review of Scientific Instruments*, 72(1):1151, 2001.